MOLECULAR SIMULATIONS ON THE ELONGATION DYNAMICS OF GOLD NANOWIRES IN VACUUM AND IN SOLVENTS

By

Qing Pu

Dissertation

Submitted to the Faculty of the

Graduate School of Vanderbilt University

in partial fulfillment of the requirements

for the degree of

DOCTOR OF PHILOSOPHY

in

Chemical Engineering

May, 2008

Nashville, Tennessee

Approved:

Professor Peter T. Cummings

Professor G. Kane Jennings

Professor Clare McCabe

Professor Kenneth A. Debelak

Professor Ronald D. Schrimpf

To my amazing daughters, Jingyi and Jiayi,

and

To my beloved husband, Dongshun Bai.

ACKNOWLEDGMENTS

I would like to thank my advisor Dr. Peter Cummings for his extremely helpful guidance and great encouragement throughout my research. I appreciate everything he has done for me, especially for leading me to this exciting molecular simulation field. I admire Dr. Cummings not only because his erudition but also his passion in research, which are of great value to my future career. I would like to express my gratitude to Dr. Yongsheng Leng for his support, patience and encouragement along my Ph.D. study. He always has been there to guide me to the right direction and encourage me to be a deeper thinker. I thank all my committee members, Dr. Kane Jennings, Dr. Clare McCabe, Dr. Kenneth Debelak, Dr. Harold Park, and Dr. Ron Schrimpf for their constructive suggestions and valuable input from different perspectives.

I thank all the faculty, staff and students in the Department of Chemical Engineering for making a wonderful memory during my graduate study at Vanderbilt.

I would like to thank my husband Dongshun Bai. His endless love and support inspire me to successfully finish my doctorial study. Being his wife is the wisest choice in my life. I thank my daughters Jingyi and Jiayi. They have brought a lot of fun into my life. I am also grateful for the unconditional love and support from my parents and sister.

Finally, I thank the financial support from the Office of Science of the U.S. Department of Energy Computational Nanoscience Project and Vanderbilt Advanced Computing Center for Research and Education (ACCRE) for the computational time.

TABLE OF CONTENTS

Page

LIST OF TABLES

LIST OF FIGURES

CHAPTER I

INTRODUCTION

Metallic nanowires have many important technological applications, especially in the field of molecular electronics (ME). In particular gold (Au) nanowires are very interesting and promise to play a major role in nanodevices. This is due to their good conductivity, high strength, and ductility. In addition, Au nanowires have relative ease of fabrication, stability at small scales and capability for biomolecular functionalization.[1]

Gold nanowires severing as metallic contacts have attracted considerable interest recently.[2] On the experimental side, advances in experimental techniques make it possible to generate atomic-sized molecular break-junctions.[3-5] The mechanically controllable break junction (MCBJ) technique[4,6-8] that mainly focuses on studying the quantum size effects on conductance is one of these methods. In an MCBJ experiment, a metallic wire is attached to a flexible substrate that will be bent to stretch and break the wire. Afterwards, the broken wire can be brought repeatedly in and out of contact under the gentle control of the distance between two contacts. On the theoretical side, different approaches are performed to investigate the quantum conductance properties[9-12], the mechanical deformations under tensile strain,[9-15] and the break-junction structural properties.[2,10,11,13,16-18] The molecular dynamics (MD) technique combined with classical potentials is one of these approaches. However, several issues need to be solved to guarantee accurate MD study. Firstly, an accurate potential must be selected to describe the interactions between metal molecules. Various classical potentials such as the glue

model,[19] effective medium theory potential,[11] the Sutton-Chen potential,[13] the embedded-atom method (EAM),[14] the second-moment approximation of the tight-binding scheme (TB-SMA),[16] and the Finnis-Sinclair potential,[12,20] which are usually constructed for and tested on bulk systems or optimized to handle surfaces, have been applied in previous literatures without further evaluating their applicability for the very low-coordination chains. In this study, we establish an optimum potential out of three commonly used classical potentials for nanostructures (the glue model, the EAM potential and the TB-SMA potential) with large numbers of low-coordination atoms by the aid of advanced density-functional-theory (DFT) calculations. Secondly, MD simulations must take into account that experiments are performed under various conditions. For example, the elongation of nanowires can be done at room temperature or liquid-helium temperature under ultrahigh-vacuum or ambient conditions. Furthermore, the experimentally generated nanowires could adopt different crystallographic directions which then produce distinct break-junction structures. Nevertheless, most of the existing theoretical studies are based on very specific conditions such as fixed configuration and temperature. In this work, in order to get a more complete picture, a systematic statistical study of various experimental situations is used to explore the effects of crystallographic orientation, length, elongation rate, temperature as well as initial configuration on the ductile elongation properties of nanowires.

After obtaining the dynamic elongation properties and break-junction structures of Au nanowires, additional important issues follow in investigating the gold electrodes linked through organic molecules. Organic molecules bonded between two gold electrodes have emerged as prototypical metal-molecule-metal configurations in

molecular electronic devices, and their current-voltage (*I*-V) characteristics have attracted considerable interest in both experiments[3-5] and theories.[21-25] Studying the *I*-V characteristics of single molecules is a key step towards the development of practical molecular electronics devices. Theoretical research has been mainly focused on reproducing the current-voltage behavior observed in experiments for various types of molecular junctions via quantum calculations. Examples of such calculations are the density-functional-theory-based calculations of conductance of benzenedithiol (BDT)/Au systems.[21-25] These calculations qualitatively reproduced the characteristics of the current-voltage curve from experiments, but exhibited large quantitative deviations. One possible reason is the lack of realistic input to *ab initio* calculations, which were performed in a vacuum at 0 K with a jellium model for the electrode.[21] In the actual experiment, the temperature fluctuations, conformation, degree and nature of bonding, and adsorption conditions of the Au-BDT-Au junctions[26-30] must impact the measured *I*-V characteristics. Most importantly, many of the experimental *I*-V measurements in metal-molecule-metal junctions have been performed on junctions created through mechanical stretching of nanowires in an organic solution. The electronic properties of these junctions are dependent on both the stretching process and the environment in which the fabrication is performed. However, the effect of solvent on the elongation properties of nanowires has not been previously investigated. Molecular modeling is a natural tool to investigate such questions. This study is the first theoretical approach to investigate the solvent effects on the elongation of the Au Nanowires. We extend our study to involve both a simple Lennard-Jones solvent propane and a much complex organic molecule BDT which has the potential to covalently bind to gold nanowire as

self-assembled monolayers (SAMs). For propane, MD simulations are applied to understand to what extent the thermal collisions of nonbonded particles will influence the mechanical elongation property of Au nanowires. For BDT, Monte Carlo simulations were performed to study the self-assembled structure of BDT molecules on a gold nanowire when it is immersed in a bulk BDT liquid followed by MD to obtain detailed bonding geometries at the Au-BDT interface for future, more accurate quantum mechanical calculations of *I-V* characteristics.

The organization of the thesis is as follows: after a brief introduction and background description, in chapter III, we present the dynamic elongation of gold nanowires in vacuum. An optimum potential which works well for the very low-coordinated atom chains is identified and applied to statistically investigate the elongation of nanowires under various conditions. In Chapter IV, we extend our study to predict the dynamic elongation properties of gold nanowires in the non-polar solvent propane. The ductile elongations are compared with the nanowires elongated in vacuum at various temperatures. In Chapter V, a more realistic solution, BDT, is introduced. Combining grand canonical Monte Carlo (GCMC) with canonical Monte Carlo (MC) simulations, we studied the adsorption configurations of BDT on gold nanowires. In the following Chapter VI, starting from the final adsorption configurations, we investigated the dynamic elongations and breakage of gold nanowires in organic solvents at various temperatures. Finally, concluding remarks are made and recommendations for future works are discussed in Chapter VII.

CHAPTER II

BACKGROUND

After the invention of the transistor (1948) and the integrated circuit (1959), the microelectronics industry embarked on the remarkable evolution known as Moore's law, according to which the speed of computer chips will double every 18 months. This is achieved by increasing the density of circuit elements in a microprocessor by a factor of two every 18 months. Hence, while every 18 months the speed of computer chips increases by a factor of two, so does the cost to produce them. As Si-based device dimensions are now under 100-nm in feature size (current feature size is 65 nm; 45 nm technology is already in preproduction), approaching the physical limits of this technology, molecular electronics (ME) devices are emerging as an alternative practical and economic route to continuing miniaturization. ME entails a significant paradigm change for process and device modeling. The key processing step in Si technology, lithography, is likely to be replaced in ME devices by self assembly. Molecular-scale devices offer several advantages over conventional technology, including miniaturization that will allow the scaling of component size to the ultimate level of atoms and molecules. Potential benefits include dramatically increased computational speed and lower fabrication costs. However, the path to single-molecule electronic devices, which began with the theoretical prediction over 25 years ago that such devices were possible,[31] has been characterized by a significant disconnect between theory and experiment. For example, theory reproduced the qualitative features of the measured current-voltage

characteristics for a BDT molecule very successfully,[28] but the theoretical value of the current is larger than experiment by more than two orders of magnitude. The origin of the discrepancy has not been fully resolved although several factors can be easily identified, such as the contact geometry and chemistry. Theoretical efforts are underway aimed at developing the simulation and design tools needed to quantitatively model electron transport through organic molecules in the environment in which such molecules find themselves in experiments and proposed devices.

Early in 1970s, Aviram and Ratner proposed that certain organic molecules may be used to construct ME devices, by specifically showing (using quantum chemistry methods) how a single molecule could act as a rectifier.[31] In addition, molecular and nanoscale structures have been shown to be capable of other basic electronic functions such as negative differential resistance and acting as a single-electron transistor.[27,32-35] Extensive experimental and theoretical work has been performed in recent years on probing such a possibility. It has been demonstrated that some of the thiolate molecules, such as BDT, show promising conducting properties when assembled on gold tips. Current-voltage and conductance properties of molecular junctions have been measured experimentally by several independent groups.[3-5,36]

In the Reed *et al.*[4] experiment, BDT molecules are self-assembled onto an Au wire, creating a SAM as demonstrated in Figure 2.1. The BDT molecules are covalently bonded to the Au surface through an S-Au bond at each end. The wire is then pulled apart until break point, creating two tips on which the SAM persists and equilibrates. The two tips are brought together until current (I) flows under an applied voltage (V).

The electrode separation is adjusted until minimum current flows, which is assumed to be associated with a single molecule bridging the gap.

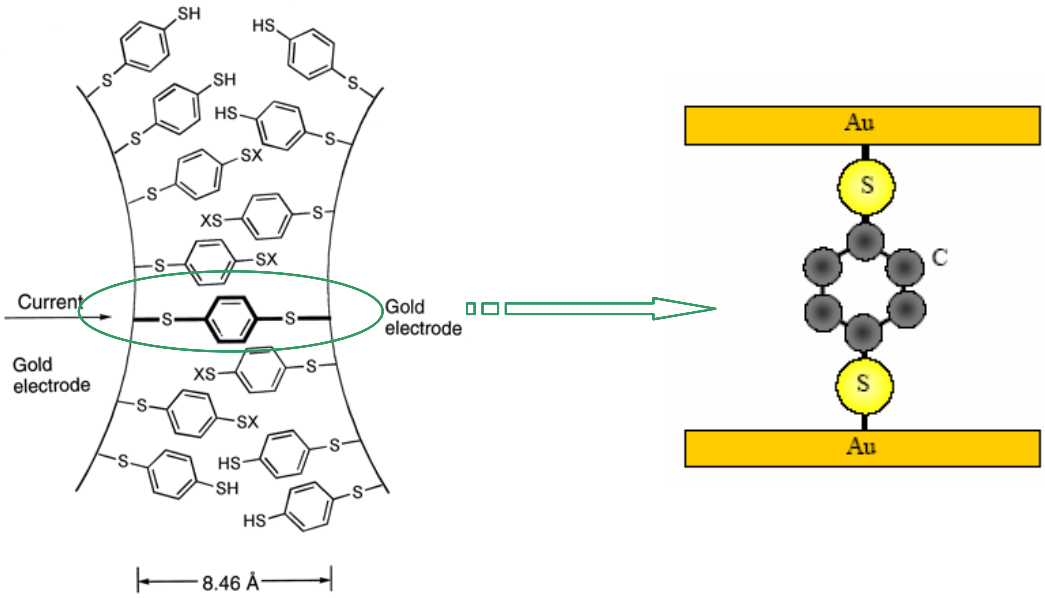

Figure 2.1. Schematic of BDT molecules bonded to gold electrodes.

The large discrepancy between the theoretical calculation[21] and the Reed *et al*. experiment led to speculation that perhaps the BDT molecules were not chemically bonded on both sides of the molecule. To ensure covalent bonding on both sides of the molecule, Cui *et al.*[3] devised the experiment shown schematically in Figure 2.2, in which a two-component SAM of alkanethiols (ATs) is bonded to a gold surface on one end; the dilute component in the SAM is a dithiol – i.e., has S atoms at each end of the molecule – while the other, predominant component has a S group at one end only (i.e., at the end bonded to the Au surface). The SAM is then exposed to a solution of colloidal gold particles. Gold clusters chemically bond to S atoms in the dithiols, while the other molecules in the SAM act effectively as insulators. They then measured statistically distinct cases in which a gold-coated AFM tip was in contact with 0, 1, 2, 3 and 4 gold clusters (and hence 0-4 AT molecules), and from this infer the inherent conduction of a single AT molecule chemically bonded at each end to gold. This measured conductance differs from theoretical calculations by only a factor of 6, indicating the importance of the quality and nature of the metal-molecule contact. However, the assumption in Cui *et al.*'s experimental work is that the limit to conductance is the AT molecule; other possibilities include the gold cluster being conductance-limiting, and in fact this assumption underlies experimental methods to measure the conductance of gold clusters.[37-39]

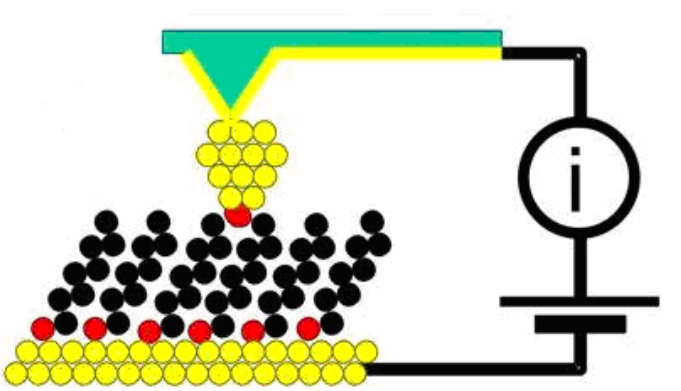

Figure 2.2. Schematic illustration of Cui *et al.'s*[3] experiment.

Other ME experiments involve the same principles (self assembly, followed by conductance measurement), such as the monolayer protected clusters (MPCs) experiments by Cliffel,[40] in which ME devices involve self-assembly followed by the creation of a mechanism for addressing (ie., accessing electrically) the individual molecules.[41-43]

In regard to the self-assembly structure of BDT molecules on Au surface, previous MD simulations[44,45] have been performed to investigate the packing structure of BDT and the bonding of S atoms onto Au(111) surface. These studies developed a classical forcefield for the chemical bonding between gold atoms and BDT molecules based on *ab initio* calculations. It has been shown that the intermolecular BDT-BDT interactions play a dominant role in determining the BDT SAMs global packing structure and bond-stretching potential is the most dominant part in chemical bonding. Most recently, Zhao *et al.* [46] reported a Monte Carlo simulation study of self assembly of BDT/THF mixtures on Au (111) surface. The simulation results indicated that BDT molecules prefer to anchor to the Au (111) surface with one of the sulfur atoms bonded with Au atom and the perpendicularly oriented BDT forms an ordered structure on Au (111) surface. By comparison, the solvent THF molecules form clusters either above the BDT monolayer, or occupy the vacancies on the Au (111) surface not covered by BDT molecules. The THF molecules always exhibit amorphous structure on Au surface, while the BDT molecules form an ordered array at high coverage. Therefore, it is very interesting to investigate the packing structures of BDT molecules on curved Au nanowires and study the effect of solvent on the dynamical elongation properties.

In this work, our main goal is to obtain detailed configurations of the Au-BDT interface, aiming at providing better input information for further quantum *I*-V calculations. This study is valuable since the results are helpful in understanding the underlying mechanism of the formation of Au-BDT-Au junctions implemented in molecular conductance measurements and will provide accurate input configurations for quantum mechanical *I*-V calculations. These calculations will help to resolve the original discrepancy between experimental and theoretical studies. Additionally, classical molecular modeling also permits us to interpret and provide useful feedback to experimental measurements, device design, and manufacture.

CHAPTER III

DYNAMIC ELONGATION OF NANOWIRES IN VACUUM

3.1. Introduction

In addition to the relevance of the break-junction technique for the study of molecular electronic devices, pulling a gold wire apart is in itself an interesting physical process. Perhaps the most notable of the interesting features observed are the break-junction structures, which in certain cases are ultrathin chains with only one atom thick and in some other cases, the occurrence of multi-shell structures. For this reason, the formation of Au nanowire break-junctions has been studied extensively with a number of experimental techniques, such as scanning tunneling microscopy (STM),[47-49] atomic force microscopy (AFM),[50,51] mechanically controllable break-junction (MCBJ)[6,7] and *in situ* high resolution transmission electron microscopy (HRTEM)[16,49,52,53]. The conductance properties and the real time visualization of dynamical nanowires elongation can be obtained from these experimental studies. Figure 3.1 shows some typical break-junction images obtained by various experimental techniques. On the theoretical side, simulations have provided atomic-scale details of the chain formation, particularly on the final stages before the gold chains break apart.[11,16,54] The elongation process has been modeled using classical MD simulation with either empirical potentials [for example, using the glue model,[55] the effective medium theory (EMT) potential,[11] Sutton-Chen potential,[13] and the EAM potential[14]] that aim to take into account many-body effects, or using potentials which are calibrated to reproduce features of the band structure through the second

moment of density of state [for example, the TB-SMA potential[16] and Finnis-Sinclair potential[12,20]]. Approaches that include the electronic structure are also available through first principles quantum mechanical calculations.[10,18,54,56,57] Whereas such techniques can provide parameter-free results, they are inherently limited to systems of small size and to a small number of configurations, usually those corresponding to the final stages before breakup or the selected parts of the Au tip-neck-tip system.[10,56] MD simulations using semi-empirical potentials have lesser accuracy but can handle very large systems with relatively low computational cost. However, the semi-empirical potentials used are constructed for and tested on bulk systems, where all atoms have full or near-full coordination. In some cases, the potentials are optimized to handle surfaces, but typically flat surfaces of a macroscopic crystal. Thus, potentials calibrated using bulk and infinite-surface properties may or may not work well for the very low-coordinated atomic chains. A comparison using the same protocol for different approaches would be valuable. In this respect, first-principles methods are ideal for evaluating the semi-empirical potentials, with the aim of establishing an optimal simulation approach for nanostructures with large numbers of low-coordination atoms. In this work, we combine MD simulation with DFT calculations to evaluate the quality of typical empirical or semi-empirical potentials widely used in the MD simulation community. Three different forcefields, the glue model,[55] the EAM,[58] and the TB-SMA[59] have been used in the MD simulations. We found that the TB-SMA potential is the most suitable one to describe the elongation properties of gold nanowire. Our calculations further illustrate that the TB-SMA potential can correctly predict the breaking force (1.5 N) of monatomic chains in the final stage of breakup, as observed in experimental measurement.[10]

To date, there are many reports on the break-junction structure. On the one hand, Coura *et al.*[16] and Rodrigues *et al.*[52] have reported the formation of monatomic chain with 2~4 atoms prior to fracture using the high resolution transmission electron microscopy (HRTEM) technique. Performing the scanning tunneling microscope (STM) technique at temperature 4.2 K, Rubio-Bollinger and coworkers[10] have predicted the formation of ~ 4-atom-long single atom chains. This result has been verified by MD simulations[2,11,13,16] using the TB-SMA, the effective medium theory potential and the Sutton-Chen potential. This single-atom thickness configuration has been proven by first principles calculations as well.[10,57] On the other hand, the formation of three-atom-thick chain with the zigzag, helical structure has also been observed by the aid of HRTEM method under the ultra-high vacuum ambient.[60] This multi-shell structure has also been confirmed by MD simulations[61,62] using the EAM potential. Additionally, first principle calculations[63] have shown that the gold nanowires form spinning zigzag shape under tension. In this work, we show that break-junctions adopt different structures under various conditions. The nanowires tend to form long monatomic chains when low temperature is combined with high elongation rate. However, helical, zigzag-type long chains more often appear for a high-aspect- ratio nanowires at low elongation rate and room temperature.

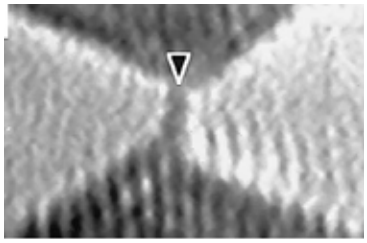

(a)

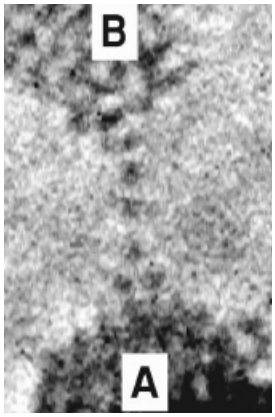

(b)

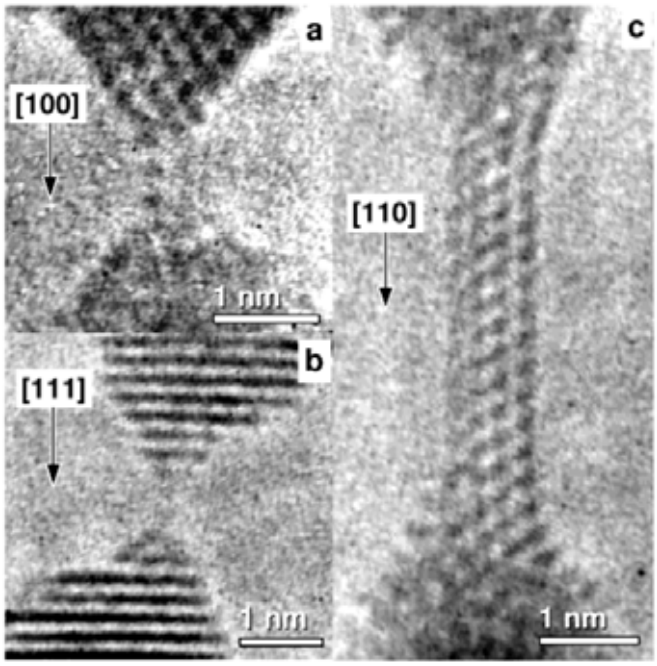

(c)

Figure 3.1. Typical experimental break-junction images. (a) break-junction structure obtained by Ohnishi *et al.*'s STM experiment;[49] (b) break-junction structure obtained by Rodrigues *et al.*'s HRTEM experiment;[53] (c) HRTEM images of gold nanowire formation for different crystallographic orientations by Coura *et al.*[16]

3.2. Simulation Details

3.2.1. Forcefields

In this work, we focus on three semi-empirical forcefields: the glue model proposed by Ercolessi *et al*.,[55] the EAM[58,61] originally developed by Daw and Baskes, and the TB-SMA developed by Cleri and Rosato.[59] Though all of these three potentials include many-body effects, which are very important for metallic bonding in transition metal systems, their derivations are quite different. The glue model is a purely empirical potential whose parameters are fitted to important thermal and surface properties of the system of interest.[55] The EAM potential is a semi-empirical potential that allows for electron density variations depending on the local bonding environment. The TB-SMA potential includes the long-range band-structure effect, and is an approximation to the quantum tight-binding (TB) potential.[59]

3.2.1.1. Glue Model

In the glue model, the total energy of a system is written in the form:

$$V = \frac{1}{2}\sum_{\substack{i,j=1 \\ (j\neq i)}}^{N}\phi\left(r_{ij}\right)+\sum_{i=1}^{N}U\left(n_i\right) \tag{3-1}$$

where the first term on the right side presents the standard pair potential while the second term accounts for the many body effects. Here n_i is the coordination of atom *i*, which contributes from superposition of the neighboring atoms:

$$n_i = \sum_{\substack{j=1 \\ (j \neq i)}}^{N} \rho(r_{ij}) \tag{3-2}$$

where $\rho(r)$ is a short-ranged monotonically decreasing function of distance. $\phi(r)$, $U(n)$ and $\rho(r)$ are polynomial functions constructed empirically by fitting several physical quantities including thermal and surface properties such as $T = 0$ K lattice parameter, the cohesive energy, the bulk modulus and the surface energy.[55]

3.2.1.2. EAM Potential

The EAM potential utilized in this paper is a modification by Foiles of the potentials originally developed by Voter and Chen.[64,65] The original Voter-Chen potentials were fit to cohesive energy, equilibrium lattice constant, bulk modulus, cubic elastic constants and the unrelaxed vacancy formation energy, bond length and bond strength of the diatomic molecule. The Foiles potential utilizes the same functional forms as the Voter-Chen potential with parameters modified to yield a more accurate estimate of the intrinsic stacking fault energy. For an experimentally measured intrinsic stacking fault energy of 32 mJ/m^2 for gold,[65] the Voter-Chen potential predicts a value of 9.74 mJ/m^2, while the Foiles potential predicts a more accurate value of 31 mJ/m^2. A full listing of the physical properties and fitting parameters that characterize both the Voter-Chen and Foiles potential as well as a discussion on the importance of accurately modeling stacking fault energies in nanowire modeling can be found in Park and Zimmerman.[61]

For the EAM, the total energy U for a system of atoms can be written as:

$$U = \sum_{i=1}^{N} \left(F_i(\rho_i) + \frac{1}{2} \sum_{j \neq i}^{N} \phi_{ij}(R_{ij}) \right) \tag{3-3}$$

where the summations extend over the total number of atoms N in the system, F_i is the embedding function, ρ_i is the electron density at atom i, ϕ_{ij} is a pair interaction function and R_{ij} is the distance between atoms i and j.

3.2.1.3. TB-SMA Potential

In the framework of the TB-SMA, the cohesive energy E_c of the system is made up of a short-range repulsive pair potential and an effective band term.

$$E_c = \sum_i \left[\sum_j A e^{-p(r_{ij}/r_0 - 1)} - \left\{ \sum_j B^2 e^{-2q(r_{ij}/r_0 - 1)} \right\}^{1/2} \right] \tag{3-4}$$

where the first term is the repulsive pair potential described by a sum of Born-Mayer ion-ion repulsion, and r_{ij} represents the distance between atom i and j and r_0 is the first-neighbors distance in the lattice. The second term is the band energy, which is proportional to the square root of second moment. The parameter B is an effective hopping integral and q describes its dependence on the relative interatomic distance. The free parameters A, B, p, q and r_0 are fitted to the experimental values of cohesive energy, lattice parameter, elastic constants of the corresponding real system at $T = 0$ K. Values of the TB-SMA parameters are taken from the literature[59] and list in Table 3.1.

Table 3.1. Parameters of the TB-SMA potential for Au.

Material	A(eV)	B(eV)	p	q
Au	0.2061	1.790	10.229	4.036

3.2.2. Simulation Methodology

We have performed MD simulations for the elongation of Au nanowires under various initial configurations. A few layers at both ends of the nanowires are kept rigid and the atoms between these two blocks are dynamic during the MD runs. Before pulling, the system is allowed to relax for 120 ps. Elongation of the wire is realized by displacing the top rigid layers along the *z* direction in a small increment, while keeping the other end fixed until the whole system is fully relaxed. The equations of motion are integrated via the velocity Verlet algorithm and the temperature is controlled by Nosé – Hoover thermostat[66-68] correspondingly to elongation in an inert solvent. We do not apply periodic boundary conditions in our simulations.

3.3. Evaluation of Semi-empirical Forcefields

We evaluate three typical semi-empirical forcefields by comparing both the static structural relaxation properties and dynamic elongation behavior of a 256-atom gold cluster with results from DFT calculations. Moreover, we demonstrate that the TB-SMA potential can properly predict the single bond strength of gold monatomic chain before its breakage.

3.3.1. Static Structure Relaxation

We first study the static structure relaxation of a 256-atom gold cluster from an initially unrelaxed configuration, corresponding to the bulk crystal, as shown in Figure 3.2(a). The DFT calculations for the 256-atom small Au nanowire use a local-density approximation (LDA) exchange-correlation functional,[69] ultrasoft pseudopotentials,[70] and

a plane-wave basis as implemented in the VASP code.[71] We use Γ point sampling and an energy cutoff of 180 eV, unless stated otherwise. LDA functional is known to describe accurately[72,73] both bulk and surface properties of Au. The "energy drops", defined as the energy differences between the relaxed and unrelaxed configurations at T= 0.01 K, are summarized in Table 3.2. We see that the TB-SMA energy drop has almost the same value as that given by the DFT calculation. In comparison, both the glue model and the EAM potential yield energy drops that are noticeably larger. In particular, the energy drop given by the glue model is almost eight times that of the DFT result. This over-relaxation by the glue and EAM potentials can be also seen in Figures 3.2(d) and 3.2(e), respectively, where we show the relaxed configurations prior to pulling. In contrast, Figure 3.2(b) and 3.2(c) show that both the DFT and the TB-SMA potentials give almost the same relaxed atomic configurations.

Table 3.2. The energies drops ΔE (kcal/mol) from the DFT energy calculation and the other three forcefields predictions. ($\Delta E = E_{crystal} - E_{relaxed}$)

	DFT	TB-SMA	Glue	EAM
ΔE	185.93	186.91	1369.28	705.44

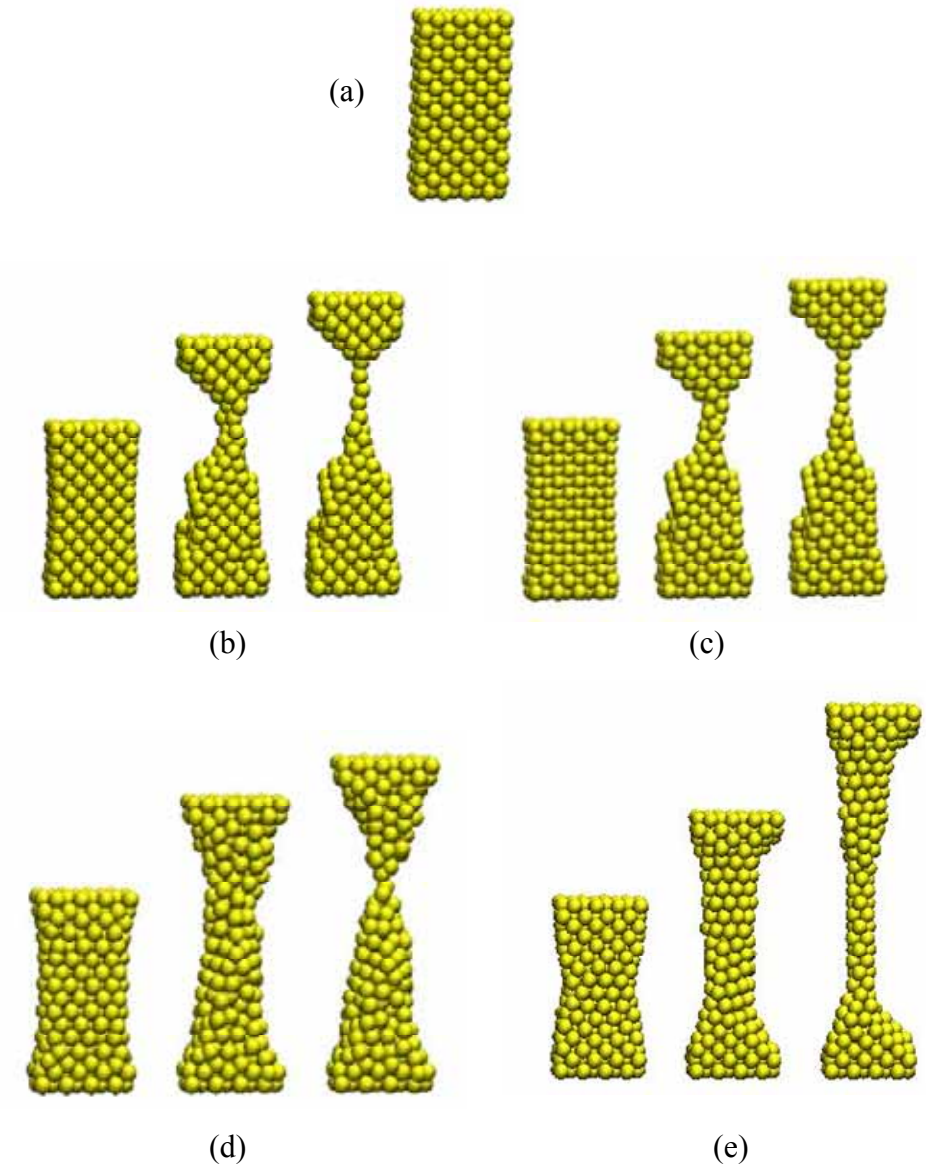

Figure 3.2. Representative snapshots for the elongation process for small Au (001) system at 0.01 K: (a) initially unrelaxed bulk structure; (b) DFT relaxed configurations prior to pulling, the intermediate stage (1590 ps) and the final break junction (2390 ps) along TB-SMA trajectory; (c) the TB-SMA configurations prior to pulling, the intermediate stage (1590 ps), and the final break junction (2390 ps); (d) the glue model configurations prior to pulling, the intermediate stage (1590 ps), and the final break junction (2208 ps) and (e) the EAM configurations prior to pulling, the intermediate stage (1590 ps) and the final break junction (3570 ps).

3.3.2. Dynamic Elongation Behavior

We now explore the elongation behavior of gold nanowires by MD simulation method. The nanowires consist of 16 layers of Au atoms, for a total of 256 atoms. Elongation of the wire is realized by displacing the top rigid layers along the *z* direction in increments of 0.1 Å, while keeping the other end fixed. For every 0.1 Å increment the whole system is allowed to relax for 5000 time steps with a time step of 2 fs, corresponding to an elongation velocity of 1.0 m/s. The three semi-empirical potentials generate three different elongation-energy paths. Along these three different atomic-configuration trajectories, DFT total energy calculations are performed. The relative elongation-energy differences between the DFT results and the corresponding results predicted by the different potentials are shown in Figure 3.3(a). Figure 3.3(b) enlarges part of Figure 3.3(a) to clearly show the energy differences between the TB-SMA and the DFT results. In these Figures, the total energies of the initial unrelaxed configuration (the bulk crystal, $E_{crystal}$) given either by the DFT or semi-empirical potentials are taken as the initial reference points. Evidently, the minimum elongation-energy difference curve between the MD and the DFT calculations corresponds to that given by the TB-SMA potential. The relative elongation-energy differences between the DFT and the other two MD simulation results given by the glue and EAM, as clearly shown in the figure, are dramatic. This is particularly true for the glue model.

(a)

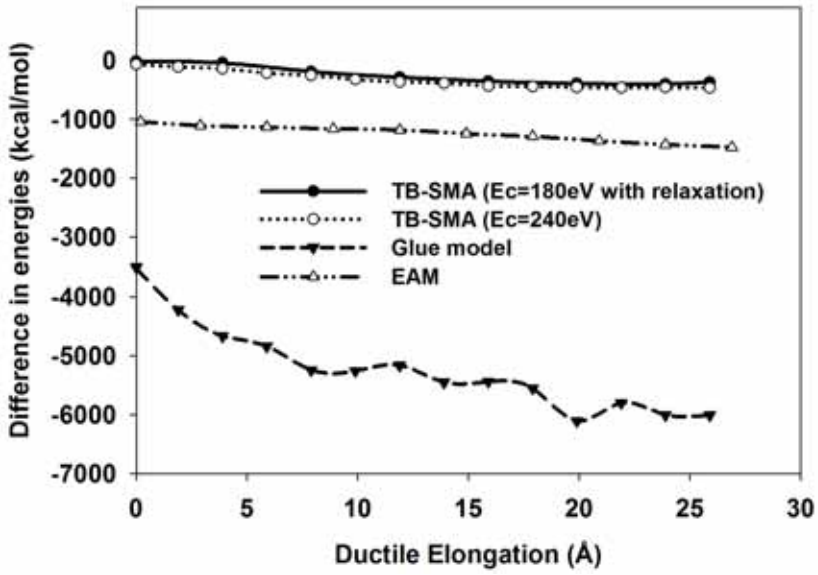

(b)

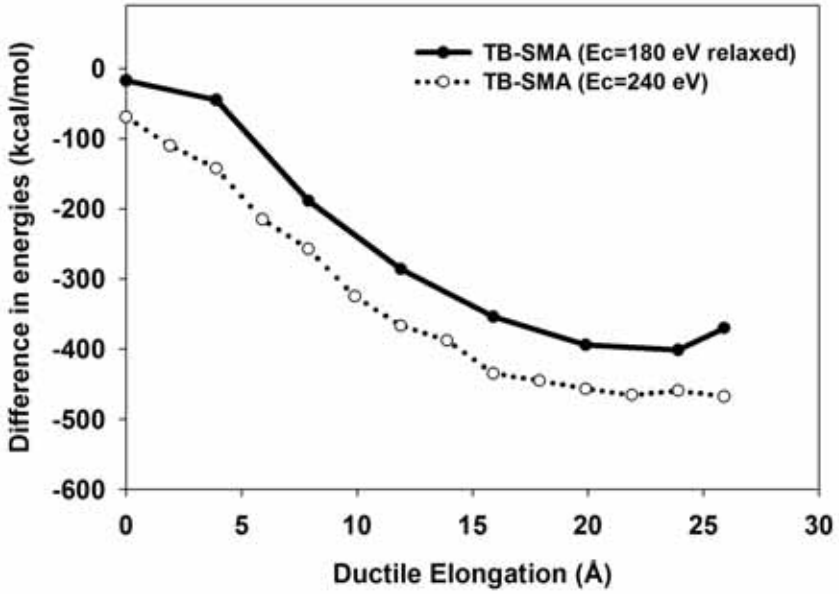

Figure 3.3. (a) The relative elongation-energy differences between the results given by the semi-empirical potentials and by the DFT calculations for the small Au (001) system at 0.01 K. This relative elongation-energy difference is defined as $\Delta E=[E(t)-E_{crystal}]_{classical}$ $-[E(t)-E_{crystal}]_{DFT}$. (b) The enlarged diagram for the results along the TB-SMA trajectory. Along the TB-SMA trajectory, the complete DFT energy relaxation calculation (energy cutoff = 180 ev) gives a relatively lower energy difference (solid line), as compared with the total DFT energy calculation with an even higher energy cutoff of 240 ev (dotted line). DFT energy calculation with an energy cutoff of 180 ev yields almost the same result as that of 240 ev cutoff, thus demonstrating the convergence of the DFT results relative to the energy cutoff of the basis set.

The initial, intermediate, and final break-junction atomic configurations given by the three semi-empirical potentials are shown in Figure 3.2 (c) – 3.2 (e). The total elongation at $T = 0.01$ K before breakup are 24.9, 22.0, and 35.7 Å, respectively, for the TB-SMA, the glue model, and the EAM potentials. Obviously, the EAM gives a much longer ductile elongation. The longer ductile elongation is even more noticeable at room temperature as shown in Figure 3.4 in which both the glue and EAM potentials generate much longer and thicker chains. The striking differences with the TB-SMA results are not surprising in view of the earlier comparisons. As far as we are aware, the effect of temperature on the mechanical behavior of gold nanowire has not been reported in experiments.

The comparably small differences between the DFT and the TB-SMA results suggest that the TB-SMA potential favors the formation of low energy break-junction structures, whereas the glue model and the EAM potential yield relatively higher energy structures. This indicates that the glue and the EAM models are not suitable for low-coordinated systems such as ultrathin Au chains, though all three semi-empirical potentials are calibrated to the bulk properties. The formation of monatomic chain structures found by the TB-SMA simulations, which is inherently a quantum phenomenon, has been observed in several experimental studies.[16,49,53] The ability of the TB-SMA potential to simulate the experimentally observed monatomic chain structure is probably due to the underlying electronic band structure and relatively longer range cutoff,[59] which is likely to be an essential feature in describing the dynamical formation of thin wires, particularly in the last stage of the formation of monatomic chains.

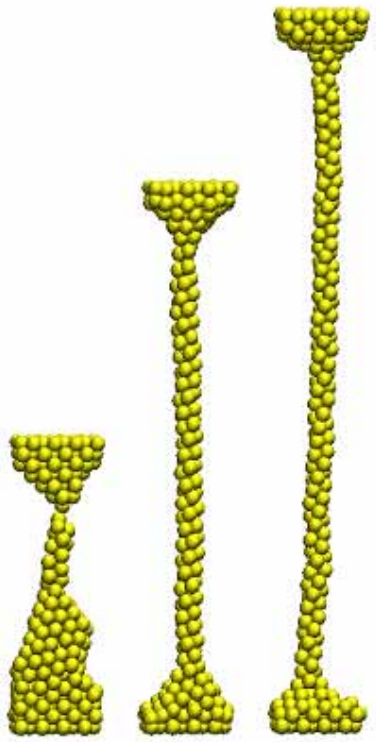

(a) (b) (c)

Figure 3.4. The snapshots of the break-junction structures for small Au (001) system at 298 K given by the three forcefields. (a) the TB-SMA result (2300 ps); (b) the glue model results (7080 ps), and (c) the EAM result (10320 ps).

3.3.3. Comparison in Elongation Dynamic Mechanisms between the TB-SMA Simulation and DFT Calculation

It should be noted that there are limits on the range of validity of the TB-SMA. For example, the TB-SMA does not predict planar structures for very small gold clusters[74,75] in which the coordination numbers of all the Au atoms are extremely small. For the system sizes of this work, however, the validity of the TB-SMA in the generation of monatomic gold chains is confirmed through higher-level DFT calculations. We further our investigation to clearly visualize the atomistic aspects of nanowire elongation process. By using a small Au (001) system with a total of 256 gold atoms at 0.01 K and allow the system to relax for 60,000 time steps prior to pulling, we get monatomic chains with 5 gold atoms suspended between two tips using the TB-SMA potential. Now we allow for full atomic relaxation within DFT for the selected TB-SMA configurations as shown in Figures 3.5.

The relaxation in general shows that the TB-SMA images are very similar to the DFT local energy minima, giving support for the choice of the TB-SMA classical potential as the tool of preference for elongation studies. There are, however, several noticeable differences between the two (TB-SMA and DFT) relaxed sets of images. Although the complexity of intermediate structures makes it difficult to describe these differences in great detail, the main features we found are as follows. For both TB-SMA and DFT, the initial cylinder (elongation $\Delta z = 0$ Å) contracts without disruption of the original FCC bonding network. The contraction is larger for DFT-LDA compared to the TB-SMA potential, and it is largest in the mid-region of the cylinder. These features are found also in the next two ($\Delta z = 3.9$ and 7.9 Å) intermediate images, albeit the differences in relaxation are more significant and can't be described simply as unequal

degrees of contraction. In the fourth image (Δz = 11.9 Å), there are three rings with 4 Au atoms each in the neck.

DFT-LDA relaxes the disordered TB-SMA configuration so that the planes of all three rings are almost parallel to each other, and the middle ring is almost at 45 degrees to the other two. In the fifth image (Δz = 15.9 Å), the mid-region of the neck consists of three pairs of Au atoms approximately in the xy plane. The TB-SMA potential places the central pair perpendicular to the other two, whereas LDA-DFT relaxes it so that all pairs are pointing in almost the same direction which is close to the (1-10) axis. In the sixth image (Δz = 19.9 Å), the centre of the neck is one-atom thick with two Au atoms in sequence supported by a pair of atoms on either side. LDA-DFT relaxation does not affect a strong change in the structure, only changes in bond lengths and angles that favor overall higher coordination. The same is true for the seventh image (Δz = 23.9 Å) which has a one-atom thick, five-atom long Au wire formed between the two tips. Finally, in the eighth image (Δz = 25.9 Å), the monatomic-chain is broken and the bottom tip exhibits an asperity in the form of two Au atoms protruding out of a semi- conical base. DFT-LDA changes partially the protruding character, leaving only one Au atom on top of a more symmetrical cone.

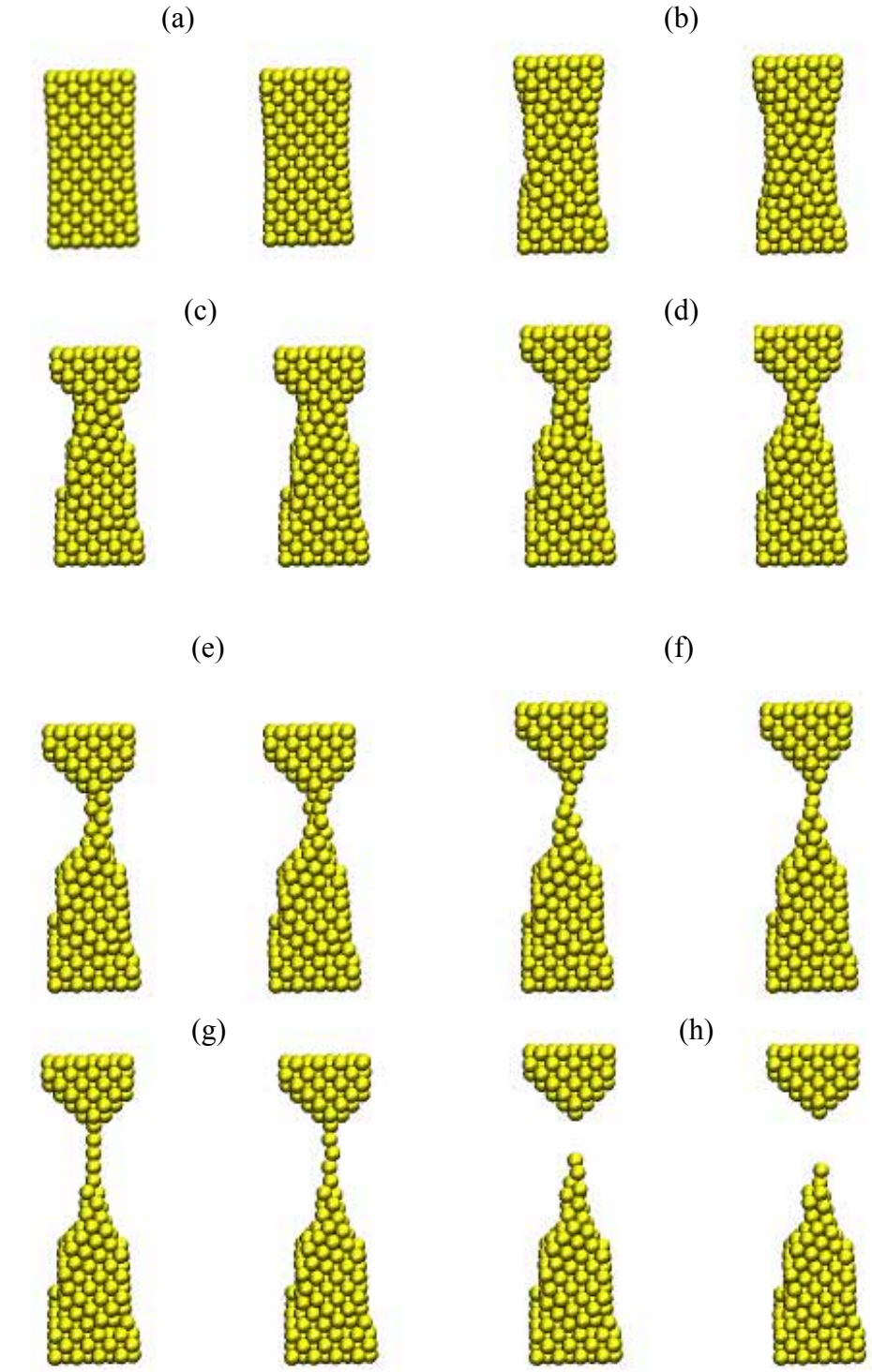

Figure 3.5. Snapshots of atomic configurations from MD (TB-SMA potential)(left) and DFT (right) studies for Au (001) at 0.01 K. (a) Δz = 0Å; (b) Δz = 3.9Å;(c) Δz = 7.9Å; (d) Δz = 11.9Å; (e) Δz = 15.9Å; (f) Δz = 19.9Å; (g) Δz = 23.9Å; (h) Δz = 25.9Å.

3.3.4. Mechanical Responses of Elongation of Au Nanowires

In order to further verify that the TB-SMA potential can properly predict the force needed to break a gold monatomic chain, we have performed MD simulations for the elongation of Au nanowires along [001] direction for a relatively larger system; the Au nanowire has 32 layers of gold containing 3254 atoms as shown in Figure 3.6 (a). (The notched wire in this case is to aid the breakup at the central part of the wire). Figure 3.7 shows the sawtooth variation of the tensile force applied along the monatomic chain direction versus the elongation length. In the stages with a linearly growing tensile force the nanowire is elastically stretched with accumulation of elastic energy, while at the force jumps, abrupt atomic rearrangement occurs and the accumulated strain energy is released. Some of the force jumps correspond to the incorporation of an extra gold atom into the bridging atomic chain while other jumps originate from atomic rearrangements occurring in the region close to the chain. The tensile force is recorded after each relaxation is completed. The numbers (1) to (5) in Figure 3.7 mark the occurrence of 1 to 5 monatomic atoms in the break junction. We find that the incorporation of new atoms in the break junction corresponds to the large jumps of tensile force in our simulation. Just before the breakup, the calculated tensile force is around 1.5 nN, which is in good agreement with the STM experimental result (1.5±0.3 nN).[10]

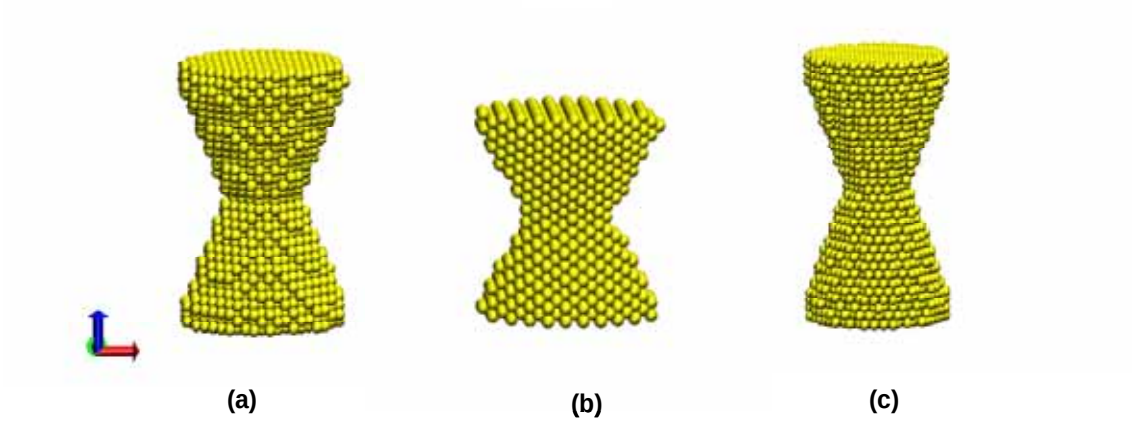

Figure 3.6. Initial configurations of Au nanowires for MD simulations. The diameters of the thinnest parts are 18.6Å and the diameters of the rigid layers are 40.8 Å.(a) Au (001), 32 layers, 3254 gold atoms; (b) Au (110), 32 layers, 2290 gold atoms; (c) Au (111), 33 layers, 3916 gold atoms.

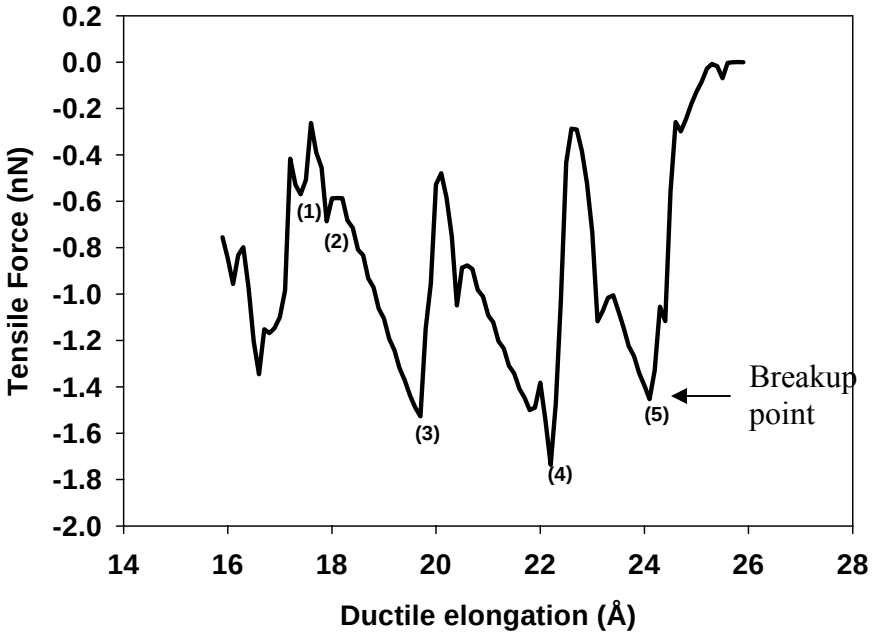

Figure 3.7. The variations of the tensile force as a function of the elongation length predicted by the TB-SMA potential, starting at the formation of monatomic chains. The atomic system corresponds to the large Au (001) system at 0.01 K. The numbers (1) to (5) mark the occurrence of 1 to 5 monatomic atoms in the break junction.

It is clear that the TB-SMA potential is the optimum potential out of the three commonly used classical potentials. Next, we concentrate our study on investigating the dynamic elongation properties of gold nanowires under various conditions using the TB-SMA potential. The results from glue model or the EAM potential are presented for comparison only.

3.4. Structural Evolution of Au Nanowires under Stretching

A systematic study of the effects of crystallographic orientation, length, elongation rate, temperature as well as initial configuration on the ductile elongation properties of nanowires take into account a variety of experimental conditions.

3.4.1. Large System Study

3.4.1.1. Effect of Crystallographic Orientation and Temperature

We study the elongation configurations for the large system with gold atoms oriented along (001), (110), and (111) directions (see Figure 3.6) at two temperatures, 0.01 K and 298 K. Starting from the same crystallographic orientation to elongate the initial unrelaxed nanowires, the TB-SMA potential and the glue model lead to different rupture structures. For the TB-SMA potential, the formation of monatomic chains range from two to five atoms in the middle of the contact has been observed. The numbers of monatomic atoms in the break junctions depend on the crystallographic orientation as well as temperature as shown in Figure 3.8 and are given in Table 3.3. By comparison, the rupture structures for the glue model are independent of the crystallographic

orientations. At lower temperature, there is always one gold atom on the upper and two gold atoms on the lower side in the break-junction. At higher temperature, the rod-like rupture structures are observed typically containing 2 to 3 gold atoms in the cross sections.

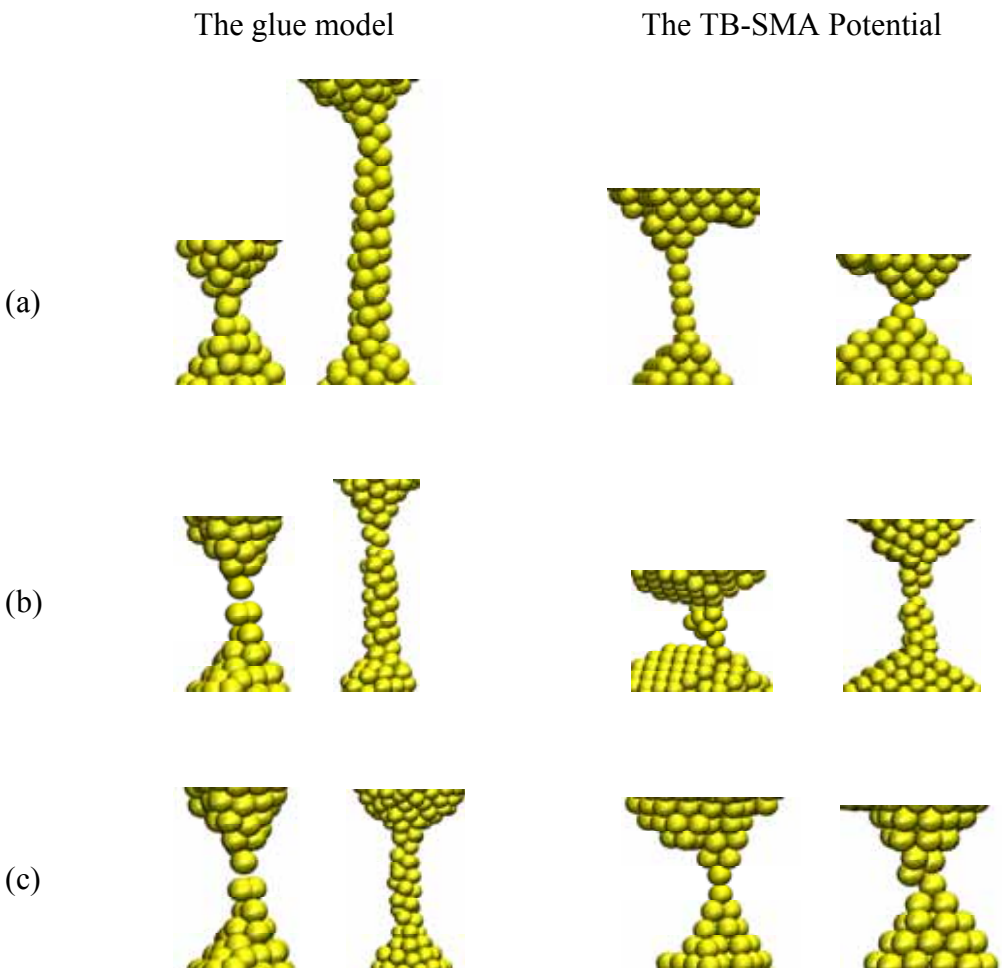

Figure 3.8. Snapshots of break junction structures for (a) Au (001), (b) Au (110) and (c) Au (111) at temperatures 0.01 K (left) and 298 K (right) for glue model and TB-SMA potential.

Table 3.3. The numbers of monatomic atoms in the break junctions for Au (001), Au (110) and Au (111) at temperatures 0.01 K and 298 K.

Temp.	0.01 K			298 K		
	Au (001)	Au (110)	Au (111)	Au (001)	Au (110)	Au (111)
TB-SMA	5	0	2	0	2	0

The formation of monatomic chain structures has been observed in several experimental studies.[16,49,52] The consistency of the TB-SMA results with experimental observations verified that the TB-SMA potential has the ability to realistically describe the experimentally generated nanowire break junctions. With regard to temperature effects, Table 3.4 lists the ductile elongation as function of temperature for various crystallographic orientations and forcefields. The ductile elongation here means the length increment of the nanowires in *z* direction upon break compared to the original length with an asterisk (*) on the upper right corner indicating the occurrence of monatomic chains. It is noted that at lower temperature 0.01 K, the values of the ductile elongation are in the narrow range from 22.4 Å to 25.6 Å regardless of the forcefields applied except for Au (110), which breaks much earlier at ductile elongation value of 14.4 Å using the TB-SMA potential. At the elevated temperature 298 K, for the TB-SMA potential, the difference between the values of the ductile elongation at various temperatures can be ignored for crystals oriented along (001) and (111) directions. The only difference is the value of ductile elongation for Au (110), which is 21.2 Å at 298 K, ~7 Å higher than that of at 0.01 K. The situation is quite different for the glue model. At 298 K, the values of ductile elongation show high ductility, ranging from 1.37 to 1.95 times higher than those of at 0.01 K. The necks become very long before the fracture eventually occurs. Additionally, before breakage, the necks are composed of more than ten layers of gold atoms in clusters of three to four atoms in the cross section, persisting over 1.5 ns.

Table 3.4. The ductile elongation as function of temperature for Au (001), Au (110) and Au (111) nanowires.

Temp.	0.01 K			298 K		
Forcefields	Au (001)	Au (110)	Au (111)	Au (001)	Au (110)	Au (111)
Glue Model	23.6 Å	25.6Å	22.8 Å	46Å	40.6Å	31.2Å
TB-SMA	24 Å *	14.4Å	22.4 Å *	21.2Å	21.2Å *	21.2Å

* Monatomic chains occurred

3.4.1.2. Effect of Initial Configuration

The absence of a published statistical analysis of the occurrence of monatomic chains led us to perform such a study, since the results can provide a way to predict break-junction structures. Thirty simulations were initialized with thirty different configurations, which were then elongated to produce gold nanowires break junctions. Figure 3.9 provides the statistics on the distribution of the numbers of monatomic atoms in the final break-junction structures just prior to rupture using the TB-SMA potential. At the lower temperature 0.01 K, Au (110) and Au (111) appear to be deterministic (i.e., all simulations led to the same result): no monatomic chains were found for Au (110), while two-atom-long monatomic chain structures arise for Au (111) for all studied initial conditions. The numbers of monatomic atoms for Au (001) vary from zero to five with 43% of cases showing the monatomic chain structures of five atoms in length. When the temperature is elevated to 298 K, the numbers of the monatomic atoms in the break-junction exhibit wide distributions. For Au (110), compared to no monatomic chain structures occurring at 0.01 K, one atom suspended between two gold tips is found in 30% of cases and two monatomic atom structures are found in 43% of cases. For Au (111), two-atom-long monatomic chain structures are found in about half of the cases, while another 40% of cases exhibit single-atom monatomic chain structure. For Au (001), the numbers of monatomic atoms vary from zero to four with one, two or four suspended Au atoms accounting for 37%, 10% and 3% of cases respectively.

The rupture structures are dependent on initial configurations. It appears that the (001) wires can produce monatomic chains because that there is a stacking fault formation on the side of the conical base. This may account for the orientation

dependence of the formation of monatomic chains. Moreover, at lower temperature, monatomic chains show a rather narrow distribution at break junction structures. At higher temperature, monatomic chains are distributed more broadly due to the thermal fluctuations.

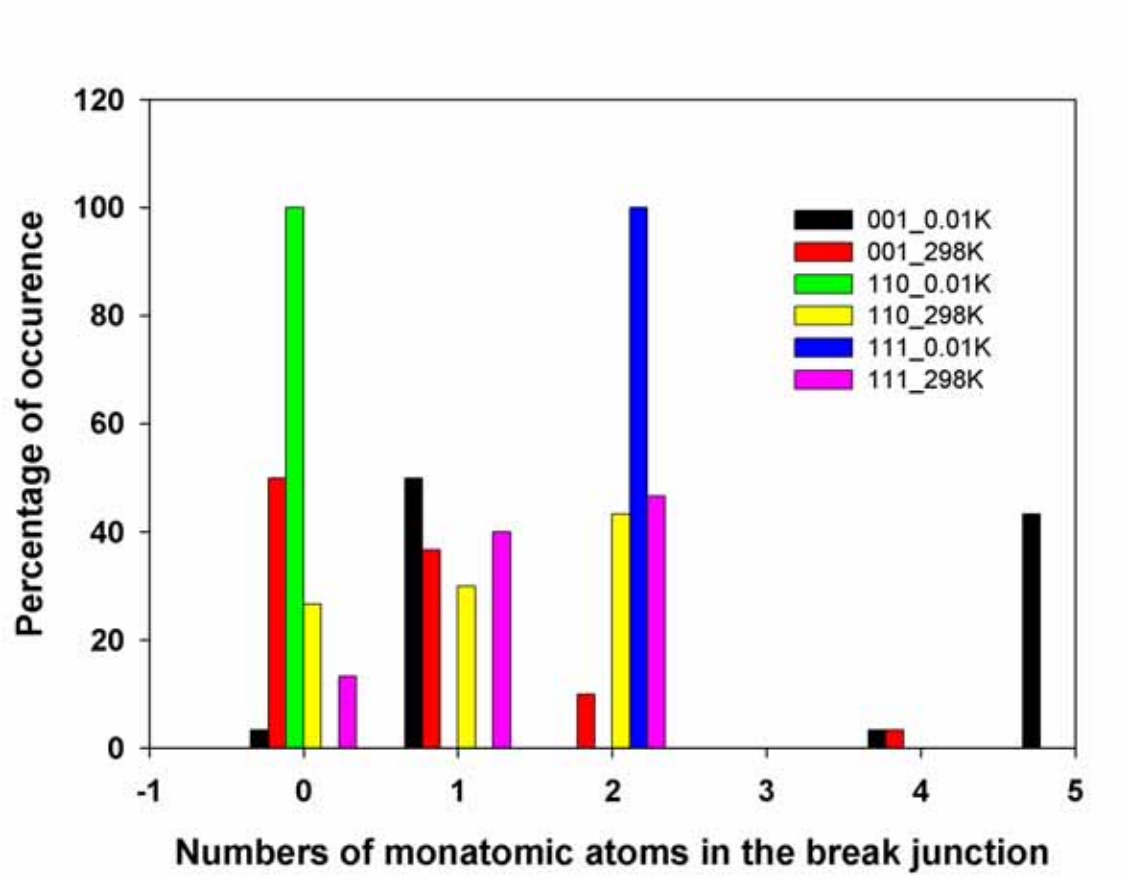

Figure 3.9. The numbers of monatomic atoms distribution for different crystallographic orientations at two temperatures.

3.4.2. Small System Study

The interesting results of the statistical studies using large system encourage us to further our studies on investigating the effect of geometry, rate and temperature on the elongation properties of the nanowires. In this study, we give attention to the crystal which orientate along [001] direction only. The target nanowires vary in length (*z* direction). The shorter nanowires include 16 layers of gold atoms, for a total of 256 atoms (Figure 3.10 (a)); the longer nanowires include 28 layers of gold atoms, for a total of 448 atoms (Figure 3.10 (b)). Two layers at both ends are kept rigid. The atoms between these two blocks are dynamic. Elongation of the wire is realized by displacing the top rigid layers along the *z* direction in increments of 0.1 Å, while keeping the other end fixed. For every 0.1 Å increment the whole system is allowed to be relaxed for 5000, 50000 or 100000 time steps with a time step of 2 fs, corresponding to an elongation rate of 1.0, 0.1 and 0.05 m/s. All of the results shown below are based on statistical studies. In each case 30 independent MD runs are performed to obtain the average ductile elongations and the break-junction structures.

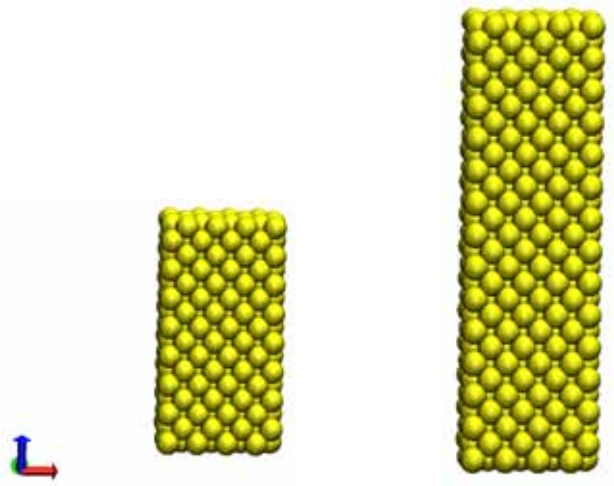

(a) (b)

Figure 3.10. Initial configurations of Au (001) nanowire. (a) 256-atom gold nanowire (b) 448-atom gold nanowire.

3.4.2.1. Effect of Length and Temperature

Keeping the dimension in *x* and *y* directions unchanged, we vary the nanowires' length from 30.6 Å (shorter nanowire) to 55.1 Å (longer nanowire) which corresponds to the increase of aspect ratio from 2.1 to 3.9. We investigate the effect of length and temperature on the ductile elongations at fixed elongation rate 1.0 m/s. Table 3.5 summaries the average ductile elongations at temperature 0.01 K, 300 K and 500 K respectively. It is found that the ductile elongations vary with temperatures for both nanowires, but with different trends. In order to explain the observed phenomena, we look into the probabilities on the formation of monatomic chains in the break junctions at three temperatures as shown in Figure 3.11 (for shorter nanowires) and Figure 3.12 (for longer nanowires).

The variations in temperature not only affect the ductile elongations, but also influence the stability of the nanowires. Figure 3.13 and 3.14 plot the center of mass of Au atoms in three directions *x*, *y* and *z* for the shorter wire and the longer wire at temperature 0.01 K and 300 K during the first 200 ps, respectively. It is obvious that the Au atoms only vibrate around their original positions at low temperature. However, at room temperature, the center of mass shows much more variations due to the thermal fluctuations. Moreover, the shorter the dimensions are, the severer the variation in center of mass.

Table 3.5. The average ductile elongations (Å) as a function of temperature for pulling nanowires in vacuum at elongation rate 1.0 m/s. The shorter nanowires include 16 layers of total 256 gold atoms; The longer nanowires include 28 layers of total 448 gold atoms.

	shorter wires	longer wires
0.01 K	18.8±2.1	30.7±12.0
300 K	18.3±4.1	21.3±7.4
500 K	15.8±3.1	12.8±3.2

Based on the statistical data in Table 3.5, we observe the following phenomena:

i) For low aspect ratio nanowires, the ductile elongations are similar at temperature 0.01 K and 300 K. In comparison, the average ductile elongations for the high aspect ratio nanowires decrease from 30.7 Å to 21.3 Å as the temperature increase from 0.01 K to 300 K. It is clearly illustrated in Figure 3.11 and 3.12 that the probabilities on the formation of long monatomic chains (over 2 atoms in length) increase from 13 % for shorter nanowires to 43 % for longer nanowires at 0.01 K. Meanwhile, the longest monatomic chain is 6 atoms in length for shorter nanowires. By comparison, for longer nanowires, the monatomic chains can be as long as 13 atoms in the break junctions. The high possibility on the formation of longer monatomic chain structures for high aspect ratio nanowires is related to the percentage of the atoms in the dynamic zone. The increase in the length of the nanowires makes more gold atoms incorporated in the process of forming monatomic chains. As for the shorter nanowire, 25% of the gold atoms (4 layers out of 16) have been restrained in the rigid layers. In comparison, only 14% of the gold atoms (4 layers out of 28) have been constrained in the rigid layers for the longer nanowires. Obviously, the more gold atoms involved in the dynamic zone, the higher the probability to form longer monatomic chains. This finding helps us explain the noteworthy high average ductile elongations for high aspect ratio nanowires at 0.01 K because normally the greater the number of the monatomic atoms in the break junctions, the longer the ductile elongations will be.

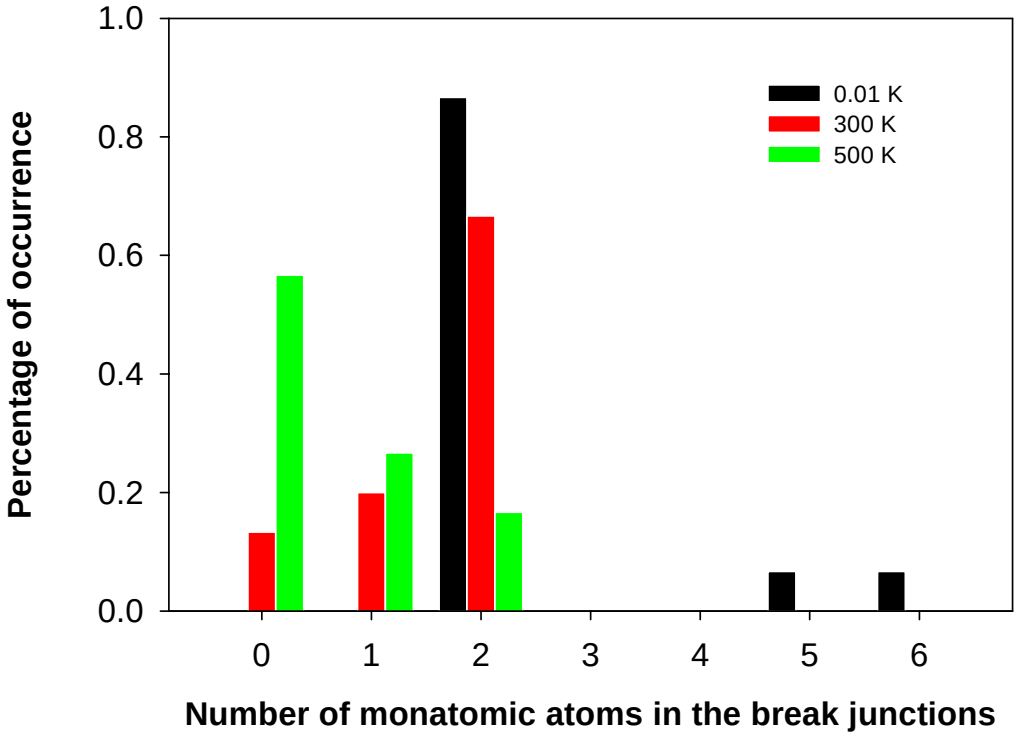

Figure 3.11. The probabilities of formation monatomic chains in the break junctions for 256-atom nanowires at elongation rate of 1.0 m/s.

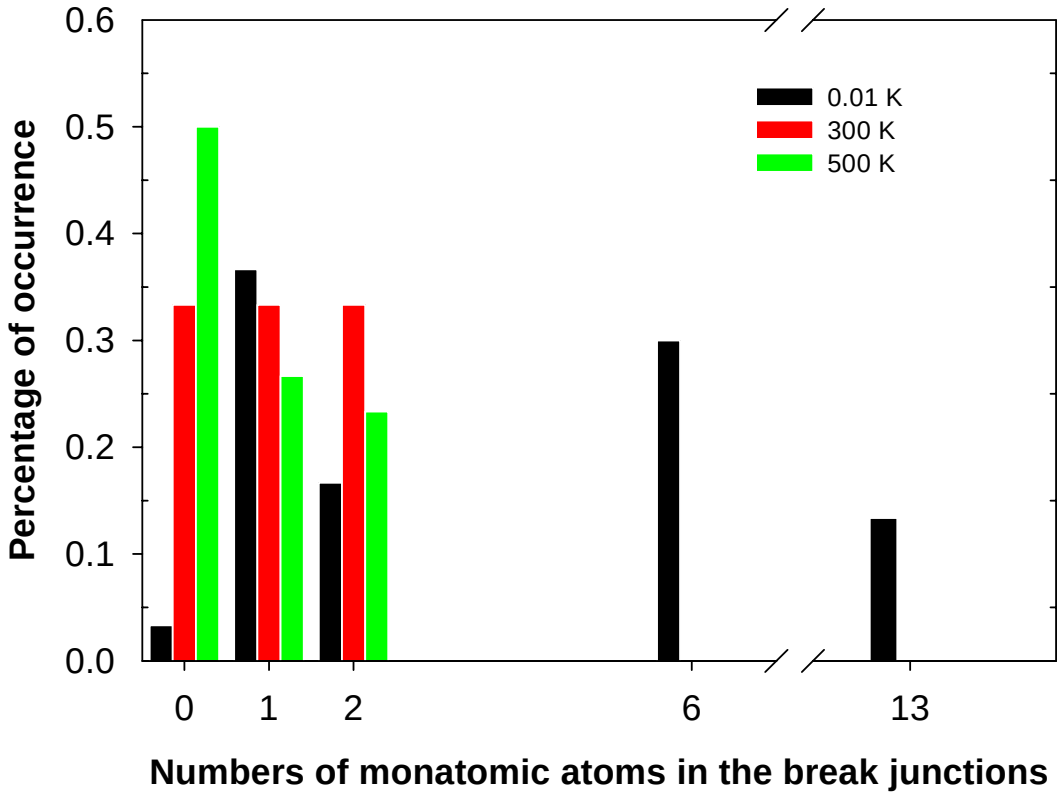

Figure 3.12. The probabilities of formation monatomic chains in the break junctions for 448-atom nanowires at elongation rate of 1.0 m/s.

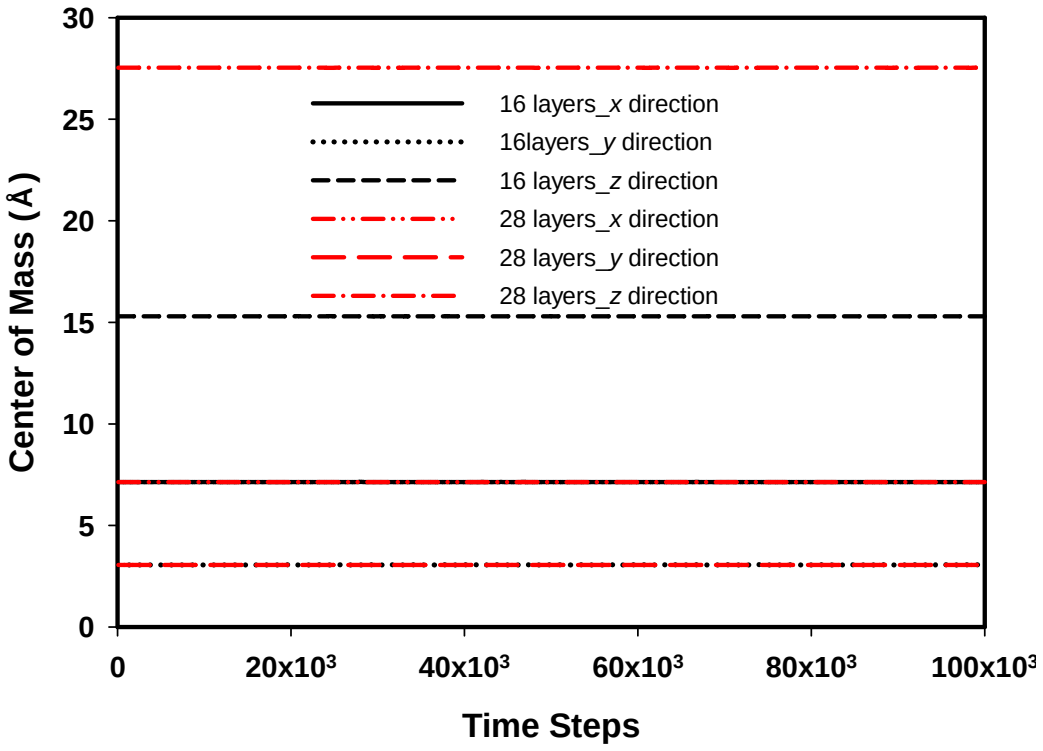

Figure 3.13. The center of mass of Au atoms in *x*, *y* and *z* directions for the 16layers and 28 layers nanowires equilibrium during the first 200 ps at 0.01 K.

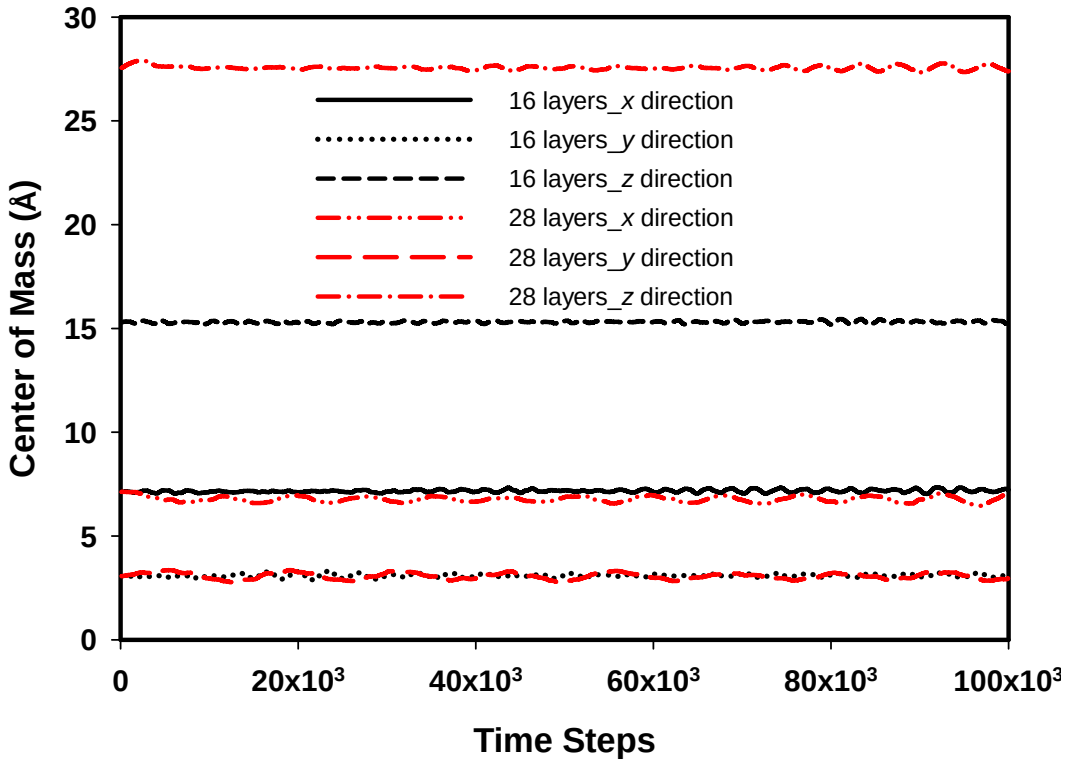

Figure 3.14. The center of mass of Au atoms in *x*, *y* and *z* directions for the 16 layers and 28 layers nanowires equilibrium during the first 200 ps at 300 K.

ii) When we further increase the temperature to 500 K, the average ductile elongations decrease considerably for nanowires in both lengths. From the figures, we find that no matter what lengths of the nanowires, the chances for the formation of longer monatomic chains decrease as the increase of the temperatures. At 300 K and 500 K, there is no single case of monatomic chains over two atoms long. Moreover, the chances for no monatomic chains formation increase further at 500 K. The formation of longer monatomic chains is very sensitive to the structural properties of the nanowires. Only very stable structures along the elongation path make more atoms in the monatomic chain possible. The increase in the temperature destroys such stable structures due to the strong thermal fluctuations, which induces the disappearance of the longer monatomic chains. As a consequence, the shorter monatomic atoms in the break junctions count as one of the reasons for the reduced ductile elongations at high temperatures. The other reason is that the formation of the neck can initiate as early as in the initial relaxation stage prior to pulling at temperature 500 K. The distortions of the configurations make the fracture of the nanowires much easier (a typical initial configuration is shown in Figure 3.15 (a)).

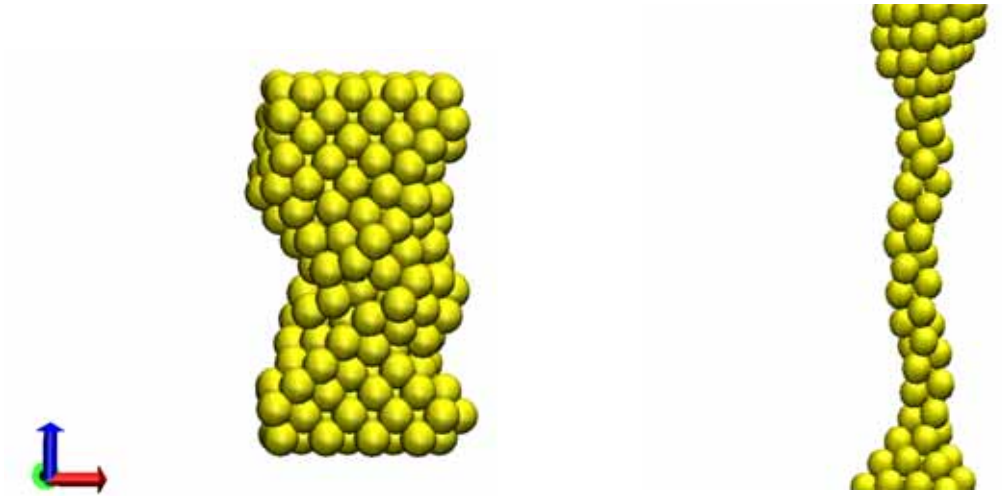

(a) (b)

Figure 3.15. The necking formation prior to pulling at 500 K (a) and the formation of multishell break-junction structure at 300 K (b).

3.4.2.2. Effect of Elongation Rate

In order to identify if the elongation rate has effect on the ductile elongations, we decrease the rate from 1.0 m/s to 0.1 m/s and 0.05 m/s. Table 3.6 (for shorter nanowires) and Table 3.7 (for longer nanowires) list the ductile elongations at elongation rates 0.1 m/s and 0.05 m/s respectively at three temperatures. We find the following trends:

i) Unlike the case of elongation of nanowires at 1.0 m/s, the average ductile elongations at 300 K are slightly higher than those at 0.01 K for both shorter and longer nanowires. By pulling the nanowires slower at 0.01 K, we notice that the longer monatomic chain structure completely disappears. For the shorter nanowires, there is no monatomic chain over two atoms long formed. The longest chain structure becomes 2 instead of the 6 found previously when elongating nanowires at rate 1.0 m/s. As for the longer nanowires, only one 9-atom-long monatomic chain structure appears. The probability on the formation of long monatomic chains more than two atoms long at 0.01 K decreases from 43% to 3% as a result of lowering the elongation rates only. One of the possible reasons for the disappearance the long monatomic chain structures at lower elongation rates could be due to the greater relaxation time allowed for the gold atoms. The adequate relaxation of the atoms generate fewer defects in the nanowires, which in turn results in the formation of more brittle like, shorter chain structures in the break junctions. Therefore, the reduction in the numbers and possibilities of the formation of monatomic chains definitely accounts for the decreased average ductile elongations at 0.01 K. From the point view of 300 K situation, we find the formation of the helical, zigzag type chains (see Figure 3.15 (b)) in the break junctions as the elongation rate is lowered, especially for high aspect ratio nanowires. This type of break-junction structure

has been observed previously in MD simulations[61,62] to generate quite long ductile elongations. In our simulation, for example, 27% of the 448-atom nanowires elongated at rate 0.05 m/s form long zigzag long chain with ductile elongations over 35 Å. In summary, the comparably longer ductile elongations at 300 K not only contribute to the formation of shorter monatomic chain structures at 0.01 K but also to the formation of longer zigzag type chain structures at 300 K.

Table 3.6. The average ductile elongations (Å) as a function of temperature for pulling the shorter nanowires in vacuum at elongation rate 0.1m/s and 0.05 m/s.

	0.1 m/s	0.05 m/s
0.01 K	15.1±0.4	15.3±0.0
300 K	16.1±6.9	16.7±3.5
500 K	7.8±1.2	6.2±0.9

Table 3.7. The average ductile elongations (Å) as a function of temperature for pulling the longer nanowires in vacuum at elongation rate 0.1m/s and 0.05 m/s.

	0.1 m/s	0.05 m/s
0.01 K	19.9±4.2	18.8±4.7
300 K	22.9±7.4	24.3±9.3
500 K	4.8±1.4	3.2±1.5

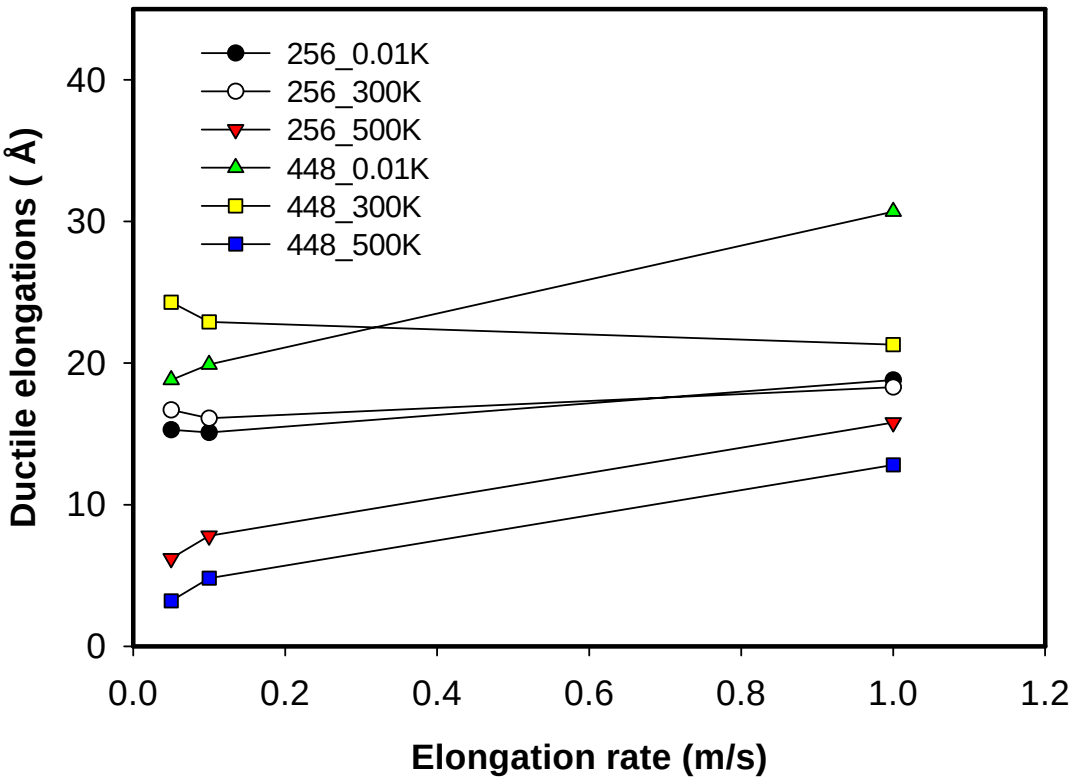

Figure 3.16. The ductile elongations as a function of elongation rate for various wire sizes at three temperatures.

ii) Figure 3.16 plots the ductile elongations as a function of elongation rate for both sizes of nanowires at three different temperatures. This figure provides us with a complete picture of the elongation rate dependent behavior. In most cases, the ductile elongations increase with increasing elongation rate, mainly originating from the formation of longer monatomic structures at high elongation rate. Some exceptions apply to the cases described before when longer zigzag-type chain formed (e.g. 448-atom nanowires elongated at rate 0.05 m/s), which bring in the higher ductile elongations at 300 K and at low elongation rate. Furthermore, the ductile elongations at 500 K turn out to be very small compared with the cases at 0.01 K and 300 K for both nanowires, particularly for the high aspect ratio nanowires.

3.5. Conclusions

Firstly, we have performed MD simulations combined with DFT energy calculations to investigate the mechanical elongation behavior of finite gold nanowires. The DFT energy calculations verify that among the three typical semi-empirical potentials (i.e., the glue model, the EAM and the TB-SMA potentials), the TB-SMA potential is the most suitable forcefield to describe the structural and mechanical properties of gold nanowires during elongation. Using the TB-SMA potential, we find that elongation of gold nanowires leads to the formation of monatomic chains, as observed by many experiments and the TB-SMA potential can correctly predict the breakup force.

Secondly, MD simulations have been conducted to study the impact of the crystallographic orientation, length, rate, and temperature on the ductile elongation

properties of nanowires with either large system or small system. For the small system study, we perform all our simulations using statistical approaches (i.e., multiple realizations of the simulations). The results show that a combination of low temperature with high elongation rate is necessary to form monatomic chains with more than two atoms in length. Furthermore, increasing the length of the nanowires assists the formation of longer monatomic chains in the break junctions at 0.01 K. In contrast, high temperature or low elongation rate diminish the probability of the formation of the long monatomic chain structures. Moreover, a combination of high temperature (300 K) with low elongation rate makes the formation of the helical, zigzag-type break-junction structures feasible.

CHAPTER IV

DYNAMIC ELONGATION OF NANOWIRES IN PROPANE

4.1. Introduction

Theoretical studies on the dynamic elongation process of the nanowires have typically been conducted in vacuum. There are extensive simulation studies devoted to the investigation of the quantized conductance properties by DFT calculations, [76-79] but usually the impact of the local environment, such as solvent effects, on the formation of the junctions is neglected. Csonka *et al.*[76] investigated the interaction of physically adsorbed molecular hydrogen with a breaking gold nanowire. Li *et al.*[77] demonstrated that the weak adsorption of organic molecules (2, 2'- bipyridine or adenine) on a copper nanowire resulted in changes in conductance. Most of the experimental conductance measurements of metal-molecule-metal junctions were performed in solvent and the junctions were fabricated through mechanical stretching of the nanowire.[4,48] Therefore, it is desirable to study the solvent effects on the elongation properties of nanowires in order to understand better the electronic properties of the molecular conjunctions. In this chapter we attempt to simulate the elongation of gold nanowires in a simple solvent through large-scale molecular simulations.

We investigate the dynamic elongation behavior of Au nanowire immersed in a simple nonpolar solvent, propane (C_3H_8). The purpose of this study is to understand to what extent the thermal collisions of nonbonded particles will influence the mechanical elongation property of Au nanowires. Propane is a three-carbon alkane with critical

pressure and temperature of 42.5 bar and 370 K, respectively. We performed MD simulations at temperatures of 300 K, 400 K and 500 K, respectively. The results revealed that when the temperature is well below the melting point of gold nanowires, there is essentially no effect of propane solvent on the elongation behavior of Au nanowires.

4.2. Simulation Details

4.2.1. Forcefields

In this study, the interactions between gold atoms were calculated by the TB-SMA[59] potential, as described in Chapter III. We approximate this short chain molecule by a spherical Lennard-Jones (LJ) particle. Interactions between solvent molecules and between gold atoms and propane molecules are described by the 12-6 LJ potential, i.e., for a pair of interacting sites *i* and *j*, the pair potential is given by

$$U_{ij}^{LJ} = 4\varepsilon_{ij}\left[\left(\frac{\sigma_{ij}}{r_{ij}}\right)^{12} - \left(\frac{\sigma_{ij}}{r_{ij}}\right)^{6}\right] \tag{4-1}$$

The cross interaction potential parameters ε_{ij} and σ_{ij} are calculated from Lorentz-Berthelot combining rules if interacting sites *i* and *j* are different species. The LJ parameters for gold atoms are derived from the universal forcefield (UFF).[80] The UFF developed by Rappe *et al.*[80] has been parameterized for the full periodic table. The set of fundamental parameters is based only on the element, its hybridization, and connectivity. In this forcefield, the potential energy for a molecule is written as a superposition of various

two-body, three-body, and four-body interactions. The LJ parameters for propane are calculated according to the corresponding state theory[81] so that the LJ fluid has the same critical temperature and pressure/density as propane. All the LJ parameters used in this work are summarized in Table 4.1.

Table 4.1. Lennard-Jones parameters for Au and propane.

	ε (kcal/mol)	σ (Å)
Au /Au	0.039	2.934
propane / propane	0.553	4.66
Au / propane	0.147	3.797

4.2.2. Simulation Methodology

We have performed MD simulations for the elongation of an Au nanowire along the [001] direction both in vacuum and in solvent at various temperatures. The nanowire includes 16 gold layers with each layer containing 16 Au atoms, so the total number of gold atoms is 256 (see Figure 4.1 (a)). Two layers at both ends are kept fixed. The atoms between these two blocks are dynamic. Similar to the simulation method description in Chapter III, elongation of the nanowire is realized by moving the top rigid layers along the *z* direction in increments of 0.1 Å, followed by 5000 time steps for relaxation, with a time step of 2 fs. This corresponds to an elongation rate of 1.0 m/s. We found that this relaxation time is sufficient for a quasi-static stretching of gold nanowires either in vacuum or in propane solvent. The equations of motion are integrated via the velocity Verlet algorithm and the temperature is controlled by the Nosé–Hoover thermostat on the dynamic Au atoms only.[66-68] Periodic boundary conditions (PBC) are applied in three dimensions. However, in simulating the elongation of nanowire in vacuum, adding or removing PBC has no effect on the simulation results, as long as the simulation box lengths are sufficiently large. Figure 4.1 (b) shows the equilibrium structure of 1298 propane molecules surrounding a gold nanowire. Unlike the slightly relaxed structure of 256-Au nanowire at T = 0.01 K,[82] the relaxed crystal structures of 256-Au wire in vacuum and in solvent at 300 K show significant reconstructions, accompanied by the formation of dislocations (see Fig. 4.1). For the simulation of 256-Au wire in propane solvent, we initially performed the constant temperature and constant pressure (*NPT* ensemble) MD run for pure propane (containing 1372 propane molecules) under its critical pressure (42.5 bar) but at 300 K, which is below its critical temperature (370 K).

The final equilibrium volume of simulation box is $6.1 \times 2.6 \times 13$ nm^3, corresponding to a density of 0.47 g/cm^3. This value is consistent with other MD simulation and experimental results.[83] The 256-Au wire was then put into the center of simulation box. All the overlapped propane molecules were removed from the simulation box. This treatment will slightly change the system pressure; however, we will show later that the effect of pressure variation upon the elongation process is negligible compared with that due to temperature variations.

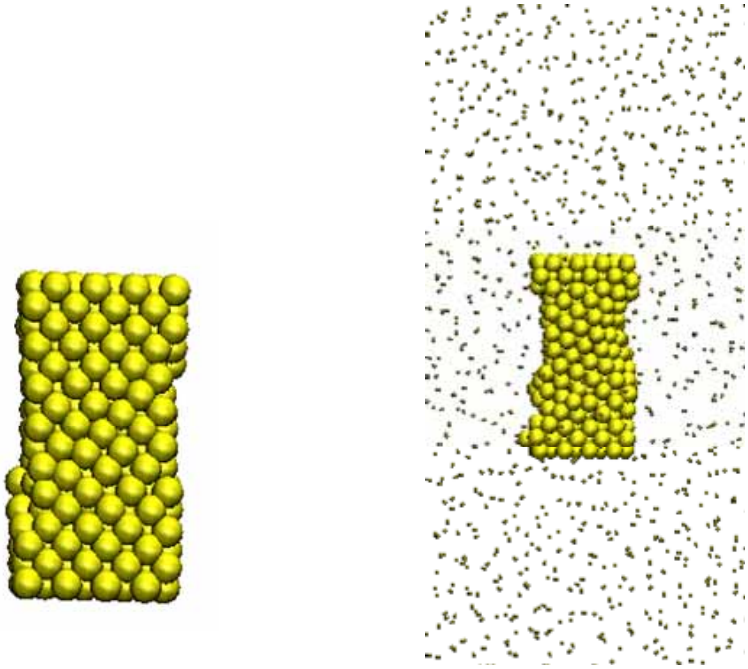

(a) (b)

Figure 4.1. Initial configurations of 256-Au (001) nanowire in vacuum and in solvent. (a) 256-atom gold nanowire relaxed 20 ps at 300 K ; (b) 256-atom relaxed nanowire in propane solvent. The dimension of the solvent box is 6.1 x 2.6 x 13 nm^3.

4.3. Effect of Propane Solvent on the Ductile Elongation of Nanowires at Various Temperatures

We investigate the effect of propane solvent on the elongation properties of the 256-atom Au (001) nanowires at different temperatures by comparing the average ductile elongations in the two cases. Figure 4.2 shows two snapshots of the elongated nanowires in vacuum and in propane solvent before breakup at 300 K. In this specific case, it is seen that the break junctions in vacuum and in solvent occur at different locations. Since the break-junction phenomenon is largely stochastic in nature, we therefore performed thirty independent MD runs of elongation in vacuum and another thirty runs in propane solvent for comparison. Table 4.2 summaries the calculated average ductile elongations, together with the standard deviations at different temperatures. It is interesting to note that, for the gold nanowires elongated both in vacuum and in propane solvent, the ductile elongations decrease with increasing temperature. Moreover, the average ductile elongations of gold nanowires in vacuum and in solvent are almost the same at temperatures of 300 K and 400 K. It should be noted that at 400 K, the corresponding pressure of liquid propane is increased to 500 bar.[83] It seems that this one order of magnitude increase in pressure has virtually no impact on the elongation of the nanowire. However, the solvent effect becomes significant only at temperature of 500 K (the corresponding pressure is ~1000 bar).[83] The average ductile elongation of Au nanowire in propane solvent is 12.35± 2.82 Å, less than that of gold nanowire in vacuum (15.83±3.07 Å).

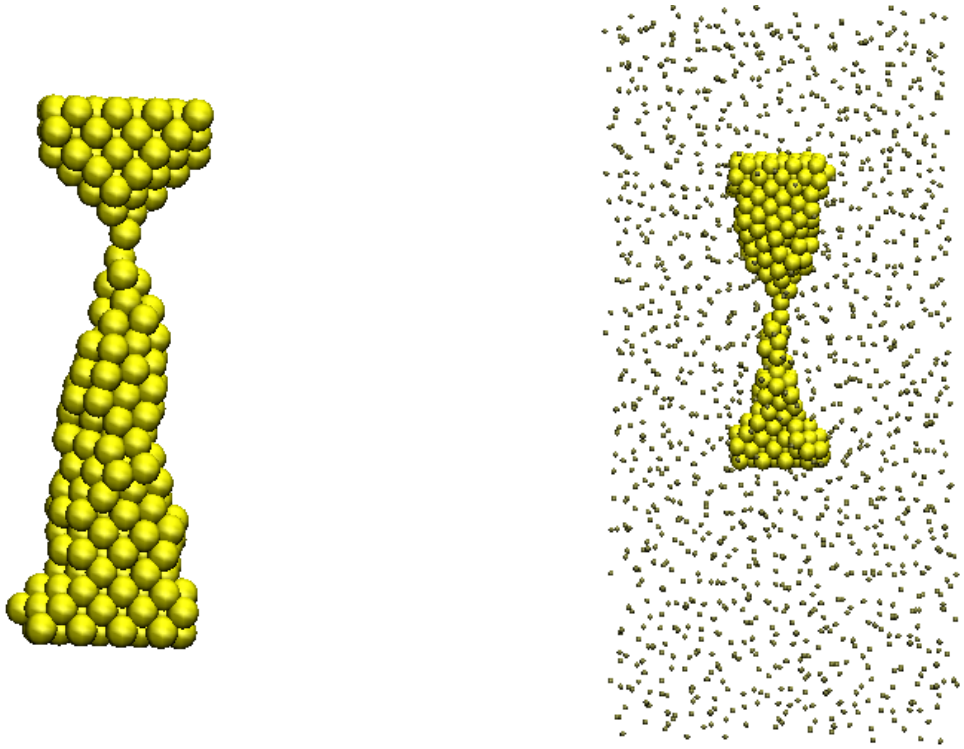

(a) (b)

Figure 4.2. Break-junction configurations of 256-Au (001) nanowire in vacuum and in solvent. (a) 256-atom gold nanowire elongated in vacuum at 300 K; (b) 256-atom gold nanowire elongated in solvent at 300 K.

Table 4.2. The variations of the ductile elongations as a function of temperature for Au (001) nanowires in vacuum and in solvent.

	nanowires in vacuum (Å)	nanowires in solvent (Å)
300 K	18.3±4.1	18.8±4.4
400 K	16.2±4.2	16.5±3.5
500 K	15.8±3.1	12.4±2.8

It is valuable to investigate further why the solvent has an effect only at relatively high temperature (500 K). To understand this phenomenon, we plot the caloric curve, the variation of the total energy of the 256-Au nanowire versus temperature, and the diffusion coefficient of gold atoms as a function of temperature, as shown in Figure 4.3. Evidently, there is a linear increase regime for the total energy of gold wire and the diffusion constant of gold atoms at relatively low temperature, corresponding to a crystal structure of the Au cluster. The abrupt jumps in both quantities around 550K signify that the melting point (T_m) of the gold cluster is around this value, consistent with several previous studies.[84-86] This melting point of a finite gold cluster is much lower than the bulk value. These calculation results indicate that the solvent effect on the elongation of Au nanowire becomes significant only when the temperature approaches the melting point.

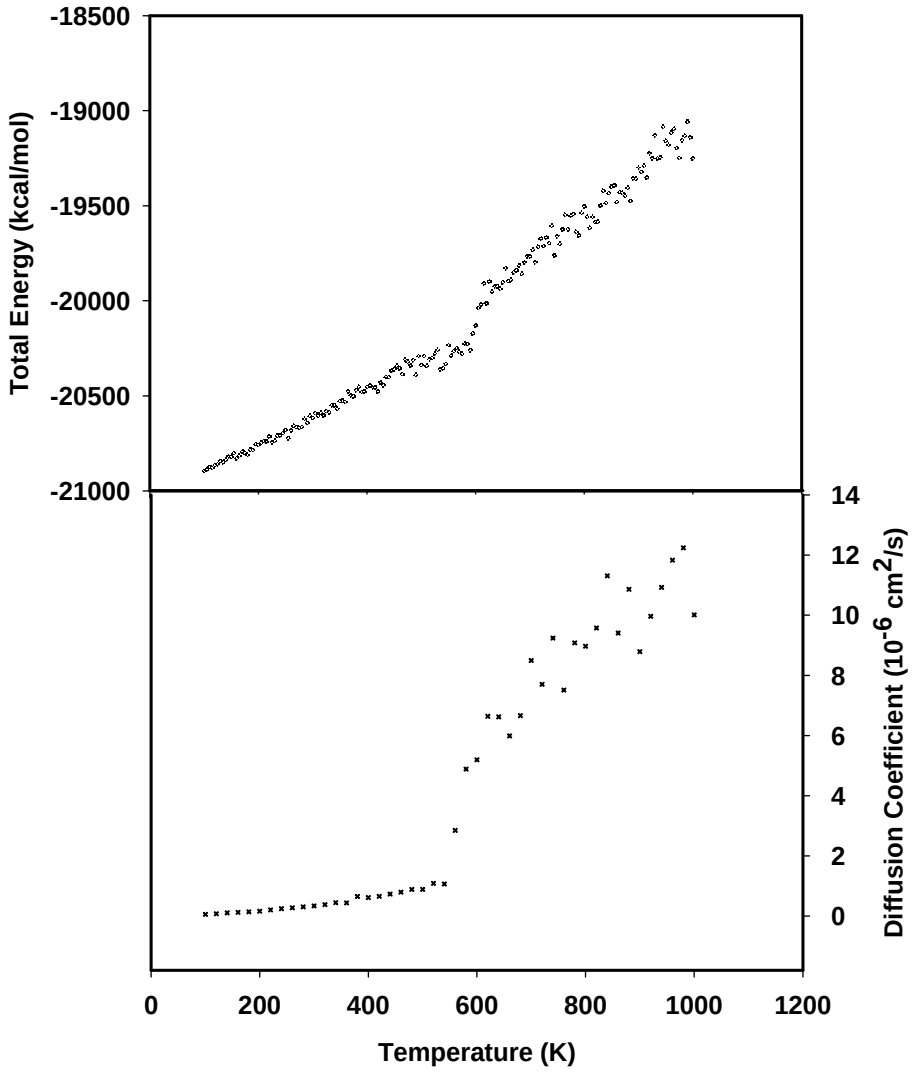

Figure 4.3. The caloric curve and the diffusion coefficient as a function of temperature for nanowire in vacuum.

4.4. Conclusions

The MD simulation studies explored the solvent effects on the elongation properties of gold nanowires. A simple Lennard-Jones spherical model for propane has been used to represent the solvent molecules in order to test the influence of the thermal collisions of nonbonded particles on the mechanical elongation property of Au nanowires. Propane does not form chemical bonds with Au atoms.

Simulation results demonstrated that the solvent effect is minimal if the temperature is below the melting point of gold nanowire. However, when the temperature approaches the melting point, the average ductile elongation of Au nanowire in propane solvent is 22 percent less than that of gold nanowire in vacuum.

CHAPTER V

SELF-ASSEMBLY OF BENZENEDITHIOL ON NANOWIRES

5.1. Introduction

In the pioneering work by Reed *et al*.[4] on the single-molecule current-voltage (as well as conductance) measurements, the gold wire was pulled apart in tetrahydrofuran (THF) solvent containing BDT molecules. The self-assembly of BDT on Au wire is the key component in establishing a metal-molecule-metal junction. As noted in chapter II, self-assembled molecular electronic systems composed of many single-molecule devices are the most promising path to future computers with ultra-dense, ultra-fast, molecular-sized components, and as the likely candidate to continue Moore's law beyond silicon technology. However, there exist formidable barriers to their practical implementation. Experiments in molecular electronics are both difficult and very expensive, and have frequently been the subject of large lab-to-lab discrepancies. A comprehensive theoretical framework is thus needed, especially for the prediction of electron transport in single molecules in their real environment (i.e., in a single-molecule experiment or at a system level in a working device). Significant theoretical issues must be resolved to make such modeling capability a reality. Many experimental measurements have shown that the microscopic contact geometry at BDT-Au interface has dramatic influence on the conductance.[87,88] Therefore, it is valuable to obtain the local bonding structures of BDTs on Au nanowires at specific temperatures via classical molecular simulations. In this

chapter, we present GCMC simulation results of the structure of BDT molecules adsorbed on Au nanowires.

5.2. Simulation Details

5.2.1. Forcefields

To simulate the adsorption of BDT molecules on gold nanowires, BDT molecules are modeled as rigid molecules. The potential model for BDT molecules employed are based on the universal forcefield (UFF)[80] plus Mulliken partial charges derived from recent *ab initio* calculations.[45] The non-bonded interactions between gold atoms and BDT molecules are modeled by Lennard-Jones pair potentials from UFF. The chemical bonding between the sulfur atom in BDT and Au atoms are modeled by Morse potential. The 3-D Ewald summation technique (EW3DC) is used to compute the electrostatic energies. The potential parameters are listed below in detail.

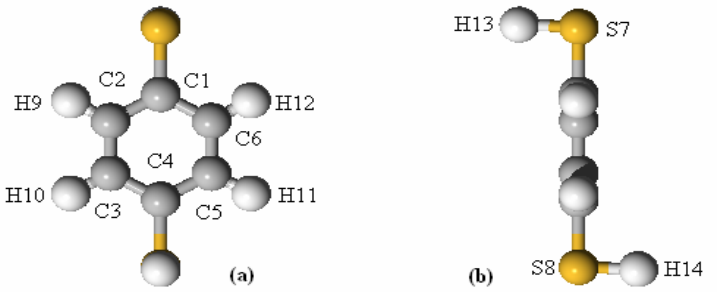

Figure 5.1. (a) The rigid bulk BDT molecular configuration used in the simulation. (b) Side view of (a).

5.2.1.1. Bulk BDT Potential Model

The BDT molecules in the bulk as shown in Figure 5.1 are modeled by an all-atom explicit potential based on the universal forcefield (UFF).[80] The potential for bulk BDT consists of two types of nonbonded interactions (nonbonded interactions occur between atoms in different molecules and between atoms in the same molecules that are more than three atoms apart in the molecule), the Lennard-Jones type dispersion energy and electrostatic energy. The Lennard-Jones energy between a pair of interacting sites *i* and *j* that are in different molecules is given by

$$U_{ij}^{LJ} = 4\varepsilon_{ij}\left[\left(\frac{\sigma_{ij}}{r_{ij}}\right)^{12} - \left(\frac{\sigma_{ij}}{r_{ij}}\right)^{6}\right] \tag{5-1}$$

The cross interaction potential parameters ε_{ij} and σ_{ij} are calculated from Lorentz-Berthelot combining rules if interacting sites *i* and *j* are different species as indicated in equation (5-2) and (5-3).

$$\varepsilon_{ij} = \sqrt{\varepsilon_i \varepsilon_j} \tag{5-2}$$

$$\sigma_{ij} = \frac{1}{2}\left(\sigma_i + \sigma_j\right) \tag{5-3}$$

The Lennard-Jones parameters in Eq. (5-1) for each interacting site on BDT are converted from corresponding UFF parameters, while the partial charges on each atom of a bulk BDT molecule are derived from recent quantum mechanical calculations.[45] The molecular configuration and potential parameters for the bulk BDT are summarized in Table 5.1.

Table 5.1. Molecular configuration and potential parameters for the bulk BDT model.

Bond lengths (Å)			
	C-C (benzene ring)	1.379	
	C-H	1.085	
	C-S	1.800	
	S-H	1.429	
Bond angles			
	C1-C2-C3	120°	
	C1-C2-H9	120°	
	C2-C1-S7	120°	
	C1-S7-H13	92.1°	
Lennard-Jones Parameters		ε(kcal/mol)	σ(Å)
	C	0.105	3.431
	H	0.044	2.571
	S	0.274	3.595
Partial charges		q(e)	
	C1, C4	-0.49	
	C2, C3, C5, C6	-0.06	
	S	0.06	
	H9, H10, H11, H12	0.20	
	H13, H14	0.15	

Table 5.2. Partial charges for potential of adsorbed BDT molecules.

Partial charges	q (e) (S8	q (e) (S7	q (e) (S8 & S7
C1	-0.49	-0.33	-0.34
C2,C6	-0.06	-0.10	-0.06
C4	-0.33	-0.49	-0.34
C3,C5	-0.10	-0.06	-0.06
S7	0.06	0.13	0.06
S8	0.13	0.06	0.06
H9, H10, H11,	0.20	0.20	0.20
H13	0.15	0.00	0.00
H14	0.00	0.15	0.00
Au	0.00	0.00	0.00

5.2.1.2. Au-BDT Potential Model

When a BDT molecule adsorbs on an Au nanowire, one or two of the sulfur atoms form chemical bonding with Au atoms, accompanied by the dissociation of the H atom from the originally bonded sulfur atom. The *ab initio* calculations indicate that the structure of the BDT is largely unchanged, but significant charge transfer occurs during the Au-S bonding process.[45] Therefore, for the partial charges calculation, we select the redistributed partial charges on the bonded BDT from the average of *ab initio* results of three DFT functional for the bridge bonding configuration.[45] Table 5.2 summarizes the partial charges for the bonded BDT model.

For the chemical bonding between the S atom in BDT and the bonded Au atoms in the nanowires, we chose the pairwise-additive Morse potential to describe the Au-S interaction. The Morse type potentials have been used previously to approximate the chemical adsorption of BDT on a Au surface.[89,90] Here, the Morse potential takes the form:

$$U_{Morse}^{Au-S} = D_e \exp[-\alpha(r-r_e)]\{\exp[-\alpha(r-r_e)]-2\}. \quad (5\text{-}4)$$

In Eq. (5-4), r is the distance between the center of S atom and the Au atom which bonds to this S atom; D_e, r_e, and α are empirical parameters. The Morse potential parameters have been further refined recently based on the calibrations for different BDT-nAu complexes.[91] It has been shown that the Au bridge site is the most stable adsorption site for S-Au chemical bonding.[92,93] Thus, we model the bonded interaction between the bonded S atom and the nearest two Au atoms by a strong Morse potential in the case of the nearest distance between this S atom and one of the bonded Au atoms is less or equal

to cutoff distance of 3 Å . The related parameters are listed in Table 5.3, which are the averages of those derived from three different DFT functionals for the BDT-3Au bridge bonding cluster.[91]

Table 5.3. Potential parameters for the Morse Au-S bonding.

D_e (kcal/mol)	r_e (Å)	α (1/Å)
28.7	2.44	1.67

5.2.2. Simulation Methodology

We study the equilibrium adsorption structure of BDT molecules on a gold nanowire that is completely immersed in BDT solution. GCMC method has been applied to acquire the equilibrium adsorption coverage of BDT on Au (001) nanowires. Canonical (*NVT* ensemble) Monte Carlo simulation runs are followed to further equilibrate the structures and to collect the bonding structures of the adsorbed phase from GCMC for analysis. A detailed description of GCMC (μVT ensemble) and canonical (*NVT*) MC simulation approach can be found elsewhere.[46] An appropriate μ value to make the BDT density approaches its bulk value is achieved by inserting BDT molecules to a simulation box with specific size. We find that in this dense liquid phase the bulk BDT density is quite independent on the BDT chemical potential μ set in the range of -120 to 120. Obviously, this is largely due to the predominant role of the total internal potential energy over the chemical potential μ for very dense liquids. In our study, μ is set at -5.

In this chapter, a small Au (001) nanowire (consisting of 256 gold atoms) and a relatively large Au (001) nanowire (consisting of 3254 gold atoms) are initially allowed to relax for at least 200 ps prior to GCMC insertion of BDT molecules. The initial molecular configuration of Au nanowire surrounded by 26 (small)/18 (large) nonbonded BDT molecules is shown in Figure 5.2. These BDT molecules are arranged in an FCC lattice in the specific simulation box. The nearest distance between the adsorbate molecules and the Au atom on the nanowire is greater than 2.5 r_e to avoid initial direct interactions between BDT and Au through chemical bonding potential. GCMC involves creation and deletion of BDT molecules for a given chemical potential, as well as

translation and rotation of rigid BDT molecules according to a set of given probabilities.[46] Because of the size and polarity of the BDT molecules, conventional GCMC simulations are very inefficient for inserting and deleting molecules. Therefore, we implement the orientationally biased GCMC[94] to improve the efficiency of the calculation. Each attempted insertion or deletion of a molecule utilized information from 15 random orientations.

Both GCMC and *NVT* MC simulations are carried out at 298 K. The simulation box lengths in three dimensions are 3.5 x 3.0 x 3.3 nm for small nanowire and 6.0 x 6.0 x 6.5 nm for larger nanowire, with periodic boundary conditions applied in all three directions. During the GCMC runs, BDT molecules are allowed to interact with the Au atoms through either Lennard-Jones or Morse potential, depending on the distance between the S atoms in BDT and the Au atoms on nanowire. If neither of the S atoms in a BDT molecule is within the Morse interaction distance (< 3.0 Å) to the Au atoms, the energy between each atom of the BDT and Au atoms is calculated by Lennard-Jones interaction. The electrostatic energy involving the BDT molecule is calculated from the partial charges for bulk BDTs. As soon as one of the S atoms of a BDT molecule is less than 3 Å, from the nearest Au atoms, the BDT molecules are identified as bonded molecules. The Morse potential is in effect between the S atom in the BDT and the two nearest Au atoms on the nanowire accompanied by the turning off the Lennard-Jones interaction between them. In the case of two S atoms in the same BDT molecules are both less than 3 Å to their nearest Au atoms, the two S atoms in BDT molecule are bonded to four nearest Au atoms through Morse potential. During a GCMC simulation, desorption process of BDT molecules form Au nanowire occurs with equal probability as

adsorption processed after the system reaches equilibrium. The energy calculation of a desorbing BDT molecule can be easily performed by reversing the above scheme.

After a prolonged GCMC run (over ten million moves), a densely packed BDT structure adsorbed on Au nanowire is obtained. The equilibrated absorbed configuration from GCMC was input as the starting point of NVT simulations. The further NVT equilibration typically included five million translation and rotation moves chosen randomly with equal probability. Additional five million NVT moves followed for collecting the structural data. The maximum values of translation and rotation of molecules were adjusted during the equilibration to achieve acceptance ratios for these moves of about 0.4. The cutoff of pairwise Lennard-Jones interaction between the interacting sites of BDT and Au atoms was 15 Å, without any long-range correction applied.

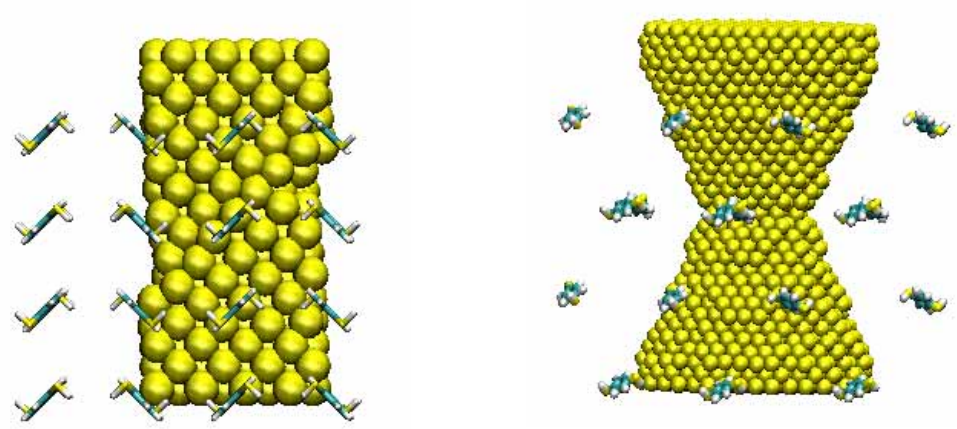

(a) (b)

Figure 5.2. Initial configurations. (a) 256-atom Au nanowire surrounded by 26 BDT molecules; (b) 3254-atom Au nanowire surrounded by 18 BDT molecules.

5.3. Adsorption Structure of Benzenedithiol on Gold Nanowires

Figure 5.3 and Figure 5.4 show the final adsorption configurations of BDTs on "small" and "large" gold nanowires. For the 256-atom small nanowire, the final adsorption structure is obtained after 10 million GCMC moves followed by equilibration of another 10 million *NVT* MC moves at 298 K. The total number of BDT molecules in the simulation box is 142, corresponding to a density of 0.99 g/cm^3, which is slightly lower than the BDT bulk value at 298 K (1.2 g/cm^3). The total number of chemically bonded BDT molecules on Au nanowire is 80. For the 3254-atom larger nanowire, the final adsorption structure is obtained after 30 million GCMC moves followed by equilibration of another 10 million *NVT* MC moves at 298 K. The total number of BDT molecules in the simulation box is 824, corresponding to a density of 1.04 g/cm^3. In this case, the total number of chemically bonded BDT molecules on Au nanowire is 314. In Figure 5.5, the distribution of bonded BDTs and sulfurs on Au nanowire is clearly demonstrated.

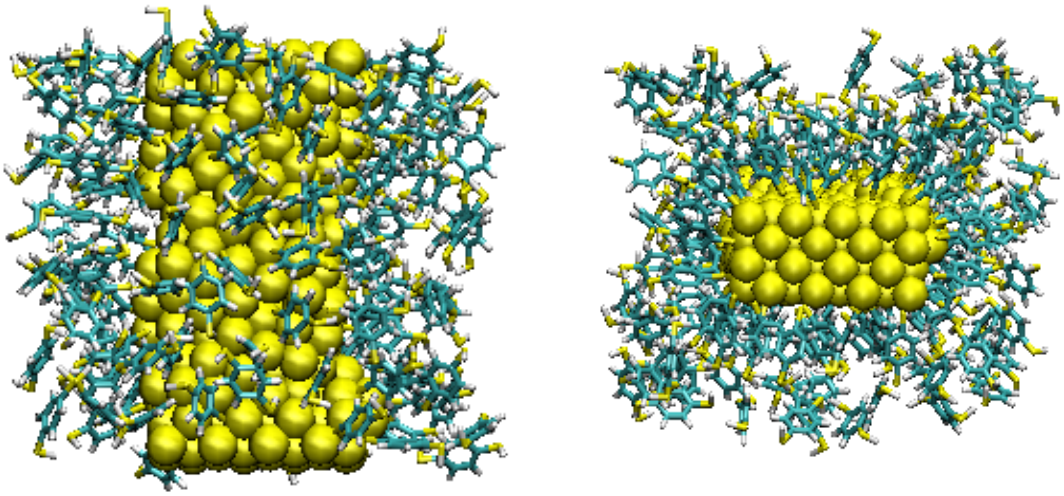

(a) (b)

Figure 5.3. Final adsorption configurations of BDTs on 256-atom Au (001) nanowire. The dimension of the box is 3.5 x 3 x 3.3 nm^3. (a) side view; (b) top view.

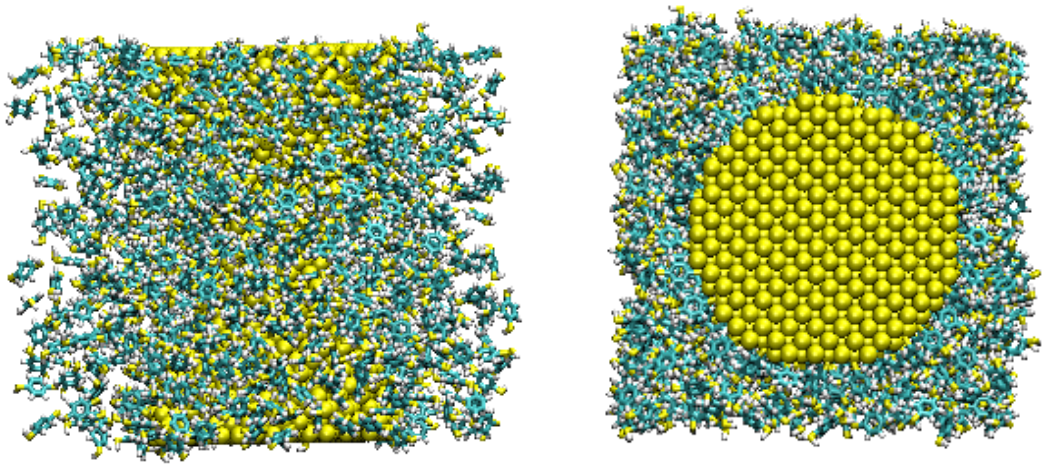

(a) (b)

Figure 5.4. Final adsorption configurations of BDTs on 3254-atom Au (001) nanowire. The dimension of the box is 6 x 6 x 6.5 nm^3. (a) side view; (b) top view.

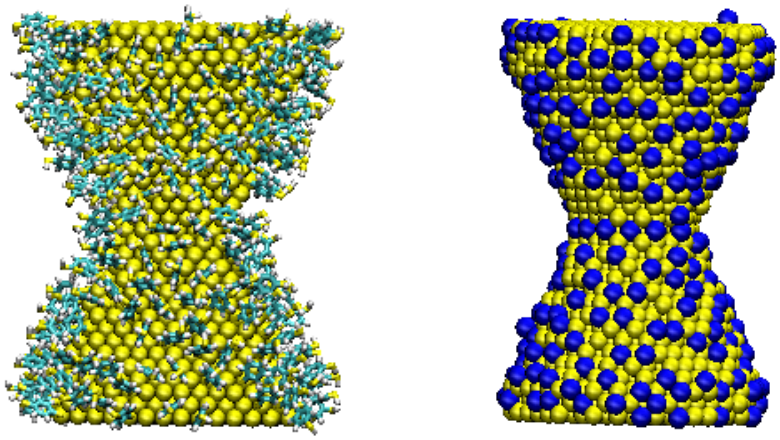

(a) (b)

Figure 5.5. The adsorption configurations after removing non-bonded BDT molecules. (a) the bonded BDTs on Au nanowire; (b) the bonded sulfur (cyan) on the Au nanowires.

To investigate the local bonding geometries, we plot S-Au and S-S distance distributions in Figures 5.6 and 5.7 respectively for the 3254-atom nanowire. Figure 5.6 clearly shows the first S-Au distance distribution peak occurs at 2.5 Å, which corresponds to the S-Au on-bridge bonding. The second S-Au peak at 3.2 Å corresponds to the nonbonded gold atoms, which are second nearest to the S atom. Closer examination reveals that these nonbonded gold atoms corresponding to the second peak are all surface atoms. Interestingly, Figure 5.7 shows that the first S-S peak occurs at about 4.2 Å. This S-S distance is less than the 5.0 Å, the distance between sulfur head groups commonly observed for benzenethiol (BD)[95] or other alkanethiol molecules[96-98] adsorbed on Au (111) surface. This is most likely due to the curved surface of gold nanowire which favors the formation of more condensed BDT packing structure.

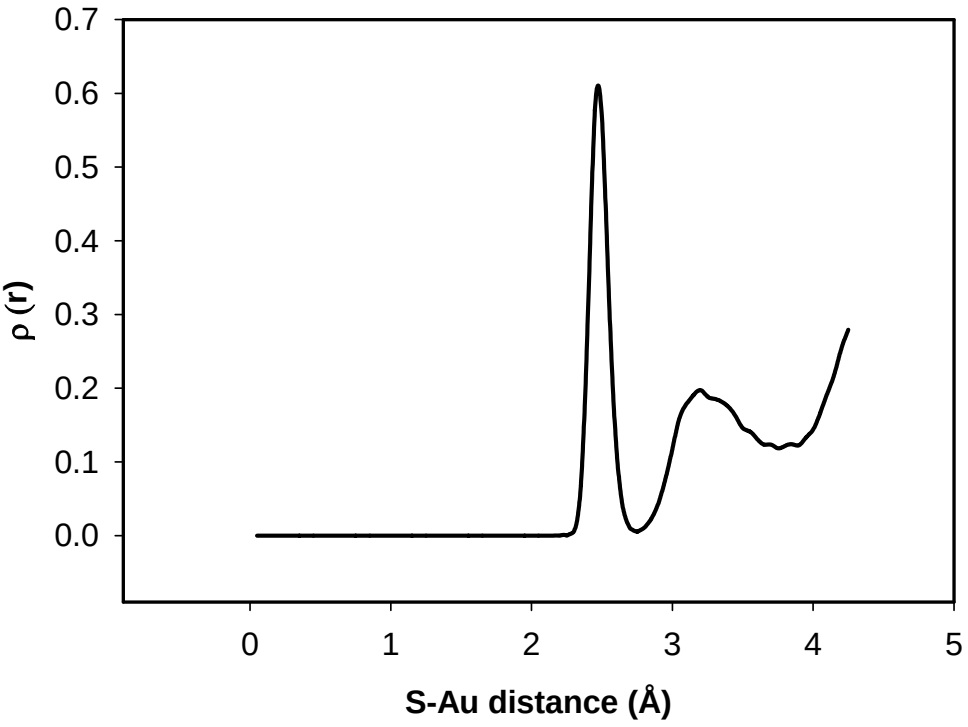

Figure 5.6. The histogram of the bonded sulfur and all of the Au atoms in the nanowire.

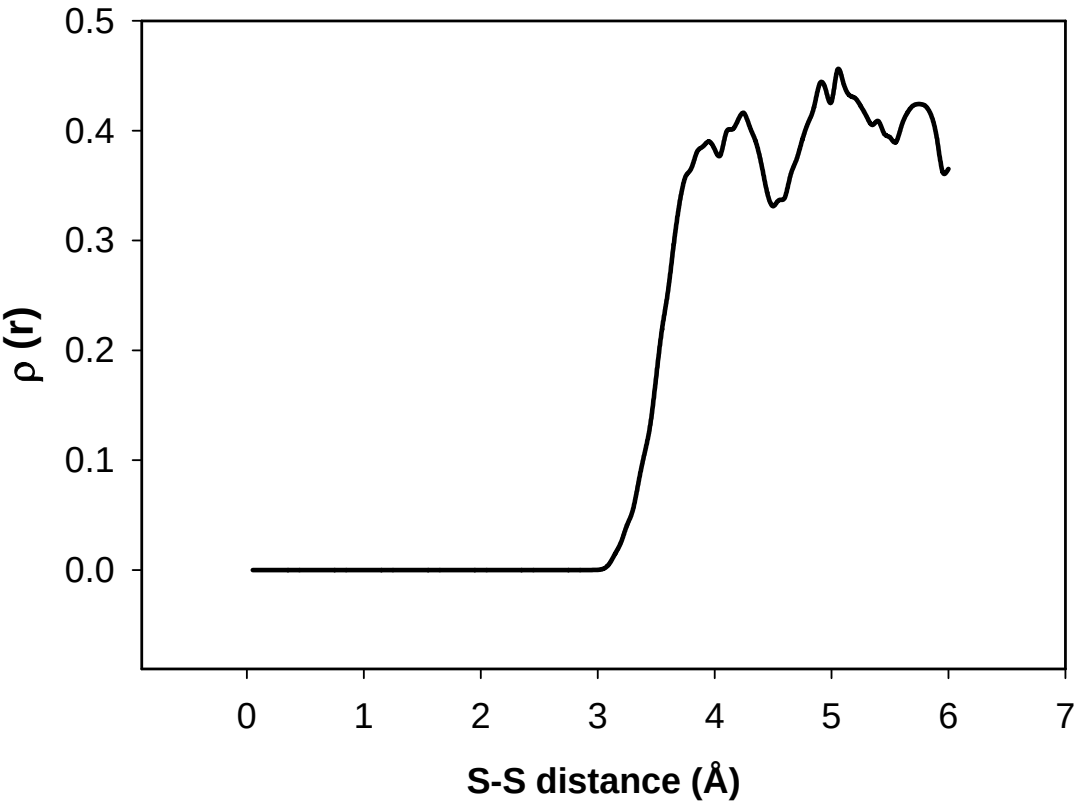

Figure 5.7. The histogram of the bonded sulfurs in the nanowire.

The local bonding structure shown in Figure 5.6 and 5.7 include all the bonded Au atoms, whether the Au atoms are on surface or in the bulk of the nanowire. In order to investigate to what extent the sulfur atoms are bonded on surface Au atoms, we use a special technique to identify the surface Au atoms. Initially, a set of ghost atoms surround the nanowires, then the ghost atoms approach the nanowires little by little until the potential between the ghost atom and Au atom approaches zero. The atomic interaction between the ghost Au atom and Au atoms is represented by a simple LJ pair potential from the Universal Forcefield (UFF)[80] as:

$$E_{ghost-Au} = 4\varepsilon_{ghost-Au}\left[\left(\frac{\sigma_{ghost-Au}}{r}\right)^{12} - \left(\frac{\sigma_{ghost-Au}}{r}\right)^{6}\right] \quad (5\text{-}5)$$

The whole process of finding the surface atoms is shown in Figure 5.8. For the 3254-atom Au nanowire, the number of surface Au atoms equal to 966. In another words, the surface atoms occupy about 30% of all the Au atoms. Therefore, it is valuable to construct the local bonding structure of the S-Au distance distribution which includes only the surface Au atoms as shown using the dashed line in Figure 5.9. The solid line in Figure 5.9 represents the S-Au distance distribution which includes all of the Au atoms as before for comparison. It is clear that the peaks occur almost at the same positions under these two conditions, indicating the majority of the bonded BDT molecules are bonded on the 966 surface Au atoms.

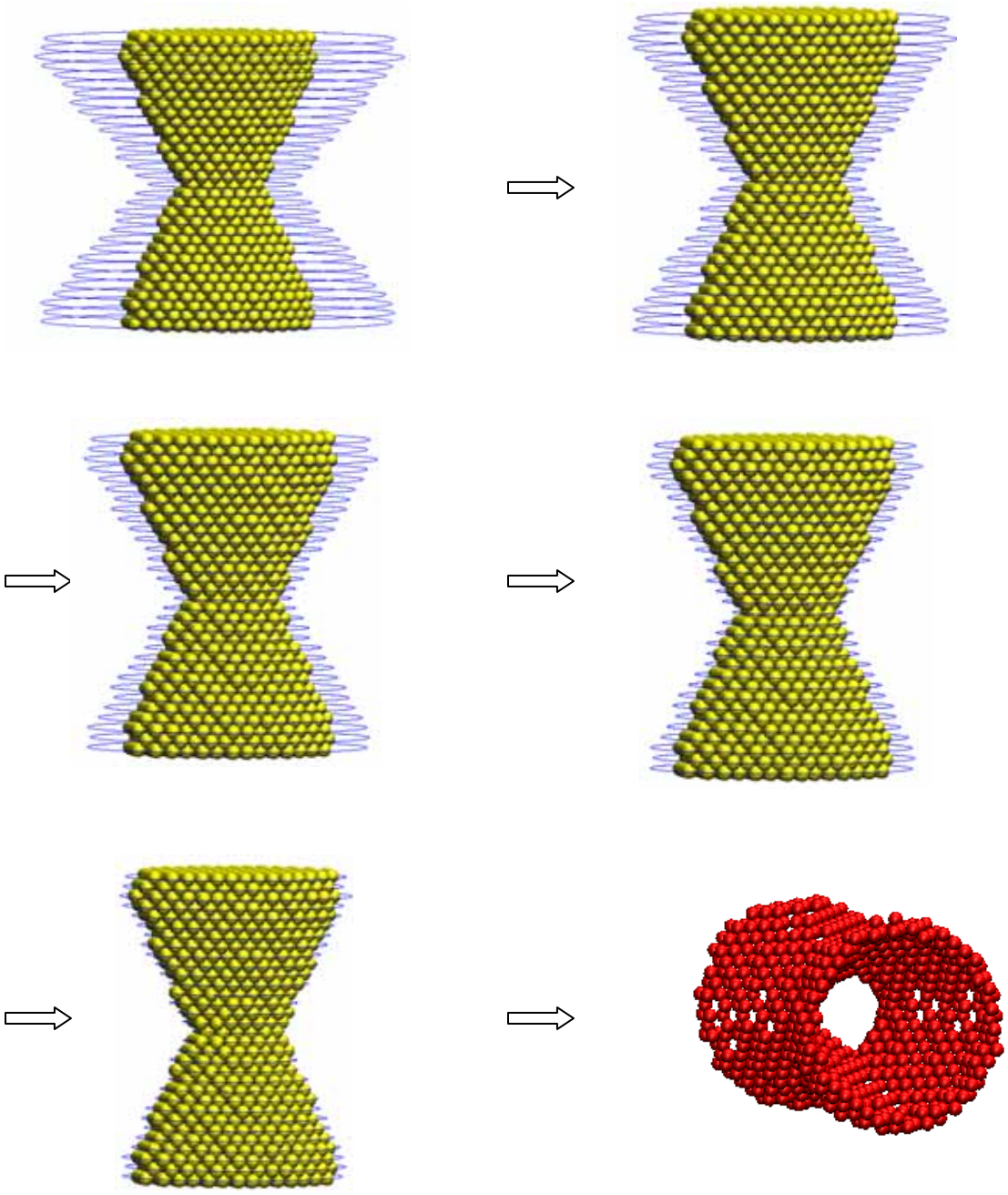

Figure 5.8. The process of identifying surface Au atoms (in red color).

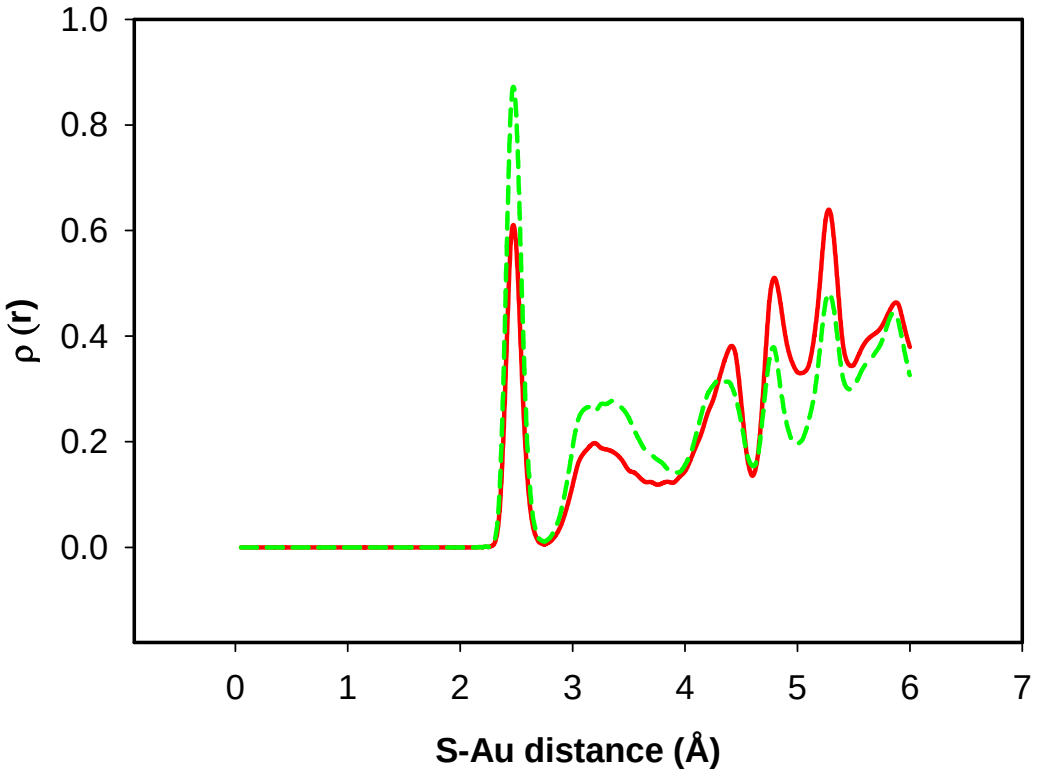

Figure 5.9. The histogram of the bonded sulfur and Au atoms in the nanowire (dashed line: surface Au atoms only; solid line: all Au atoms).

Another interesting phenomenon observed is that more than one BDT molecules are bonded to Au-Au pairs (through bridge sites) with an Au atom in common. This is especially obvious for the 256-atom Au nanowire. Table 5.4 shows the probability of the shared Au atoms being bonded by single or multiple BDT molecules. Two BDT molecules share the same bonded Au atom is the most popular event. For the small wire, one Au atom can be shared at most by four BDT molecules. In contrast, there are at most two BDT molecules share the same Au atom for larger wire. In addition, the probability of sharing the same Au atom decreases from 21.1% for small wire to 9.5% for large wire. In Figure 5.10a we show a typical configuration of BDT molecules sharing the same bonded Au atom with the bonded S-Au distance around 2.6 Å. Figure 5.10b shows that the shared Au atom locates in the corner of the Au small nanowire. The curvature structure of the small nanowire and the high chance for Au atoms to be on the corner are the main reasons for Au atoms to be shared by more than one BDT molecules.

Table 5.4. The probability of Au atom shared by more than one BDT molecules.

	256-atom-wire	3254-atom-wire
Au bonded by one BDT molecule	78.9%	90.5%
Au bonded by two BDT molecules	18.0%	9.5%
Au bonded by three BDT molecules	2.3%	0.0%
Au bonded by four BDT molecules	0.8%	0.0%

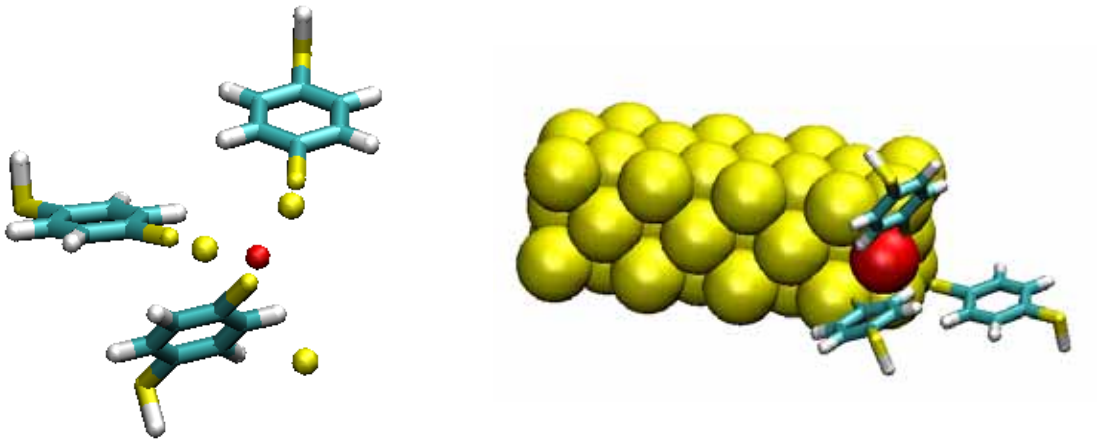

(a) (b)

Figure 5.10. A schematic of four BDT molecules bonded to Au pairs. (a) one of the Au atoms (in red) shared by all three BDT molecules; (b) the shared Au atom locates on the corner of the nanowire.

5.4. Conclusions

In this chapter we relate molecular simulations of the self-assembly of BDT molecules on Au nanowires. The forcefield parameters developed recently for the BDT-Au chemical bonding have been implemented in GCMC simulations. We have successfully obtained the adsorption configurations of BDT molecules on both small Au (001) nanowire and larger Au (001) nanowire with the BDT density in the simulation box approaches to the bulk density. The local bonding geometry of BDT-Au obtained is consistent with previous results that S binds most favorably on the bridge sites of the Au surface with the distance of bonded S and Au located around 2.5 Å. We find that the packing density of bonded BDT on the surface of Au nanowire is larger than that of BT molecules on Au (111) surface, evidently due to the curved surface of the gold wire. Furthermore, an Au atom can be bonded by multiple BDT molecules and this phenomenon is more apparent for the smaller, higher curvature nanowire.

CHAPTER VI

DYNAMIC ELONGATION OF NANOWIRES IN BENZENEDITHIOL

6.1. Introduction

The understanding of molecule-metal contact effects on electron transport through molecular junctions is an important step toward building a functional device based on single molecules. The transport property of the combined Au-BDT-Au electrode system has been intensively investigated because BDT is a typical and simple π-conjugated molecule.[99] Several theoretical studies have produced the qualitative feature of the measured current-voltage characteristics for BDT molecule sandwiched between two gold electrodes. However, a significant discrepancy in *I-V* values between these quantum calculations and experimental measurements persists. It has been shown that the absolute magnitude of the current is an extremely sensitive function of the contact geometry and chemistry in the metal-molecule interface. In addition, temperature (hot electrons and vibrational coupling) or local disorder in the Au metal near the contacts arising from the breaking of the gold wire can alter the value of the current.[21] The microscopic contact geometry at the BDT-Au interface is one of the critical factors that have dramatic influence on the conductance. For example, the conductance is dependent on whether the molecule is properly bonded to both electrodes, what the binding site of the thiol group on the gold electrode is, and how the molecule orients itself with respect to the gold electrode.[88] The DFT calculations by Ponte *et al.*[100] show three possible low energy Au-BDT-Au configurations. Two BDT molecules can each bond to one side of the metal and

transfer electrons through the overlap of electronic clouds. The stable thiol group binding sites are either on bridge or on hollow. Moreover, the BDT molecules can be laid almost flat on the surface or they can be almost perpendicular to the metal surface. However, for these three stable interface structures, the conductances are $0.04G_0$, $0.64G_0$ and $0.51G_0$, respectively, where $G_0 = 2e^2/h$ represents the fundamental conductance value. The difference in conductance caused by variation in contact geometry is thus as large as one order of magnitude. Another DFT calculation done by Nara *et al.*[93] shows the conductance varying from 0.004 G_0 to 0.04 G_0 to 0.078 G_0 simply by altering the thiol group binding sites from on top, on bridge to on hollow sites, respectively. On the experimental side, applying mechanically controllable break junction technique, Tsutsui *et al.*[101] detected low (~ 0.01 G_0) and high conductance (~ 0.1 G_0) regimes for BDT molecules bonded on Au wires. They attributed the two distinct conductance states to the Au-S bonding configurations changing from top-top to top-hollow (or the hollow-hollow) sites. This tenfold (0.1 G_0 / 0.01 G_0) increase in the BDT conductance is consistence with Nara *et al.*'[93] theoretical calculation (0.04 G_0 / 0.004 G_0) when the bridging configurations transformed from top-top to hollow-hollow sites. Similarly, using STM-break junction setup for single alkanedithiols, Li *et al.*[102] also recorded the occurrence of low and high conductance regimes. Therefore, it is valuable to seek insights into the local bonding structures of BDTs on Au nanowires via classical molecular simulations to identify the detailed Au-BDT-Au configurations since in quantum mechanical *I-V* calculations, the geometry of the stable metal-molecule-metal interface has to be determined at the initial setup. DFT calculations are typically done on optimized geometries at 0 *K*, which are clearly subject to, possible change at ambient conditions in a

complex environment. Our simulation results can be used as an accurate input to quantum calculations that will help to resolve the original discrepancy between experimental and theoretical studies. Additionally, classical molecular modeling also helps to interpret, and to give useful feedback to, the experimental measurements, device design, and manufacture.

6.2. Simulation Details

6.2.1. Forcefields

6.2.1.1. Universal Forcefield[80] for the BDT Organic Molecules

For the simulation of the elongation and breakage of gold nanowire in organic solvents, the BDTs are modeled as nonrigid molecule. The potential energy is expressed as a sum of valence or bonded interactions and nonbonded interactions:

$$E = E_R + E_\theta + E_\phi + E_\omega + E_{vdw} + E_{el} \tag{6-1}$$

The bonded interactions consist of bond stretching (E_R), bond angle bending (E_θ), dihedral angle torsion (E_ϕ), and inversion (E_ω). The nonbonded interactions consist of van der Waals (E_{vdw}) and electrostatic (E_{el}) terms.

For two atomic species I and J bonded together, the harmonic potential is used to describe the bond vibration (bond stretching):

$$E_R = \frac{1}{2} k_{IJ} \left(r - r_{IJ} \right)^2 \tag{6-2}$$

where r_{IJ} is the equilibrium bond length and k_{IJ} is the bond stretching force constant.

For two atoms *I* and *K* bonded to atom J in a general nonlinear case, the bond angle bending energy will take the form (bond angle bending):

$$E_\theta = \frac{k_{IJK}}{2\sin^2\theta_0}(\cos\theta - \cos\theta_0)^2 \tag{6-3}$$

where θ_0 is the equilibrium angle and k_{IJK} is the angle bending force constant.

For two bonds IJ and KL connected to a central bond *JK*, the torsion energy E_θ is given by (dihedral angle torsion):

$$E_\phi = \frac{1}{2}V_\phi[1 - \cos n\phi_0 \cos n\phi] \tag{6-4}$$

where V_ϕ is the rotational barrier, *n* is the periodicity of the potential and ϕ_0 is the equilibrium angle.

When atom *I* is bonded exactly to three other atom *J*, *K*, and *L*, the inversion energy is (torsion):

$$E_\omega = k_{IJKL}(1 - \cos\omega_{IJKL}) \tag{6-5}$$

where k_{IJKL} is the force constant and ω_{IJKL} is the angle between *IL* axis and *IJK* plane.

Table 6.1 lists all of the force constants and equilibrium values.

Table 6.1. Potential parameters in UFF.

bond stretching	r_{ij} (Å)	k_{IJ} (kcal/mol·Å^2)
C-C	1.379	925.83
C-R	1.085	708.61
C-S	1.800	588.45
S-H	1.429	438.3
angle bending	θ_0 (^{o})	k_{IJK} (kcal/mol· rad^2)
C-C-C	120	222.72
C-C-H	120	114.23
C-C-S	120	201.01
C-S-H	92.1	102.16
torsion	ϕ_0 (^{o})	$\frac{1}{2}V_\phi$ (kcal/mol)
X-C-C-X	180 (0)	13.474
X-C-S-X	90	3.9528
inversion	ω_0 (^{o})	k_{IJKL} (kcal/mol)
	0	6

For atoms in the same BDT molecule but separated by more than two neighboring atoms (the 1-2 and 1-3 interaction exclusions) or for atoms in different BDT molecules and all of the nonbonded Au atoms, the van der Waals interactions are included in the forcefield. A Lennard- Jones 12-6 –type expression is used:

$$E_{vdw} = D_{IJ}\left[\left(\frac{x_{IJ}}{r}\right)^{12} - 2\left(\frac{x_{IJ}}{r}\right)^{6}\right] \tag{6-6}$$

D_{IJ} is the well depth in kcal/mol and x_{IJ} is the van der Waals bond length in Å corresponding to the point of minimum energy. For different atomic species interactions, the general x_{IJ} and D_{IJ} parameters are obtained from the homonuclear parameters using the geometric mean combination rule. Table 6.2 summarizes all of the LJ 12-6 potential parameters for C, H, S, and Au species.

The partial charges from Mulliken population analysis in *ab initio* calculations[23] are assigned to individual atoms in BDT molecules.

Table 6.2. Atomic Mass and Lennard-Jones 12-6-type parameters in UFF.

atom type	Mass (amu)	D_{IJ} (kcal/mol)	x_{IJ} (Å)
C	12.0000	0.1050	3.851
H	1.0000	0.044	2.886
S	32.0000	0.274	4.035
Au	197.0000	0.039	3.293

6.2.1.2. Au-BDT Bonding Potential

For the chemical bonding between the S atom in BDT and the bonded Au atoms in the nanowires, we applied the pairwise-additive Morse potential to describe the Au-S interaction as described in chapter V, section 5.2.1.2. Due to the strong Morse potential, we exclude the bond stretching, bond angle bending and bond torsion between the bonded sulfur atom and other particles in this specific BDT molecule where the bonded sulfur belongs to.

6.2.2. Simulation Methodology

We performed MD simulations for the elongation of an Au nanowire along the [001] direction in BDT solution at room temperature. The final equilibrium adsorption structures from GCMC (Figure 5.3 and Figure 5.4) are used as the starting configurations for the MD elongation process. This is because elongation of nanowire has been done through mechanical controllable break junction experiment in BDT solutions in Reed *et al.* experiment. Elongation of nanowire is realized by moving the top rigid layers along the *z* direction in increments of 0.1 Å, followed by 1000 time steps relaxations, with a time step of 2 fs. This corresponds to an elongation rate of 5.0 m/s. Periodic boundary conditions (PBC) are applied in three dimensions. The simulation box lengths in z direction increased along with the elongation process. Due to the high stiffness of the benzene ring and strong valence bonding of the BDT molecules, a much smaller time step is needed for the fast variation with large magnitude of intramolecular forces than for the slow variations of intermolecular forces. Moreover, within the intramolecular forces, the H atoms are 1 order of magnitude lower in mass than other particles which causes

them to have much higher vibration frequencies than others. Therefore, a multiple-time-scale method is appropriate to integrate the equations of motion. In our study, we applied the double reversible reference system propagator algorithm (RESPA) based on the original work of Tuckerman *et al*.[68] and the extended system Nosé-Hoover dynamics[67,103] for the NVT ensemble. The conserved quantity (pseudo-Hamiltonian) of the system is:

$$H'(x, y, p_x, p_y, \eta, p_\eta) = \sum \frac{p_x^2}{2m} + \sum \frac{p_y^2}{2m} + V + \frac{p_\eta^2}{2Q} + 3NkT\eta = V + V_{Nose} + V_{kin} \qquad (6\text{-}7)$$

where x and y are the positions of the BDT particles and Au atoms, respectively, p_x and p_y are the momenta of the BDT particles and Au atoms, respectively, η and p_η are the extended thermostat and conjugated momentum., k is the Boltzmann constant, and T is the temperature. In equation 6-7, variable V is the potential energy of the molecular system. Tuckerman *et al*.[68] showed that any integrators derived from Trotter factorization of the Liouville operator iL are reversible. They then constructed a general double-RESPA scheme for the systems with short-long-range force separations and disparate mass problems. Here we extended their double-RESPA scheme in order to fit our Au-BDT interaction system, which involves a further decomposition of the propagator for the particle H within the reference system and separation the positions and momenta between BDT particles and Au atoms. The numerical procedure for the proposed double RESPA is in detail as follows:

The Liouville operator corresponds to the pseudo-Hamiltonian (equation 6-7) is given by:

$$iL = iL_r + \left[F_l(x,y)\frac{\partial}{\partial p_x} - \dot{\eta} p_x \frac{\partial}{\partial p_x} \right] + \left[F_y \frac{\partial}{\partial p_y} - \dot{\eta} p_y \frac{\partial}{\partial p_y} \right] + \dot{\eta}\frac{\partial}{\partial \eta} + F_\eta(p)\frac{\partial}{\partial p_\eta} \qquad (6\text{-}8)$$
$$= iL_r + iL_1$$

where iL_r is the reference system operator and iL_1 is the remaining operator. iL_r is defined as:

$$iL_r = \dot{x}\frac{\partial}{\partial x} + F_s(x)\frac{\partial}{\partial x} \qquad (6\text{-}9)$$

where $F_s(x)$ is the short-range intramolecular interactions between BDT molecules. Supposed that $\Gamma(0) = \Gamma(x(0), y(0), p_x(0), p_y(0), \eta(0), p_\eta(0))$ is the initial state of the molecular system. The state of the system at time t is given by:

$$\Gamma(t) = e^{iL_t}\Gamma(0) \qquad (6\text{-}10)$$

For a small time step Δt, the propagator $e^{iL\Delta t}$ can be factored using the Trotter theorem as:

$$e^{iL\Delta t} = e^{iL_1\Delta t/2} e^{iL_r\Delta t} e^{iL_1\Delta t/2} \qquad (6\text{-}11)$$

The middle propagator in equation 6-11 involves the calculation of short-range forces that have fast varying characteristics with large magnitudes. This will need a smaller time step $\delta t = \Delta t / n$ to integrate the equations of motion in the reference system for n times. Because of the large difference in mass between H atoms and C, S atoms, in order to avoid the drift in total energy, we decompose the propagator for light particles within the reference system as:

$$iL_r = iL_{lr} + iL_{hr} \tag{6-12}$$

$$iL_{lr} = \dot{l}\frac{\partial}{\partial l}F_{ls}(l,h)\frac{\partial}{\partial p_l} \tag{6-13}$$

$$iL_{hr} = \dot{h}\frac{\partial}{\partial h}F_{hs}(l,h)\frac{\partial}{\partial p_h} \tag{6-14}$$

where l and h label fast and slow degrees of freedom. So the middle propagator can be written as:

$$e^{il_r\Delta t} = \left[e^{iL_{lr}(\delta t/2)}e^{iL_h\delta t}e^{iL_{lr}(\delta t/2)}\right]^n \qquad (\Delta t = n\delta t) \tag{6-15}$$

In the above equation, a second decomposition is employed in the propagator $e^{iL_{lr}(\delta t/2)}$, yielding:

$$e^{iL_{lr}(\delta t/2)}e^{iL_{hr}\delta t}e^{iL_{lr}(\delta t/2)} = \left[e^{iL_{lr}(dt)}\right]^{m/2}e^{iL_{hr}\delta t}\left[e^{iL_{lr}(dt)}\right]^{m/2} \qquad (\delta t = mdt) \tag{6-16}$$

Where

$$e^{iL_{lr}(dt)} = e^{(dt/2)F_{ls}(l,h)\partial/\partial p_l}e^{dt\dot{l}\partial/\partial l}e^{(dt/2)F_{ls}(l,h)\partial/\partial p_l} \tag{6-17}$$

$$e^{iL_{hr}\delta t} = e^{(\delta t/2)F_{hs}\partial/\partial p_h}e^{\delta t\dot{h}\partial/\partial h}e^{(\delta t/2)F_{hs}\partial/\partial p_h} \tag{6-18}$$

The total gain of this double-RESPA scheme is mn.

The first and third propagators $e^{iL_1\Delta t/2}$ in equation 6-11 can be further decomposed to:

$$e^{iL_1\Delta t/2} = e^{iL_x\Delta t/4} e^{iL_y\Delta t/2} e^{iL_x\Delta t/4} \tag{6-19}$$

Consider the initial state of the molecular system $\Gamma(0) = \{x_l(0), x_h(0), y(0), p_{xl}(0), p_{xh}(0), p_y(0), \eta(0), p_\eta(0)\}$ and the new state $\Gamma(\Delta t) = \{x_l(\Delta t), x_h(\Delta t), y(\Delta t), p_{xl}(\Delta t), p_{xh}(\Delta t), p_y(\Delta t), \eta(\Delta t), p_\eta(\Delta t)\}$ at time Δt, where x_l, x_h are the coordinates of the light and heavy particles in BDT, y is the coordinate of Au atom, p_{xl}, p_{xh} and p_y are the corresponding conjugated momenta, and η and p_η are the thermostat coordinate and momentum. The third propagator $e^{iL_x\Delta t/4}$ in equation 6-19 propagates the phase variables to:

$$x_l(0) \to x_{l0} = x_l(0) \tag{6-20}$$

$$x_h(0) \to x_{h0} = x_h(0) \tag{6-21}$$

$$p_{xl}(0) \to p_{xl0} = \left[p_{xl}(0) + \frac{\Delta t}{8} F_l(0) \right] e^{-(\Delta t/4)(p_{\eta 0}/Q)} + \frac{\Delta t}{8} F_l(0) \tag{6-22}$$

$$p_{xh}(0) \to p_{xh0} = \left[p_{xh}(0) + \frac{\Delta t}{8} F_l(0) \right] e^{-(\Delta t/4)(p_{\eta 0}/Q)} + \frac{\Delta t}{8} F_l(0) \tag{6-23}$$

$$\eta(0) \to \eta_0 = \eta(0) + \frac{\Delta t}{2} \frac{p_{\eta 0}}{Q} \tag{6-24}$$

$$p_\eta(0) \to p_{\eta 0} = p_\eta(0) + \frac{\Delta t}{2} F_\eta(0) \tag{6-25}$$

where $F_l(0) = F_l(x_l(0), x_h(0))$ is the initial long-range force and $F_\eta(0) = \sum p^2(0)/m - 3NkT$ is the initial thermostat force. The middle propagator $e^{iL_y\Delta t/2}$ in equation 6-19 propagates the coordinates and momenta of Au atoms and generates a velocity Verlet algorithm.

$$y_0 \to y_0 + \frac{\Delta t}{2}\frac{p_{y0}}{m}e^{-(\Delta t/4)(p_{\eta 0}/Q)} + \frac{1}{2}\left(\frac{\Delta t}{2}\right)^2 \frac{F_y(0)}{m} \tag{6-26}$$

$$p_{y0} \to \left\{ p_{y0}e^{-(\Delta t/4)(p_{\eta 0}/Q)} + \frac{\Delta t}{4}\left[F_y(0) + F_y\left(\frac{\Delta t}{2}\right)\right]\right\} e^{-(\Delta t/4)(p_{\eta 0}/Q)} \tag{6-27}$$

Followed by the propagating of the first propagator in equation 6-19 as:

$$p_{xl}\left(\frac{\Delta t}{4}\right) \to p_{xl\Delta t/4} = \left[p_{xl}(0) + \frac{\Delta t}{8}F_l\left(\frac{\Delta t}{2}\right)\right] e^{-(\Delta t/4)(p_{\eta 0}/Q)} + \frac{\Delta t}{8}F_l\left(\frac{\Delta t}{2}\right) \tag{6-28}$$

$$p_{xh}\left(\frac{\Delta t}{4}\right) \to p_{xh\Delta t/4} = \left[p_{xh}(0) + \frac{\Delta t}{8}F_l\left(\frac{\Delta t}{2}\right)\right] e^{-(\Delta t/4)(p_{\eta 0}/Q)} + \frac{\Delta t}{8}F_l\left(\frac{\Delta t}{2}\right) \tag{6-29}$$

The middle propagator in equation 6-11 can be further decomposed according to equation 6-12 ~ 6-18, which propagator only the coordinates and monmenta of all of the BDT particles in the reference system:

$$\left.\begin{aligned} x_{l0} &\to x_{l0} + dt\left(\frac{p_{xl}(\Delta t/4)}{m}\right) + \frac{1}{2}(dt)^2\frac{F_{ls}(l_0,h_0)}{m} \\ p_{xl}\left(\frac{\Delta t}{2}\right) &\to p_{xl\Delta t/2} = \left[p_{xl}\left(\frac{\Delta t}{4}\right) + \frac{\Delta t}{8}F_{ls}\left(\frac{\Delta t}{4}\right)\right] e^{-(\Delta t/4)(p_{\eta 0}/Q)} + \frac{\Delta t}{8}F_{ls}\left(\frac{\Delta t}{2}\right) \end{aligned}\right\}$$

integrate *m/2* time step *dt* (6-30)

$$\left.\begin{aligned} x_{h0} &\to x_{h0} + \delta t\left(\frac{p_{xh}(\Delta t/4)}{m}\right) + \frac{1}{2}(\delta t)^2\frac{F_{lh}(l_0,h_0)}{m} \\ p_{xh}\left(\frac{\Delta t}{2}\right) &\to p_{xh\Delta t/2} = p_{xh}\left(\frac{\Delta t}{4}\right) + \frac{\delta t}{2}\left[F_l\left(\frac{\Delta t}{4}\right) + F_l\left(\frac{\Delta t}{2}\right)\right] \end{aligned}\right\}$$

integrate one time step δt (6-31)

$$\left.\begin{aligned} x_{l\Delta t/2} &\to x_{l0} + dt\left(\frac{p_{xl}(\Delta t/2)}{m}\right) + \frac{1}{2}(dt)^2\,\frac{F_{ls}(l_0,h_0)}{m} \\ p_{xl}\left(\frac{\Delta t}{2}\right) &\to p_{xl\Delta t/2} = \left[p_{xl}\left(\frac{\Delta t}{4}\right) + \frac{\Delta t}{8}F_{ls}\left(\frac{\Delta t}{4}\right)\right]e^{-(\Delta t/4)(p_{\eta 0}/Q)} + \frac{\Delta t}{8}F_{ls}\left(\frac{\Delta t}{2}\right) \end{aligned}\right\}$$

integrate *m/2* time step *dt* (6-32)

where $\delta t = m(dt)$. Then repeat the integration processes 6-30 ~ 6-32 *n* times to Δt.

Now the coordinates of all of the light and heavy particles in BDT have been propagated to $\{x_l(\Delta t), x_h(\Delta t)\}$, but their momenta $\{p_{xl}, p_{xh}\}$ and coordinates and momenta of Au atoms need to be propagated by the long-range forces from the current state to the final stage.

$$p_{xl}\left(\frac{3\Delta t}{4}\right) \to p_{xl3\Delta t/4} = \left[p_{xl}\left(\frac{\Delta t}{2}\right) + \frac{\Delta t}{8}F_l(\Delta t)\right]e^{-(\Delta t/4)(p_{\eta 0}/Q)} + \frac{\Delta t}{8}F_l(\Delta t) \tag{6-33}$$

$$p_{xh}\left(\frac{3\Delta t}{4}\right) \to p_{xh3\Delta t/4} = \left[p_{xl}\left(\frac{\Delta t}{2}\right) + \frac{\Delta t}{8}F_l(\Delta t)\right]e^{-(\Delta t/4)(p_{\eta 0}/Q)} + \frac{\Delta t}{8}F_l(\Delta t) \tag{6-34}$$

$$y_{\Delta t} \to y_{\Delta t/2} + \frac{\Delta t}{2}\frac{p_{y\Delta t/2}}{m}e^{-(\Delta t/4)(p_{\eta 0}/Q)} + \frac{1}{2}\left(\frac{\Delta t}{2}\right)^2\frac{F_y(\Delta t)}{m} \tag{6-35}$$

$$p_{y0} \to \left\{p_{y0}e^{-(\Delta t/4)(p_{\eta 0}/Q)} + \frac{\Delta t}{4}\left[F_y\left(\frac{\Delta t}{2}\right) + F_y(\Delta t)\right]\right\}e^{-(\Delta t/4)(p_{\eta 0}/Q)} \tag{6-36}$$

$$p_{xl}(\Delta t) \to p_{xl\Delta t} = \left[p_{xl}\left(\frac{3\Delta t}{4}\right) + \frac{\Delta t}{8}F_l(\Delta t)\right]e^{-(\Delta t/4)(p_{\eta 0}/Q)} + \frac{\Delta t}{8}F_l(\Delta t) \tag{6-37}$$

$$p_{xh}(\Delta t) \rightarrow p_{xh\Delta t} = \left[p_{xh}\left(\frac{3\Delta t}{4}\right) + \frac{\Delta t}{8} F_l(\Delta t) \right] e^{-(\Delta t/4)(p_{\eta 0}/Q)} + \frac{\Delta t}{8} F_l(\Delta t) \tag{6-38}$$

The thermostat coordinate η and p_η are finally propagated to:

$$\eta(\Delta t) = \eta_0 + \frac{\Delta t}{2}\frac{p_{\eta 0}}{Q} = \eta(0) + \frac{\Delta t p_\eta(0)}{Q} + \frac{\Delta t^2}{2Q} F_\eta(0) \tag{6-39}$$

$$p_\eta(\Delta t) = p_{\eta 0} + \frac{\Delta t}{2} F_\eta(\Delta t) = p_\eta(0) + \frac{\Delta t}{2}\left[F_\eta(0) + F_\eta(\Delta t)\right] \tag{6-40}$$

6.3. Results

6.3.1. Equilibration

In order to check the validity of our deduced double-RESPA scheme, we plot the variations in the energy terms in equation 6-7 during the first 20 *ps* relaxation of BDT molecules on both 256-atom-Au (001) nanowire and 3254-atom-Au (001) nanowire at room temperature in Figure 6.1 and Figure 6.2, respectively. The initial configurations of BDT molecules adsorbed on Au (001) nanowire come from GCMC final adsorption structures (Figure 5.3 and Figure 5.4). The time step in the outer-loop is $\Delta t = 2\,fs$. In implementing the double-RESPA scheme as shown above, the numbers of inner and inner-inner loops are n = 5 and m = 4, so the gain is 20 which means the timestep is 20 times smaller in the inner-inner loop. The smallest time step is 0.1 *fs* for the H-atom motion. The mass of the thermostat Q is chosen according to the equation $Q = 3NkT\tau$, where τ is some characteristic time in the system. We notice that the equilibrium process is not sensitive to the chosen Q value. Therefore, we arbitrarily choose $\tau = 500\,fs$ in this study. Figure 6.1 and 6.2 clearly show that the system approaches equilibrium in approximately 2 *ps*. The total quantity H' remains constant except for a small fluctuation in the first few time steps. Therefore, the modified double-RESPA scheme works well for our Au-BDT system.

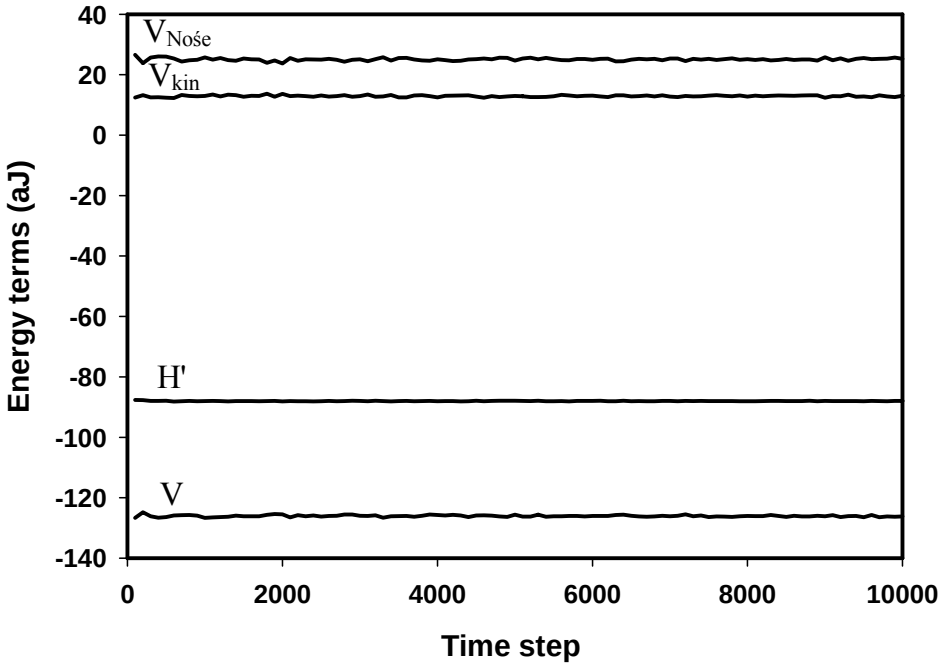

Figure 6.1. Equilibration of BDT molecules on 256-atom Au (001) nanowire during the first 20 ps MD runs.

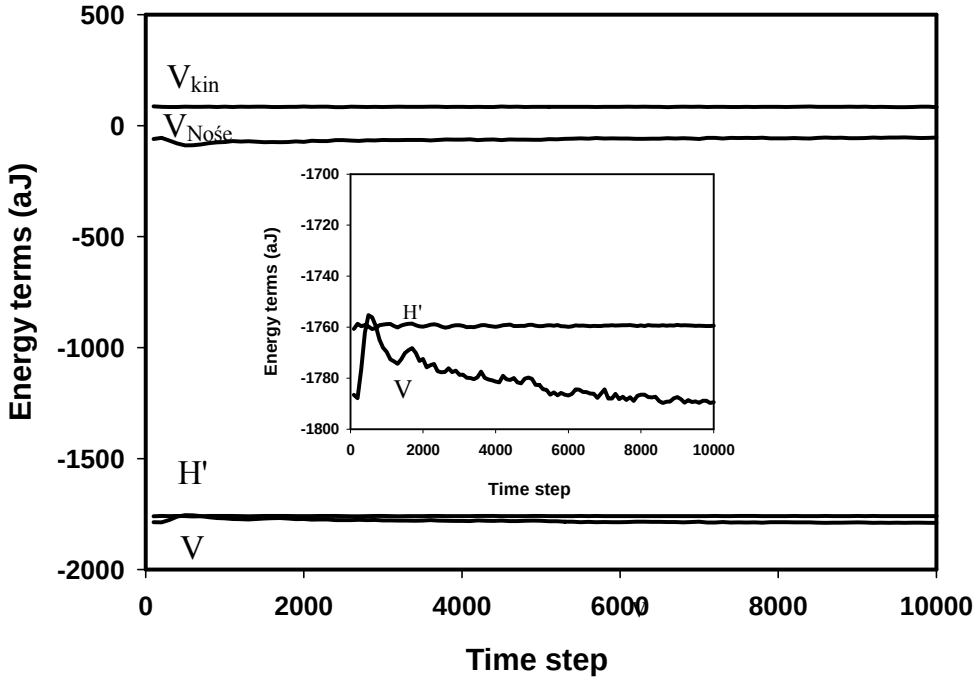

Figure 6.2. Equilibration of BDT molecules on 3254-atom Au (001) nanowire during the first 20 ps MD runs.

6.3.2. Au-BDT Bonding Geometry

The Au-BDT bonding geometry is one of the critical parameters in determining the adsorption structures, and thus ultimately has a significant effect on the electronic properties of metal-molecule-metal junctions. Here we plot the probability distributions of the angles between the C atom (the one which to the bonded S atom), the bonded S atom, and one of the two nearest Au atoms, in Figure 6.3 and Figure 6.4 respectively. The statistical averages are obtained over the second 20 ps run right after 20 ps initial equilibration. It is seen that there is only one dominant peak for each case, which is 112 degree and 117 degree, respectively. The angles reflect the orientation information of bonded BDT on Au nanowires, which has not been investigated before. Previously, the adsorption and bonding of BDT molecules has mainly focused on flat Au surfaces or clusters. Tanibayashi *et al*.[99] obtained stable structure of single BDT between two Au (111) surfaces within the framework of density-functional-theory. They found that the bridge site is the most stable binding site with the angle between the axis along S-C_6H_4-SH and the normal of the Au (111) surface about 62 degree. From surface-enhanced infrared adsorption spectroscopy, Wan *et al*.[95] observed that the phenyl ring plane of benzenethiol molecule tilted about 30^o from the Au (111) surface normal.

Understanding the bonding geometry is important since it can dramatically affect the electron transport properties. Haiss *et al*.[104] showed that the electrical conductance is sensitive with regard to the tilt angle of the organic molecules. Moreover, they demonstrated that contact geometry and thermal fluctuations can be systematically controlled, through precise control of the nanoelectrode gap spacing, allowing molecules to be tilted or stretched, and by engineering the intrinsic rigidity of the molecules.

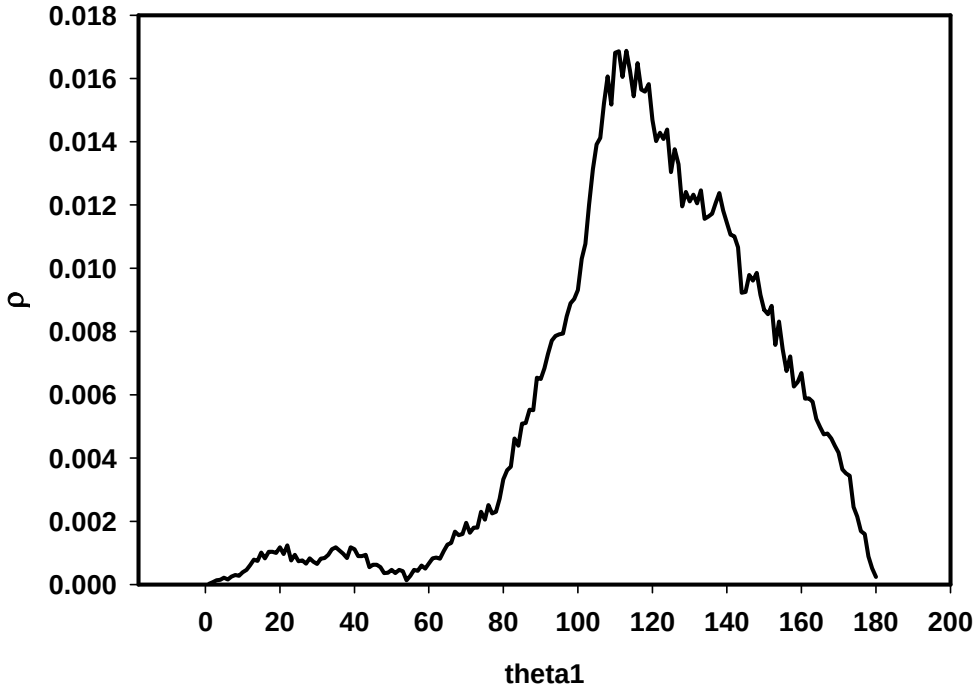

Figure 6.3. The statistical average of the probability distribution of the angle between C, bonded S, and the nearest bonded Au atom from the second 20 ps MD runs.

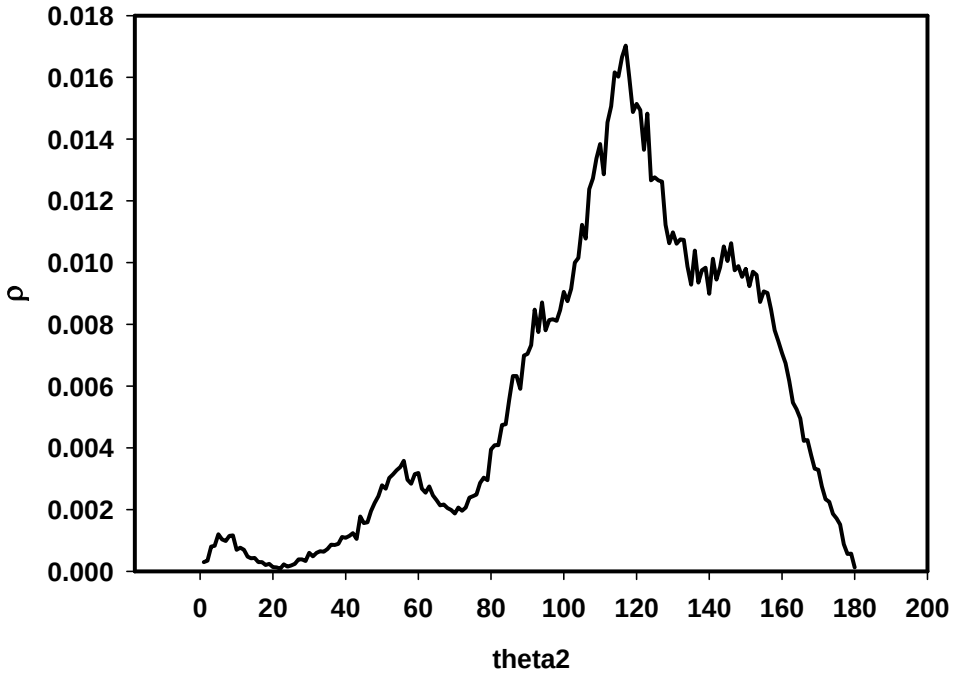

Figure 6.4. The statistical average of the probability distribution of the angle between C, bonded S, and the second nearest bonded Au atom from the second 20 ps MD runs.

6.3.3. Effect of BDT on the Ductile Elongation of Nanowires at Room Temperature

It is interesting to make a comparison between the ductile elongation properties of the 256-atom Au (001) nanowires in vacuum and in BDTs at room temperature. Starting from the final adsorption configuration from GCMC (see Figure 5.3), the gold nanowires are allowed to elongate until the occurrence of break-junctions in the presence of BDTs. Figure 6.5 shows two snapshots of the elongated nanowires in vacuum and in BDTs right before breakage at 300 K. Under this special case, the nanowire broke slowly in the presence of BDT molecules. However, keeping in mind the stochastic in nature of the break-junctions, we perform thirty independent MD runs of elongation nanowires in BDTs. The results then compare with those of nanowires elongated in vacuum. Table 6.3 summaries the calculated average ductile elongations, together with the standard deviations.

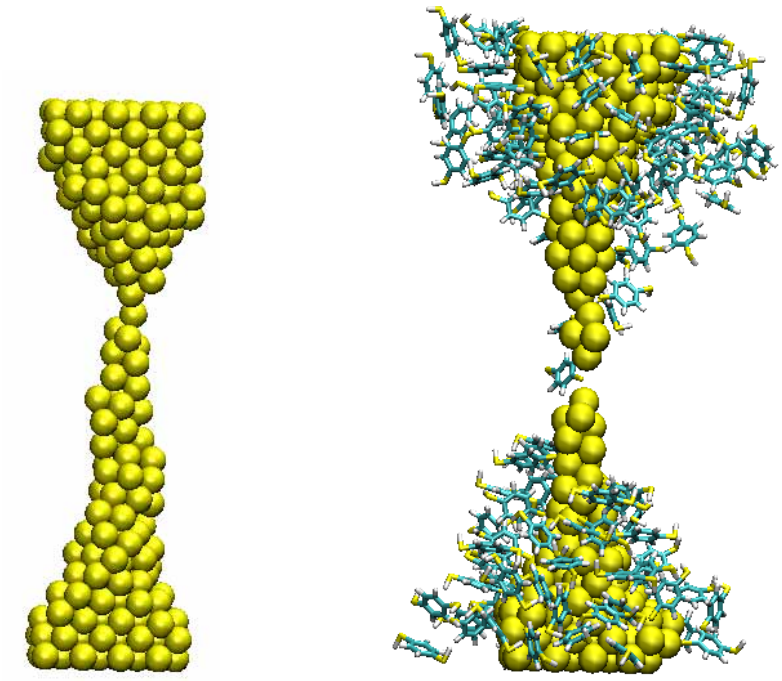

(a) (b)

Figure 6.5. Break-junction configurations of 256-Au (001) nanowire in vacuum and in solvent. (a) 256-atom gold nanowire elongated in vacuum at 300 K; (b) 256-atom gold nanowire elongated in BDT at 300 K.

Table 6.3. The variations of the ductile elongations for 256-atom Au (001) nanowires in vacuum and in BDT.

	nanowires in vacuum (Å)	nanowires in BDT (Å)
300 K	21.3 ± 6.4	26.5 ± 7.6

Firstly, for the nanowires elongated in vacuum, the elongation rate applied in this chapter is 5.0 m/s. Though the rate is at least 5 times higher than the previous studies, the relaxation process is still sufficient to simulate a quasi-static tension of gold nanowires. However, we notice that the ductile elongations are dependent on the elongation rate. To get a more complete picture of the effect of nanowire elongation on rate in vacuum, we plot the ductile elongations as a function of elongation rates as shown in Figure 6.6. It is obvious that the ductile elongations increase with increasing elongation rates except for the lower elongation rates 0.05 m/s and 0.1 m/s which have similar ductile elongations. In addition to the variation of ductile elongations with elongation rate, the standard deviations also differ. For example, the nanowires break over a wider ductile elongations range (from 13.1 Å to 40.9 Å) at the highest elongation rate 5.0 m/s. In comparison, the nanowires break in a narrower range (from 11.7 Å to 24 Å) at the lowest elongation rate 0.05 m/s.

Furthermore, the higher chances of the occurrence of longer monatomic chains in the break-junctions at higher elongation rate also account for the longer ductile elongations. Figure 6.7 shows the plot of the probabilities of occurrence of monatomic chains in the break-junctions versus the elongation rate. As the elongation rate increases, the probability of longer monatomic chains increases. For example, with elongation rate 0.05 m/s, 63% of the nanowires break up with brittle structures with no monatomic chains in the break-junctions and the longest monatomic chains is two atoms long. However, when the elongation rate increases to 5 m/s, monatomic chains occur in all thirty simulations and the longest chain length is 7.

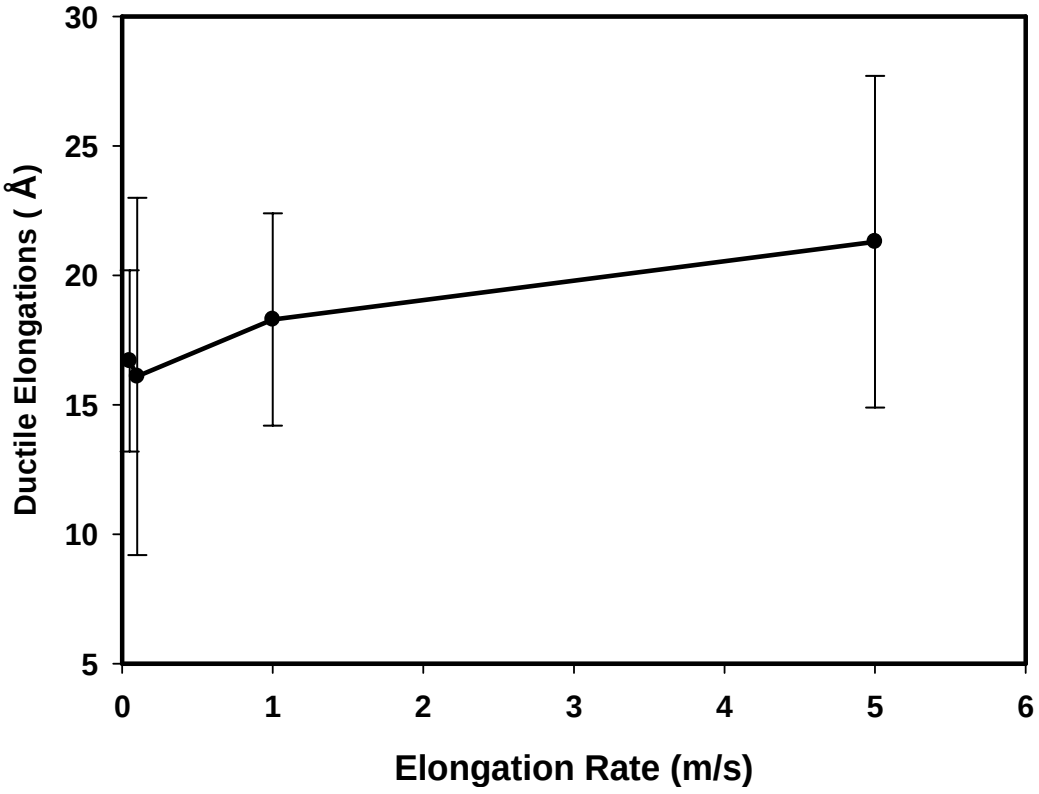

Figure 6.6. The ductile elongations as a function of elongation rate for 256-atom nanowire elongated in vacuum at room temperature.

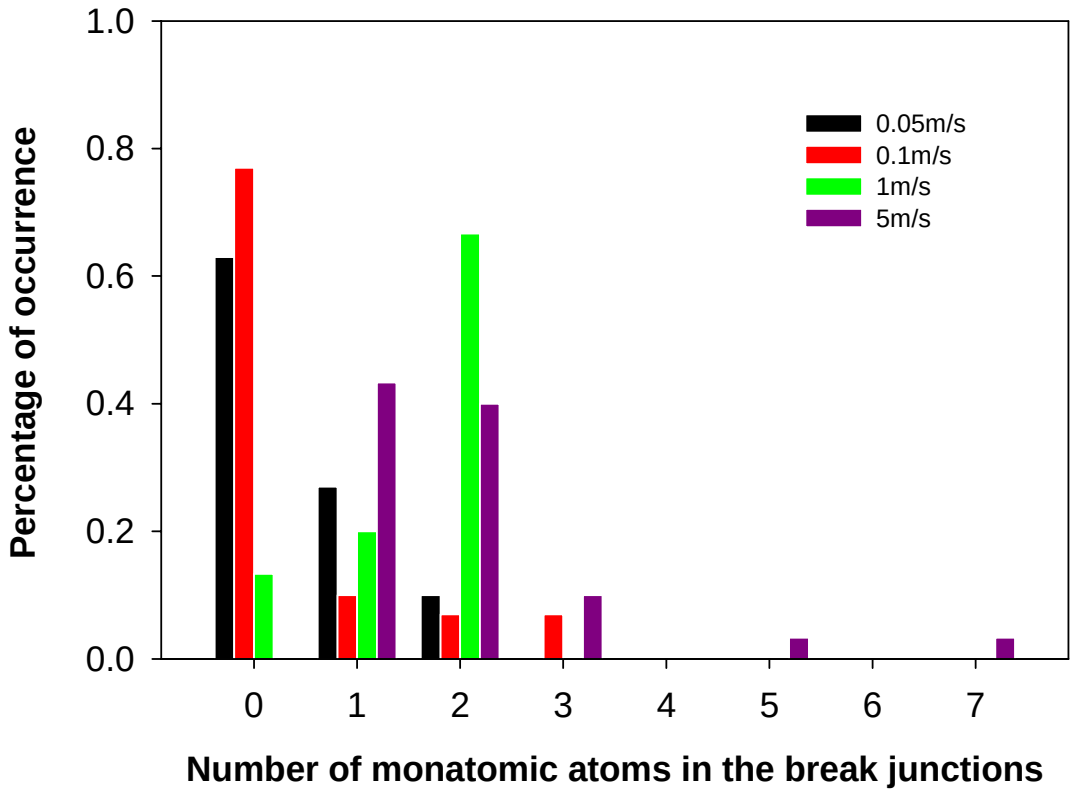

Figure 6.7. The probabilities of formation monatomic chains in the break junctions for 256-atom nanowires elongated in vacuum at room temperature at various elongation rates.

For nanowires elongated in the presence of organic molecules, it is found that the propane has no significant effect on the ductile elongation at room temperature as described in Chapter IV. However, when nanowires elongate in the presence of BDT molecules, the average ductile elongation increases 24 percent compared with that in vacuum even at room temperature. The nanowires stretched much longer before the occurrence of break-junctions because BDT molecules have the potential to chemically bond to Au atoms. The Morse potential takes effect between the bonded sulfur and Au atoms, which plays the role of reducing the tendency of Au atoms to be stretched apart.

6.3.4. Effect of BDT Density on the Ductile Elongation of Nanowires

After full absorption of BDT molecules (i.e., when the adsorbed BDT layers has come to equilibrium) on the 256-atom Au nanowire, the BDT density in the fluid surrounding the nanowire is about 1.0 g/cm^3, which is slightly lower than the BDT bulk value at 298 K (1.2 g/cm^3). However, during the process of elongating the nanowire, the box size in z direction keeps increasing. For the thirty MD runs, the nanowire can be elongated to as long as 45.4 Å until breakage. Therefore, the BDT density drops to 0.44 g/cm^3, less than half of the bulk BDT density. In order to simulate the experimental generated break-junctions to the maximum extent approaching their fabrication environment, we propose a method to combine GCMC and MD techniques to keep the BDT density at bulk density during the entire elongation process. Initially, GCMC is performed to obtain the equilibrium adsorption structure, which then input to the MD for elongating the nanowire a small distance in z direction (Δz) of 5 Å. We ignore the variation in BDT density caused by the 5.05 x 10^{-21} cm^3 increase in box size. After the 5

Å elongation has been fully relaxed in MD, the configuration is used as the starting point to run the GCMC again. BDT molecules are expected to be inserted into the simulation box to keep the BDT density approaches the bulk density.

Table 6.4 lists the calculated BDT density in the simulation box after each 5 Å elongation. It is obvious that the BDT density remains at the bulk value for the entire elongation process, thus describing Reed *et al*.'[4] experiment very realistically. It is found that the increase in the number of BDT molecules (both nonbonded and bonded) after each GCMC runs is about 25, of which only a small percent belongs to bonded BDTs as shown in Figure 6.8.

We repeat the same GCMC-MD pattern for each 5 Å elongation. Figure 6.9 shows snapshots after each GCMC runs, which represents nanowires elongated in the presence of bulk BDT molecules. In the case of pure MD elongation without any intermediate GCMC steps, the metal-molecule-metal structure is generated at ductile elongation of 21.2 Å. However, the insertion of the BDT molecules, particularly the bonded BDT molecules, increases the ductile elongation remarkably. During the elongation process, the nanowire itself forms brittle long chain structure with two to four Au atoms in the cross sections lasting over 0.3 ns. The nanowire breaks at ductile elongation of 42.5 Å which is two times longer than that pure MD elongation. The surrounding BDT molecules, especially those bonded to the bridge sites of the Au nanowires, is the key factor in reducing the probability of breakage of the Au nanowires.

Table 6.4. The BDT density after each 5 Å increase in box length in *z* direction.

increase in z length (Å)	BDT density (g/cm^3)
5	1.07
10	1.08
15	1.10
20	1.11
25	1.11
30	1.15
35	1.14
40	1.13

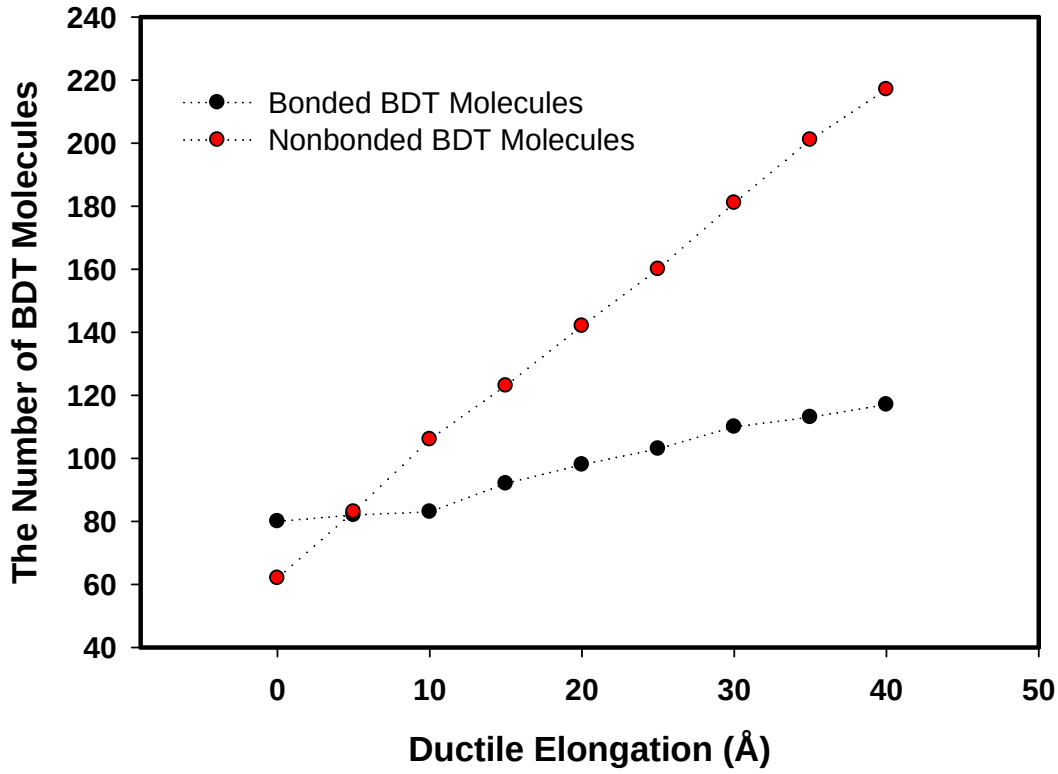

Figure 6.8. The variation in the number of nonbonded and bonded BDTs in the simulation box during the entire elongation process.

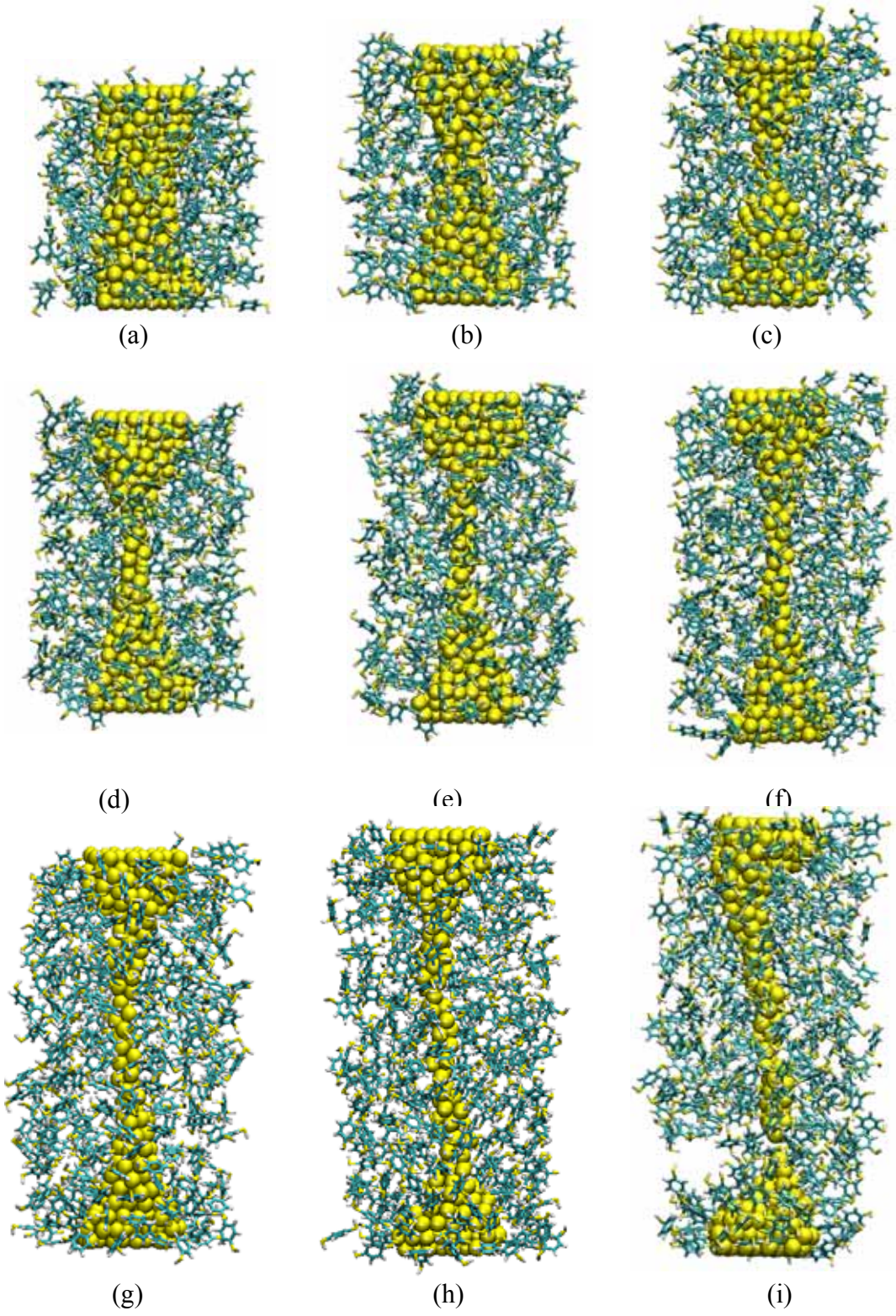

Figure 6.9. The snapshots of a 256-atom nanowire elongated in bulk BDT environment at room temperature. (a) Δz = 5Å; (b) Δz = 10Å; (c) Δz = 15Å; (d) Δz = 20Å; (e) Δz = 25Å; (f) Δz = 30Å; (g) Δz = 35Å; (h) Δz = 40Å; (i) Δz = 42.5Å.

6.4. Conclusions

Combining GCMC with MD techniques, we further explore the dynamic elongations of gold nanowires in the presence of BDT molecules. Unlike propane, BDT molecules do form chemical bonds with Au atoms. Simulation results demonstrate that the existence of BDT molecules significantly increase the ductile elongations compared with those obtained in vacuum even if the temperature is well below the melting point of gold nanowire. In addition, the ductile elongation increases notably in the presence of bulk BDT molecules which are attributed to the bonded BDT molecules.

CHAPTER VII

CONCLUSIONS AND RECOMMENDATIONS

7.1. Conclusions

We present in this research the mechanical elongation behavior of gold nanowires in vacuum and in solvents. Firstly, for the elongation of nanowires in vacuum, we identify a suitable forcefield in describing the interaction between Au atoms for the system size in our research. By comparing the static and dynamic relaxation energy between DFT total energy calculations and those of semi-empirical forcefields, it has been verified that among the three widely used semi-empirical potentials (i.e., the glue model, the EAM and the TB-SMA potentials), the TB-SMA potential is the most appropriate forcefield in describing the structural and mechanical properties of gold nanowires during elongation. Furthermore, the visualization of the snapshots along the elongation path shows that the TB-SMA images are very similar to those of the DFT local energy minima. Moreover, the TB-SMA potential has the ability to generate monatomic chains in the break-junctions and predict the 1.5 N breakup forces, as observed by many experiments.

Secondly, applying the TB-SMA potential, MD simulations have been conducted to study the impact of the crystallographic orientation, length, elongation rate, and temperature on the ductile elongations of nanowires in the vacuum environment. Due to the statistical nature of the elongation process, all of our results are based on thirty independent MD runs of the small system studied. The results show that a combination

of low temperature with high elongation rate is necessary to form monatomic chains with more than two atoms in length. In contrast, high temperature or low elongation rates diminish the probability of the formation of long monatomic chain structures. Furthermore, increasing the length of the nanowires assists the formation of longer monatomic chains in the break junctions at low temperature 0.01 K. An interesting phenomenon we observe is the formation of the helical, zigzag-type break-junction structures when high temperature (300 K) is combined with low elongation rate. Therefore, the TB-SMA has the capability to successfully produce two typical experimentally observed break-junction structures – the monatomic chain and the zigzag, helical structures.

Next, MD simulations have been performed to study the influence of the thermal collisions of nonbonded particles on the dynamic elongation properties of nanowires when they are elongated in a simple Lennard-Jones solvent - propane. Simulation results demonstrate that the solvent effect is minimal if the temperature is below the melting point of gold nanowire. However, as long as the temperature approaches the melting point, the average ductile elongation of Au nanowire in propane solvent is lower than that of Au nanowire in vacuum.

The next step is to investigate the self-assembly of BDT molecules on Au nanowires by GCMC simulation. The local bonding geometry of BDT-Au obtained in this work is consistent with previous results that S binds most favorably on the bridge sites of the Au surface. In addition, we find that the packing density of bonded BDT on the surface of Au nanowire is larger than that of BT molecules on Au (111) surface, evidently due to the curved surface of gold wire.

For the last step, MD simulations and canonical Monte Carlo simulations are performed to study, for the first time, the elongation dynamics and structure of metal-molecule-metal in the presences BDT molecules which have the potential to form chemical bonds with Au atoms. Simulation results demonstrate that the presences of BDT molecules has significant effect on ductile elongation compared with those obtained in vacuum even at room temperature. In addition, the ductile elongation increases considerably in the presence of bulk BDT molecules, mainly due to the bonded BDTs constrain the elongation of Au atoms.

7.2. Recommendations

In this study, we have developed a technique to combine MD with GCMC simulations to study the dynamic elongations of nanowires in a covalently bonding BDT solution. In the future work, we could apply molecular dynamics simulation in grand canonical ensemble (GCMD)[105] technique as proposed by Eslami *et al*. to our Au-BDT system. The GCMD method outlined in their work is capable of performing simulations in the grand canonical ensemble over the whole density range which is especially appropriate to our dense BDT adsorption structures. By performing GCMD technique, the data transfer between MD and GCMC simulations is eliminated. However, a parallel GCMD code would be necessary due to the large number of molecules involved.

After the GCMD code works efficiently, we could further explore the effects of crystallographic orientation, length, elongation rate, as well as temperature on the ductile elongations of nanowires in a statistical approach as we have done for nanowires elongated in the vacuum environment.

REFERENCES

(1) Gall, K.; Diao, J. K.; Dunn, M. L.; Haftel, M.; Bernstein, N.; Mehl, M. J. *Journal of Engineering Materials and Technology-Transactions of the Asme* **2005**, *127*, 417.

(2) da Silva, E. Z.; da Silva, A. J. R.; Fazzio, A. *Physical Review Letters* **2001**, *87*, 256102.

(3) Cui, X. D.; Primak, A.; Zarate, X.; Tomfohr, J.; Sankey, O. F.; Moore, A. L.; Moore, T. A.; Gust, D.; Harris, G.; Lindsay, S. M. *Science* **2001**, *294*, 571.

(4) Reed, M. A.; Zhou, C.; Muller, C. J.; Burgin, T. P.; Tour, J. M. *Science* **1997**, *278*, 252.

(5) Xu, B. Q.; Tao, N. J. J. *Science* **2003**, *301*, 1221.

(6) Krans, J. M.; Vanruitenbeek, J. M.; Fisun, V. V.; Yanson, I. K.; Dejongh, L. J. *Nature* **1995**, *375*, 767.

(7) Muller, C. J.; Vanruitenbeek, J. M.; Dejongh, L. J. *Physical Review Letters* **1992**, *69*, 140.

(8) Untiedt, C.; Yanson, A. I.; Grande, R.; Rubio-Bollinger, G.; Agrait, N.; Vieira, S.; van Ruitenbeek, J. M. *Physical Review B* **2002**, *66*, 085418.

(9) Mehrez, H.; Ciraci, S. *Physical Review B* **1997**, *56*, 12632.

(10) Rubio-Bollinger, G.; Bahn, S. R.; Agrait, N.; Jacobsen, K. W.; Vieira, S. *Physical Review Letters* **2001**, *87*, 026101.

(11) Sorensen, M. R.; Brandbyge, M.; Jacobsen, K. W. *Physical Review B* **1998**, *57*, 3283.

(12) Todorov, T. N.; Sutton, A. P. *Physical Review B* **1996**, *54*, 14234.

(13) Finbow, G. M.; LyndenBell, R. M.; McDonald, I. R. *Molecular Physics* **1997**, *92*, 705.

(14) Landman, U.; Luedtke, W. D.; Salisbury, B. E.; Whetten, R. L. *Physical Review Letters* **1996**, *77*, 1362.

(15) Tanimori, S.; Shimamura, S. *Journal of the Physical Society of Japan* **1999**, *68*, 3556.

(16) Coura, P. Z.; Legoas, S. B.; Moreira, A. S.; Sato, F.; Rodrigues, V.; Dantas, S. O.; Ugarte, D.; Galvao, D. S. *Nano Letters* **2004**, *4*, 1187.

(17) Torres, J. A.; Tosatti, E.; Dal Corso, A.; Ercolessi, F.; Kohanoff, J. J.; Di Tolla, F. D.; Soler, J. M. *Surface Science* **1999**, *426*, L441.

(18) Tosatti, E.; Prestipino, S.; Kostlmeier, S.; Dal Corso, A.; Di Tolla, F. D. *Science* **2001**, *291*, 288.

(19) Bilalbegovic, G. *Journal of Physics:Condensed Matter* **2001**, *13*, 11531.

(20) Todorov, T. N.; Sutton, A. P. *Physical Review Letters* **1993**, *70*, 2138.

(21) Di Ventra, M.; Pantelides, S. T.; Lang, N. D. *Physical Review Letters* **2000**, *84*, 979.

(22) Kornilovitch, P. E.; Bratkovsky, A. M. *Physical Review B* **2001**, *64*, 195413.

(23) Krstic, P. S.; Dean, D. J.; Zhang, X. G.; Keffer, D.; Leng, Y. S.; Cummings, P. T.; Wells, J. C. *Computational Materials Science* **2003**, *28*, 321.

(24) Seminario, J. M.; Zacarias, A. G.; Tour, J. M. *Journal of Physical Chemistry A* **1999**, *103*, 7883.

(25) Stokbro, K.; Taylor, J.; Brandbyge, M.; Mozos, J. L.; Ordejon, P. *Computational Materials Science* **2003**, *27*, 151.

(26) Joachim, C.; Gimzewski, J. K.; Aviram, A. *Nature* **2000**, *408*, 541.

(27) Chen, J.; Reed, M. A.; Rawlett, A. M.; Tour, J. M. *Science* **1999**, *286*, 1550.

(28) Di Ventra, M.; Kim, S. G.; Pantelides, S. T.; Lang, N. D. *Physical Review Letters* **2001**, *86*, 288.

(29) Hipps, K. W. *Science* **2001**, *294*, 536.

(30) Yaliraki, S. N.; Kemp, M.; Ratner, M. A. *Journal of the American Chemical Society* **1999**, *121*, 3428.

(31) Aviram, A.; Ratner, M. A. *Chemical Physics Letters* **1974**, *29*, 277.

(32) Andres, R. P.; Bein, T.; Dorogi, M.; Feng, S.; Henderson, J. I.; Kubiak, C. P.; Mahoney, W.; Osifchin, R. G.; Reifenberger, R. *Science* **1996**, *272*, 1323.

(33) Collier, C. P.; Wong, E. W.; Belohradsky, M.; Raymo, F. M.; Stoddart, J. F.; Kuekes, P. J.; Williams, R. S.; Heath, J. R. *Science* **1999**, *285*, 391.

(34) Feldheim, D. L.; Keating, C. D. *Chemical Society Reviews* **1998**, *27*, 1.

(35) Klein, D. L.; Roth, R.; Lim, A. K. L.; Alivisatos, A. P.; McEuen, P. L. *Nature* **1997**, *389*, 699.

(36) Blum, A. S.; Kushmerick, J. G.; Long, D. P.; Patterson, C. H.; Yang, J. C.; Henderson, J. C.; Yao, Y. X.; Tour, J. M.; Shashidhar, R.; Ratna, B. R. *Nature Materials* **2005**, *4*, 167.

(37) Bigioni, T. P.; Harrell, L. E.; Cullen, W. G.; Guthrie, D. E.; Whetten, R. L.; First, P. N. *European Physical Journal D* **1999**, *6*, 355.

(38) Harrell, L. E.; Bigioni, T. P.; Cullen, W. G.; Whetten, R. L.; First, P. N. *Journal of Vacuum Science & Technology B* **1999**, *17*, 2411.

(39) Osman, H.; Schmidt, J.; Svensson, K.; Palmer, R. E.; Shigeta, Y.; Wilcoxon, J. P. *Chemical Physics Letters* **2000**, *330*, 1.

(40) Peterson, R. R.; Cliffel, D. E. *Analytical Chemistry* **2005**, *77*, 4348.

(41) Collier, C. P.; Mattersteig, G.; Wong, E. W.; Luo, Y.; Beverly, K.; Sampaio, J.; Raymo, F. M.; Stoddart, J. F.; Heath, J. R. *Science* **2000**, *289*, 1172.

(42) Heath, J. R.; Kuekes, P. J.; Snider, G. S.; Williams, R. S. *Science* **1998**, *280*, 1716.

(43) Luo, Y.; Collier, C. P.; Jeppesen, J. O.; Nielsen, K. A.; Delonno, E.; Ho, G.; Perkins, J.; Tseng, H. R.; Yamamoto, T.; Stoddart, J. F.; Heath, J. R. *Chemphyschem* **2002**, *3*, 519.

(44) Leng, Y. S.; Keffer, D. J.; Cummings, P. T. *Journal of Physical Chemistry B* **2003**, *107*, 11940.

(45) Leng, Y. S.; Krstic, P. S.; Wells, J. C.; Cummings, P. T.; Dean, D. J. *Journal of Chemical Physics* **2005**, *122*, 244721.

(46) Zhao, X. C.; Leng, Y. S.; Cummings, P. T. *Langmuir* **2006**, *22*, 4116.

(47) Pascual, J. I.; Mendez, J.; Gomezherrero, J.; Baro, A. M.; Garcia, N.; Binh, V. T. *Physical Review Letters* **1993**, *71*, 1852.

(48) Yanson, A. I.; Bollinger, G. R.; van den Brom, H. E.; Agrait, N.; van Ruitenbeek, J. M. *Nature* **1998**, *395*, 783.

(49) Ohnishi, H.; Kondo, Y.; Takayanagi, K. *Nature* **1998**, *395*, 780.

(50) Rubio, G.; Agrait, N.; Vieira, S. *Physical Review Letters* **1996**, *76*, 2302.

(51) Marszalek, P. E.; Greenleaf, W. J.; Li, H. B.; Oberhauser, A. F.; Fernandez, J. M. *Proceedings of the National Academy of Sciences of the United States of America* **2000**, *97*, 6282.

(52) Rodrigues, V.; Fuhrer, T.; Ugarte, D. *Physical Review Letters* **2000**, *85*, 4124.

(53) Rodrigues, V.; Ugarte, D. *Physical Review B* **2001**, *63*, 073405.

(54) Barnett, R. N.; Landman, U. *Nature* **1997**, *387*, 788.

(55) Ercolessi, F.; Parrinello, M.; Tosatti, E. *Philosophical Magazine a-Physics of Condensed Matter Structure Defects and Mechanical Properties* **1988**, *58*, 213.

(56) Hakkinen, H.; Barnett, R. N.; Scherbakov, A. G.; Landman, U. *Journal of Physical Chemistry B* **2000**, *104*, 9063.

(57) Kruger, D.; Fuchs, H.; Rousseau, R.; Marx, D.; Parrinello, M. *Physical Review Letters* **2002**, *89*, 186402.

(58) Voter, A. F. *Los Alamos Unclassified Technical Report # LA-UR 93-3901* **1993**.

(59) Cleri, F.; Rosato, V. *Physical Review B* **1993**, *48*, 22.

(60) Kondo, Y.; Takayanagi, K. *Science* **2000**, *289*, 606.

(61) Park, H. S.; Zimmerman, J. A. *Physical Review B* **2005**, *72*, 054106.

(62) Park, H. S.; Zimmerman, J. A. *Scripta Materialia* **2006**, *54*, 1127.

(63) Sanchez-Portal, D.; Artacho, E.; Junquera, J.; Ordejon, P.; Garcia, A.; Soler, J. M. *Physical Review Letters* **1999**, *83*, 3884.

(64) Chen, A. F. V. a. S. P. *Mat. Res. Soc. Symp. Proc.* **1987**, *82*, 175.

(65) Lothe, J. P. H. a. J. *Theory of Dislocations, Krieger Publishing Company* **1982**.

(66) Martyna, G. J.; Tuckerman, M. E.; Tobias, D. J.; Klein, M. L. *Molecular Physics* **1996**, *87*, 1117.

(67) Nose, S. *Journal of Chemical Physics* **1984**, *81*, 511.

(68) Tuckerman, M.; Berne, B. J.; Martyna, G. J. *Journal of Chemical Physics* **1992**, *97*, 1990.

(69) Perdew, J. P.; Zunger, A. *Physical Review B* **1981**, *23*, 5048.

(70) Vanderbilt, D. *Physical Review B* **1990**, *41*, 7892.

(71) Kresse, G.; Furthmuller, J. *Physical Review B* **1996**, *54*, 11169.

(72) Galanakis, I.; Papanikolaou, N.; Dederichs, P. H. *Surface Science* **2002**, *511*, 1.

(73) Yu, B. D.; Scheffler, M. *Physical Review B* **1997**, *56*, R15569.

(74) Hakkinen, H.; Moseler, M.; Landman, U. *Physical Review Letters* **2002**, *89*, 033401.

(75) Xiao, L.; Tollberg, B.; Hu, X. K.; Wang, L. C. *Journal of Chemical Physics* **2006**, *124*, 114309.

(76) Csonka, S.; Halbritter, A.; Mihaly, G.; Jurdik, E.; Shklyarevskii, O. I.; Speller, S.; van Kempen, H. *Physical Review Letters* **2003**, *90*, 116803.

(77) Li, C. Z.; He, H. X.; Bogozi, A.; Bunch, J. S.; Tao, N. J. *Applied Physics Letters* **2000**, *76*, 1333.

(78) Novaes, F. D.; da Silva, A. J. R.; da Silva, E. Z.; Fazzio, A. *Physical Review Letters* **2003**, *90*, 036101.

(79) Novaes, F. D.; Da Silva, A. J. R.; Fazzio, A.; Da Silva, E. Z. *Applied Physics a-Materials Science & Processing* **2005**, *81*, 1551.

(80) Rappe, A. K.; Casewit, C. J.; Colwell, K. S.; Goddard, W. A.; Skiff, W. M. *Journal of the American Chemical Society* **1992**, *114*, 10024.

(81) Prausnitz, J. M. *Molecular Thermodynamics of Fluid-Phase Equilibria*, 109.

(82) Pu, Q.; Leng, Y. S.; Tsetseris, L.; Park, H. S.; Pantelides, S. T.; Cummings, P. T. *Journal of Chemical Physics* **2007**, *126*, Art. No. 144707.

(83) Toxvaerd, S. *Journal of Chemical Physics* **1989**, *91*, 3716.

(84) Bilalbegovic, G. *Solid State Communications* **2000**, *115*, 73.

(85) Cleveland, C. L.; Luedtke, W. D.; Landman, U. *Physical Review B* **1999**, *60*, 5065.

(86) Gulseren, O.; Ercolessi, F.; Tosatti, E. *Physical Review B* **1995**, *51*, 7377.

(87) Tsutsui, M.; Teramae, Y.; Kurokawa, S.; Sakai, A. *Applied Physics Letters* **2006**, *89*, 163111.

(88) Xiao, X. Y.; Xu, B. Q.; Tao, N. J. *Nano Letters* **2004**, *4*, 267.

(89) Mahaffy, R.; Bhatia, R.; Garrison, B. J. *Journal of Physical Chemistry B* **1997**, *101*, 771.

(90) Sadreev, A. F.; Sukhinin, Y. V. *Journal of Chemical Physics* **1997**, *107*, 2643.

(91) Leng, Y. S.; Dyer, P. J.; Krstic, P. S.; Harrison, R. J.; Cummings, P. T. *Molecular Physics* **2007**, *105*, 293.

(92) Fischer, D.; Curioni, A.; Andreoni, W. *Langmuir* **2003**, *19*, 3567.

(93) Nara, J.; Geng, W. T.; Kino, H.; Kobayashi, N.; Ohno, T. *Journal of Chemical Physics* **2004**, *121*, 6485.

(94) Smit, B. *Molecular Physics* **1995**, *85*, 153.

(95) Wan, L. J.; Terashima, M.; Noda, H.; Osawa, M. *Journal of Physical Chemistry B* **2000**, *104*, 3563.

(96) Mar, W.; Klein, M. L. *Langmuir* **1994**, *10*, 188.

(97) Nuzzo, R. G.; Allara, D. L. *Journal of the American Chemical Society* **1983**, *105*, 4481.

(98) Ulman, A. *An Introduction to Ultra-thin Organic Films: From Langmuir-Blodgett to Self-Assembly* **1991**, *Academic Press*, San Diego.

(99) Tanibayashi, S.; Tada, T.; Watanabe, S.; Yoshizawa, K. *Japanese Journal of Applied Physics Part 1-Regular Papers Brief Communications & Review Papers* **2005**, *44*, 7729.

(100) Pontes, R. B.; Novaes, F. D.; Fazzio, A.; da Silva, A. J. R. *Journal of the American Chemical Society* **2006**, *128*, 8996.

(101) Tsutsui, M.; Teramae, Y.; Kurokawa, S.; Sakai, A. *Applied Physics Letters* **2006**, *89*.

(102) Li, X. L.; He, J.; Hihath, J.; Xu, B. Q.; Lindsay, S. M.; Tao, N. J. *Journal of the American Chemical Society* **2006**, *128*, 2135.

(103) Hoover, W. G. *Physical Review A* **1985**, *31*, 1695.

(104) Haiss, W.; Wang, C. S.; Grace, I.; Batsanov, A. S.; Schiffrin, D. J.; Higgins, S. J.; Bryce, M. R.; Lambert, C. J.; Nichols, R. J. *Nature Materials* **2006**, *5*, 995.

(105) Eslami, H.; Muller-Plathe, F. *Journal of Computational Chemistry* **2007**, *28*, 1763.